

Review of Aeronautical Fatigue Investigations in Brazil

**International Committee on Aeronautical Fatigue and
Structural Integrity - ICAF 2023**

Prepared by:

Carlos E. Chaves

On behalf of:

Fatigue, Fracture and Structural Integrity Committee

Brazilian Society of Engineering and Mechanical Sciences – ABCM

2/6/2023

SUMMARY

This report presents the review of fatigue and fracture investigations related to aeronautical structures performed in Brazil from the middle of 2021 to the middle of 2023. Its contents will be made available for public domain during the 38th ICAF (International Committee on Aeronautical Fatigue and Structural Integrity) Conference to be held in Delft, the Netherlands, in June 26-29, 2023.

All papers, dissertations, theses, and conference proceedings presented in this document were directly supplied by their authors, co-authors, or advisors to the author of this review, and a number of these works were previously presented in conferences or are available from public sources.

CONTENTS

| | |
|---|----|
| SUMMARY..... | 1 |
| CONTENTS..... | 2 |
| ABBREVIATIONS..... | 3 |
| SYMBOLS..... | 5 |
| LIST OF FIGURES..... | 6 |
| 1. INTRODUCTION..... | 12 |
| 2. CRACK GROWTH ANALYSIS AND SIMULATION..... | 14 |
| 3. METALLIC MATERIALS AND STRUCTURES..... | 19 |
| Fatigue and Fracture Properties..... | 19 |
| Fretting Fatigue..... | 23 |
| Mechanical Processes and Surface Treatments..... | 34 |
| Metallic Structures..... | 37 |
| Structural Health Monitoring..... | 50 |
| 4. COMPOSITE MATERIALS AND STRUCTURES..... | 55 |
| Composite Materials..... | 55 |
| Structural Health Monitoring..... | 68 |
| 5. PROBABILISTIC MODELLING AND RISK ANALYSIS..... | 74 |
| 6. FATIGUE LOADS..... | 77 |
| 7. AIRWORTHINESS..... | 84 |
| 8. REFERENCES..... | 88 |

ABBREVIATIONS

| | |
|-------|--|
| 3-ENF | Three Point Bend End-notched Flexure |
| ANN | Artificial Neural Network |
| AM | Additive Manufacturing |
| ASTM | American Society for Testing and Materials |
| CBBM | Compliance Based Beam Method |
| CDF | Cumulative Distribution Function |
| CDM | Continuum Damage Mechanics |
| CFC | Carbon Fiber Composite |
| CT | Compact Tension (Specimen) |
| CZM | Cohesive Zone Modelling |
| DCM | Displacement Correlation Method |
| DI | Damage Index |
| FC | Flight Cycles |
| FF | Fretting Fatigue |
| CBBM | Compliance Based Beam Model |
| CDM | Continuum Damage Mechanics |
| GFC | Glass Fiber Composite |
| GFEM | Generalized Finite Element Method |
| CLC | Combined Loading Compression |
| CUF | Carrera's Unified Formulation |
| DCB | Double Cantilever Beam |
| DCM | Displacement Correlation Method |
| HC | Hybrid Composite |
| HS | Hardness Satin |
| IRS | Independent Random Sampling |
| ISO | International Organization for Standardization |
| kN | kilo-Newton |
| KQvM | Stress Intensity Factor Obtained with Chevron Test (ASTM E1304-97) |
| LEFM | Linear Elastic Fracture Mechanics |
| LPBF | Laser Powder Bed Fusion |
| MLG | Main Landing Gear |

| | |
|-------|--|
| MWCM | Modified Wöhler Curve Method |
| PEI | Poly(etherimide) |
| SEM | Scanning Electron Microscopy |
| SERR | Strain Energy Release Rate |
| SGFEM | Stable Generalized Finite Element Method |
| SHM | Structural Health Monitoring |
| SIF | Stress Intensity Factor |
| SFPOF | Single Flight Probability of Failure |
| SWT | Smith, Watson and Topper |
| TCD | Theory of Critical Distances |
| UEL | User Element subroutine |
| VBM | Vibration Based Method |
| VCCT | Virtual Crack Closure Technique |

SYMBOLS

| | |
|-----------------|-------------------------------------|
| δ | Displacement |
| δ_{\min} | Minimum displacement |
| δ_{\max} | Maximum displacement |
| ΔG | Strain energy variation |
| G_{Ic} | Critical strain energy release rate |
| N_f | Number of cycles to failure |
| τ_a | Shear stress amplitude |

LIST OF FIGURES

| | |
|--|----|
| Figure 1 - Plate with a central crack subjected to mode I crack growth. | 15 |
| Figure 2 - Predicted smeared damage contours for a pure mode I simulation for: (a) low-stress loading condition, (b) high-stress loading condition..... | 15 |
| Figure 3 - Crack growth curves for mode I loading under the high-stress loading condition: (a) $a \times N$, (b) $da/dN \times \Delta K$ | 16 |
| Figure 4 - Centered inclined cracked panel. Green nodes enriched with Branch Functions and red nodes enriched with Linear Heaviside Functions. | 17 |
| Figure 5 - SIF comparison between GFEM and SGFEM - Mode II - Inclined centered crack..... | 18 |
| Figure 6 - Test machine with specimen and instrumentation installed..... | 21 |
| Figure 7 - Test matrix - number of specimens and overloads applied..... | 21 |
| Figure 8 - Crack growth curves for specimens corresponding to Configuration 01 (single overload $P = 13$ kN, vertical axis in left plot corresponds to measured crack length)..... | 22 |
| Figure 9 - Test results and model fit for Configuration 04 (vertical axis corresponds to measured crack length)..... | 22 |
| Figure 10 - New Fretting Fatigue Machine of the University of Brasilia (UnB)..... | 26 |
| Figure 11 - Schematic view and component list of the new Fretting Fatigue Machine of the University of Brasilia (UnB)..... | 27 |
| Figure 12 - Photo and dimensions of the fretting specimens..... | 27 |
| Figure 13 - Flowchart illustrating all the process to construct the ANN models..... | 29 |
| Figure 14 - (a) SWT parameter versus fatigue life for the 2024-T3. (b) Modified Wöhler curve for the 2024-T3..... | 30 |
| Figure 15 - Estimated fatigue life by the ANN_SHEAR model vs. the experimental one (a). Estimated fatigue life by the ANN_NORMAL model vs. the experimental...30 | 30 |

| | |
|---|----|
| Figure 16 - Estimated fatigue life considering all the models vs. experimental data for 2024-T3 alloy. | 31 |
| Figure 17 - Schematic representation of the application of loads in the fretting fatigue test: (a) representation of where each load is applied to the specimen,(b) order of application of test loads, and the representation of the H-L (c) and L-H (d) loading blocks..... | 32 |
| Figure 18 - FE model for the fretting fatigue problem. | 33 |
| Figure 19 - Geometry and dimensions (mm) of the FCG specimens, including laser lines positioning. | 35 |
| Figure 20 - FCG test results: (a) crack length vs. number of cycles for $R = 0.1$, (b) crack growth rate da/dN vs. ΔK plots for $R = 0.1$ | 35 |
| Figure 21 - Geometric properties and assumed crack location for the problem under analysis. | 38 |
| Figure 22 – Critical displacement – linear buckling comparison..... | 39 |
| Figure 23 - Force x displacement - $a = 60$ mm - Configuration 1 | 40 |
| Figure 24 - Comparisons for the post-buckling geometric correction factors: (a) crack growth cycles, (b) crack growth rate. | 40 |
| Figure 25 - Bending stress (obtained from FEM analysis) for a flat panel (unconstrained and constrained) and for a curved panel. | 42 |
| Figure 26 - Curved Sub-scale Panel Test Setup..... | 42 |
| Figure 27 - 4 Plate and stringer geometry – with A1 and A2 as the two crack front directions. | 44 |
| Figure 28 - Experimental test setup for fatigue tests (left) and residual strength tests (right)..... | 45 |
| Figure 29 - Crack propagation result for each stiffened panel and crack front..... | 45 |
| Figure 30 - Residual strength test results. | 46 |
| Figure 31 - FEM model - schematic..... | 46 |
| Figure 32 - Numerical delamination shapes tested and compared against the experimental delamination shape, measured using NDT testing. | 47 |

| | |
|--|----|
| Figure 33 - a-N curves obtained by delamination shape..... | 48 |
| Figure 34 - Model used in the simulation (left) and detail of the stiffener (right)... | 48 |
| Figure 35 - Embraer 190 E2 (second generation) wing full-scale fatigue test overview..... | 49 |
| Figure 36 - Methodology used in this work..... | 51 |
| Figure 37 - Specimen geometry used in the random vibration tests. | 51 |
| Figure 38 - Damage index "DI 1" versus time..... | 52 |
| Figure 39 - Crack size versus time: experimental and numerical values..... | 52 |
| Figure 40 - Strip with edge cracks subjected to bending moment. | 53 |
| Figure 41 - Geometry and detail of the mesh around the crack used in the numerical analysis..... | 54 |
| Figure 42 - Uncertainty in damage index values for a crack size close to 8 mm..... | 54 |
| Figure 43 - (a) Schematic perspective drawing of the new jig and (b) a detail of a coupon assembled on the jig. | 56 |
| Figure 44 - (a) Coupons after the fatigue tests and (b) detail of the failure mode obtained in a sample coupon..... | 56 |
| Figure 45 - Specimens fractured in the cycling test (a) with 85% of the tensile strength, (b) with 60% of the tensile strength and with the pronounced presence of delamination..... | 57 |
| Figure 46 - S-N curve for carbon/PEI composite. | 58 |
| Figure 47 - Paris model results - Mode I (CVF = glass fiber composite, or GFC)..... | 61 |
| Figure 48 - Paris model results - Mode II (CVF = glass fiber composite, or GFC). | 61 |
| Figure 49 - Experimental test set-up: (a) Load frame and stiffened panel (1- clamped ends, 2- LVDT, 3- Anti-buckling edge supports, 4- Strain gauges, (b) servo-hydraulic load frame for quasi-static compression test. | 63 |
| Figure 50 - Normalized results obtained from residual strength tests for a typical composite T-stiffened panel integrated by secondary bonding technology..... | 63 |
| Figure 51 - Finite element meshes for compact tension coupon test specimen. | 64 |

| | |
|---|----|
| Figure 52 - Coupon level results for different progressive damage formulations and aspect ratios. (left: strain based variable formulation, right: proposed damage variable formulation)..... | 65 |
| Figure 53 - Full-fatigue curve for various load ranges values..... | 66 |
| Figure 54 - Detail on the real model of the AS HB-350 blade and numerical model. | 69 |
| Figure 55 - Positioning sensors after optimization. | 70 |
| Figure 56 - Numerical model (a) isometric view, (b) parametrized damage..... | 72 |
| Figure 57 - Experimental setup for the modal testing. | 72 |
| Figure 58 - Damage identification and sizing results for the damage type in core (actual and predicted)..... | 73 |
| Figure 59 - Cracks on the web of the rear spar of a wing structure. Adapted from Ref. [35]. | 75 |
| Figure 60 - On the left: length of secondary relative to length of lead crack when it is detectable. On the right: types of secondary cracks (Ref. [36]). | 76 |
| Figure 61 - Length of the secondary cracks ($c_{[2]}$ and $c_{[3]}$) relative to the length of the lead crack ($c_{[1]}$). | 76 |
| Figure 62 - Reconstruction of the chart presented in Figure 58 (Ref. [36]). Crack lengths converted to millimeters and curves plotted in linear scale..... | 76 |
| Figure 63 - Single flight profiles solution. | 78 |
| Figure 64 - Equivalent flight profile solution..... | 78 |
| Figure 65 - Flight profiles A to D..... | 79 |
| Figure 66 - Number of lives for the flight profiles and composition..... | 80 |
| Figure 67 - Airborne spectrum discretization..... | 81 |
| Figure 68 - Load sequence for TWIST Flight Type A. | 82 |
| Figure 69 - Simple plasticity correction..... | 82 |
| Figure 70 - TWIST damage per flight type for $K_t=3$ | 83 |

Figure 71 - MLG trunnion collar location, from Tuegel et al. (Ref. [43]).....86

Figure 72 - CDF of SPOF= 10^{-4} point in FC; K_t Pinching Results.....87

LIST OF TABLES

| | |
|--|----|
| Table 1 - Forces, displacements, and temperature ranges of the new four actuators high temperature fretting fatigue rig..... | 25 |
| Table 2 - Stiffener types and dimensions. | 38 |
| Table 3 - Plate geometry. | 39 |
| Table 4 - Stiffened panel materials. | 44 |
| Table 5 - Glare® skin layup. | 44 |

1. INTRODUCTION

The present document is a summary of fatigue investigations related to aerospace materials and structures performed by Brazilian organizations (or by Brazilian researchers) over the past two years. The complete document will be made available by occasion of the 38th ICAF (International Committee on Aeronautical Fatigue and Structural Integrity) Conference to be held in Delft, The Netherlands, between June 26th and June 29th, 2023.

Some of the research works presented along this review are follow on research activities related to the ones previously presented in previous National Reviews. While some of the contributing institutions are supplying follow-on research works and new research works during this two-year period, other institutions have faced certain difficulties because there was still a negative effect of the Covid-19 pandemic during the first part of this period.

The following are the main Brazilian institutions that have collaborated during this period with research works on fatigue and fracture mechanics related to aeronautical products, and had scientific or technological research works added to this review:

- Brazilian Society of Engineering and Mechanical Sciences (ABCM) – Rio de Janeiro – RJ
- CEFET (Federal Technology Education Center) – Angra dos Reis - RJ
- University of São Paulo (USP) – São Carlos – SP
- University of São Paulo (USP) – Lorena - SP
- State University of São Paulo (UNESP) – Guaratinguetá – SP
- Federal University of Brasília (UnB) – Brasília - DF
- Federal University of Itajubá (UNIFEI) – Itajubá – MG
- Federal University of São Paulo (UNIFESP) – São José dos Campos – SP
- Aeronautics Institute of Technology (ITA) – São José dos Campos – SP
- Aeronautics and Space Institute (IAE) – São José dos Campos – SP
- Embraer S/A – São José dos Campos – SP

Further, some works to be presented were developed in cooperation with foreign institutions, from which some are mentioned here:

- University of Porto - Portugal
- KU Leuven - Belgium
- FAA Technical Center - USA

As for the previous years, the author of this report would like to thank to all partners from the academy and the research institutes that have collaborated with this compilation, and that will be cited along the report, and is particularly grateful to Professors Mariano Andrés Arbelo and Maurício Vicente Donadon, from the Aeronautics Institute of Technology (ITA) and to Professor Volnei Tita, from the University of São Paulo (USP), Professor Guilherme Ferreira Gomes, from Federal University of Itajubá (UNIFEI), Professor Maria Odília Cioffi, from State University of São Paulo (Unesp), Professor Carlos Baptista, from the University of São Paulo (USP), Professor José Alexander Araújo, from the University of Brasília (UnB), and many others, for their increasing support in current activities related to fatigue, fracture and structural integrity in aerospace structures and materials, and for their help during the organization of the report.

This report follows the basic structure applied to previous reviews, with minor subject modifications. During the reporting process, some collaborations were included in certain topics according to this structure, but it is recognized that they could be also included in other similar topics (for example, “analysis and simulation with composite materials” is partially “analysis and simulation” and partially “composite materials”), and therefore it is important that the reader checks the titles of all works included in the report regardless of the chapter where they were included.

2. CRACK GROWTH ANALYSIS AND SIMULATION

A mixed-mode energy-based elastoplastic fatigue induced damage model for the peridynamic theory (Ref. [1])

An elastoplastic constitutive damage model based on peridynamics formulation (Ref. [2])

Summary:

Peridynamic Theory based models allow simulating the initiation and growth of cracks in solid materials, without the aid of additional methods commonly employed in the conventional finite element formulation.

Within this context, a new elastoplastic damage model is proposed to use with the Peridynamic Theory. This proposed damage model combines Von Mises plasticity-based theory with a smeared cracking approach enabling damage prediction within an energy-based framework. The formulation incorporates a mixed-mode propagation criterion to account for the effect of both axial and shear stresses in the simulation, which in turn allows prediction of damage progression in ductile materials under multiaxial loading without knowing *a priori* the mode mixity ratio. This proposed damage modeling approach can be used within any constitutive peridynamic model, by relying on the displacement field obtained in the simulation.

Highlights:

Peridynamics is a nonlocal extension of continuum mechanics, in which in contrast to the classical approaches, the balance of linear momentum is formulated as an integral equation that remains valid in the presence of material discontinuities such as cracks. Within the peridynamics framework, a material point interacts directly with all neighboring material points within a finite distance, termed the horizon. The vectors connecting the point to its neighbors are referred to as bonds.

These papers propose a novel elastoplastic constitutive damage model based on the Peridynamic Theory. The extracts in this report are based on the second paper.

The proposed damage model combines Von Mises plasticity-based theory with a smeared cracking approach within a unified way accounting for effects of the axial and shear stresses, to compute the contribution of the mode I and mode II on the crack propagation process in ductile materials. To the best of the authors' knowledge, this kind of novel damage model for peridynamics is first proposed here. The results obtained with the proposed model are compared to experimental results published in the literature.

The paper brings a review of the state-based peridynamic constitutive model, with the plasticity correction procedure and the stress and strain calculation procedure.

The proposed elastoplastic damage model is presented along with a discussion about the numerical simulations and verification cases and concluding remarks.

In the report, from the various validation examples developed and published in both papers, one example case is presented. For this problem, two middle tension specimens of aluminum 7075 temper T6 are simulated under two different cyclic stresses condition: a low-stress condition (L.S.) of $\sigma_\infty = 30\text{MPa}$, and a high-stress condition (H.S.) of $\sigma_\infty = 414\text{MPa}$, according to Figure 1.

The numerical predicted damage paths for both load conditions are given in Figure 2. For the problem under the high-stress loading condition, the numerical results for the crack propagation compared with the experimental results presented in are shown in Figure 3.

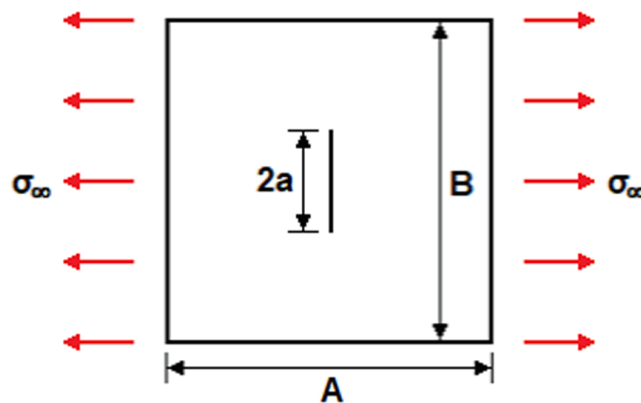


Figure 1 - Plate with a central crack subjected to mode I crack growth.

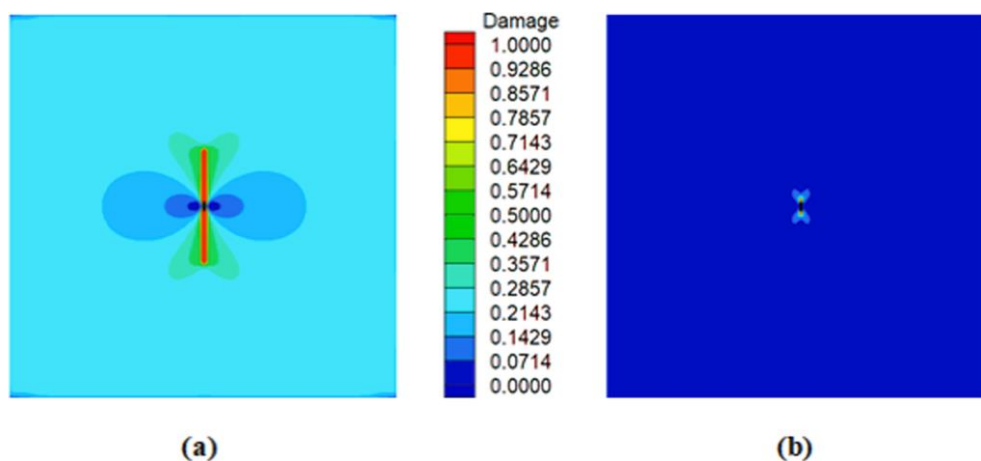


Figure 2 - Predicted smeared damage contours for a pure mode I simulation for: (a) low-stress loading condition, (b) high-stress loading condition.

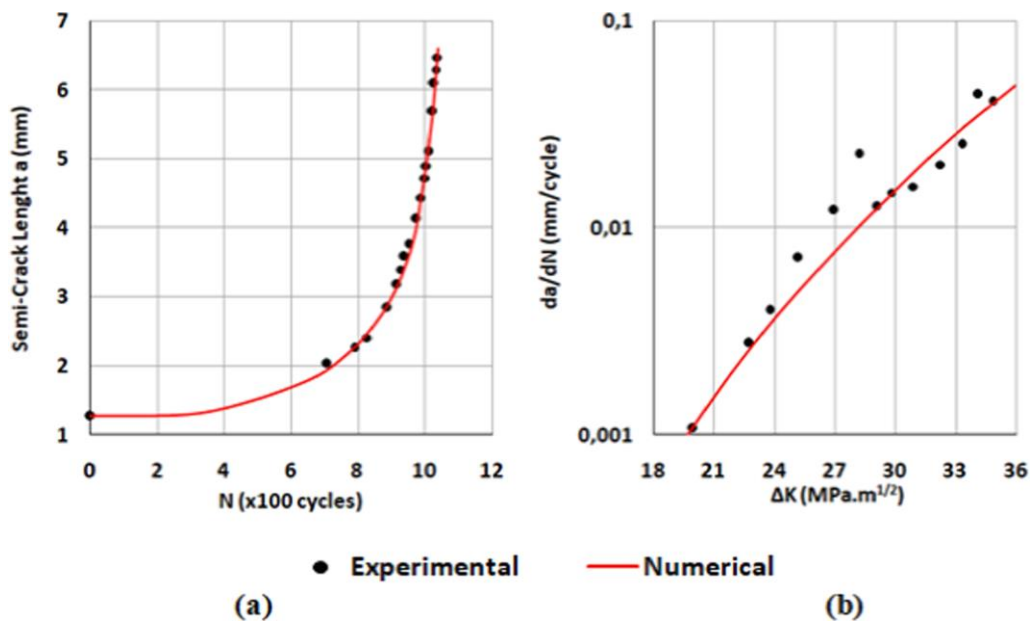


Figure 3 - Crack growth curves for mode I loading under the high-stress loading condition: (a) $a \times N$, (b) $da/dN \times \Delta K$.

As can be observed, the results brought by the FORTRAN code are very close to the experimental results for both loading conditions. The low-stress loading condition propagates the crack mostly under the elastic region of the stress-strain relationship for the aluminum 7075-T6, while the crack for the high-stress condition mostly propagates under the plastic region. Even though both cracks propagate mostly under different regions, the model correctly predicted the propagations for both problems.

Extraction of Stress Intensity Factors via the displacement correlation method from stable generalized finite element solutions (Ref. [3])

Summary:

This work presents and discusses the Stress Intensity Factors (SIF's) calculation using the Displacement Correlation Method (DCM) coupled to a Stable Generalized Finite Element Method (SGFEM). Moreover, the improvement of the results using the Stable Generalized Finite Element Method (SGFEM) instead of the Generalized Finite Element Method (GFEM) is also investigated. In these methods, in general, enrichment functions are applied to represent the effects of the singularity attached to the crack tip and the discontinuities introduced by the crack. Beyond that, the enrichment functions in the SGFEM are modified to avoid some problems that appear in the GFEM, as round off errors due to ill conditioning of the stiffness matrix, which can affect the convergence of the model. The DCM was chosen due to his low computational cost compared to other methods based on energetic

approach such as the J integral. Such features can be explored to implement fast crack growth simulations models using the SGFEM. Practical examples with closed form solution, considering different opening modes, are used to compare SIF's extracted using both SGFEM and GFEM methodologies. These examples include horizontal and inclined cracks aiming to demonstrate the robustness of the proposed technique.

Highlights:

First, the GFEM and SGFEM are outlined, together with some usual methods for SIF calculation. Then, three benchmark problems are discussed: (i) tensile edge crack, (ii) shear edge crack and (iii) inclined centered crack. Figure 4 shows the adopted mesh with its respective enriched nodes for the problem with inclined centered crack. Linear Heaviside enrichment functions were applied on the nodes surrounding the crack.

Figure 5 shows the relative error between the calculated SIF and the one extracted from the open literature for the analyses performed for inclined centered crack using only the DCM applying the linear least square extrapolation technique described above. The reference values were extracted from Marukami (Ref. [4]).

It could be concluded that the SGFEM generated consistent results when compared with results obtained from close form solutions available on the open literature. Furthermore, in most cases, when the DCM is applied combined with least linear square extrapolation techniques, the SGFEM provided more accurate results than its predecessor, the GFEM. Furthermore, it is demonstrated that, despite of the simplicity involved at its formulation, when compared to the other extraction techniques, the application of the DCM provided results that are close to the references when combined with the linear least square extrapolation technique.

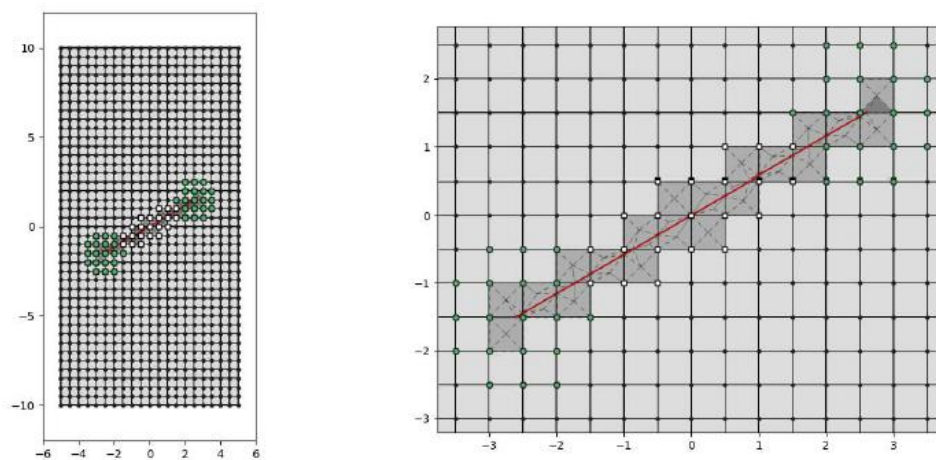


Figure 4 - Centered inclined cracked panel. Green nodes enriched with Branch Functions and red nodes enriched with Linear Heaviside Functions.

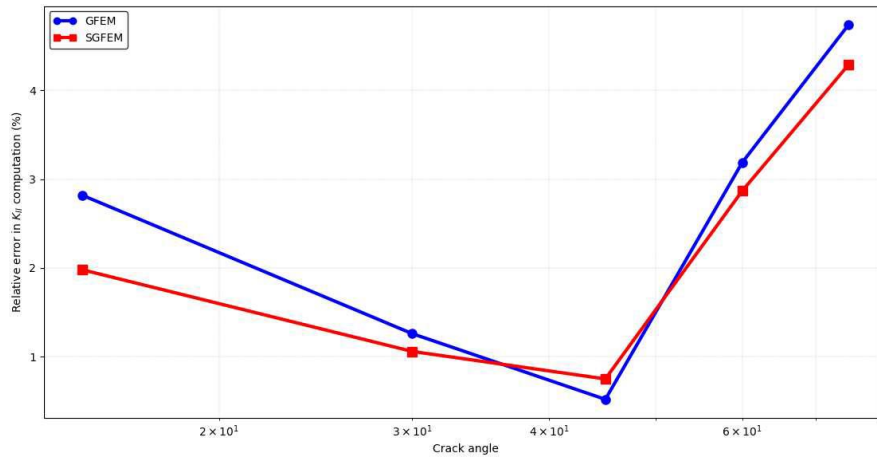


Figure 5 - SIF comparison between GFEM and SGFEM - Mode II - Inclined centered crack.

3. METALLIC MATERIALS AND STRUCTURES

This chapter will be divided in five sections, reflecting the contributions during this period:

- (i) fatigue and fracture properties,
- (ii) fretting fatigue,
- (iii) mechanical processes and surface treatments,
- (iv) metallic structures (reflecting tests and analyses of larger sub-components, components, and full-scale structures) and
- (v) structural health monitoring (SHM).

Fatigue and Fracture Properties

The effect of retardation due to overloads in fatigue crack growth (Ref. [5])

Summary:

This work is an experimental study focused on the characterization of fatigue crack propagation, considering the interaction between overloads and the retardation effect. An experimental test matrix was created based on plates made of aluminum with an initial central crack under Mode I loading. The aluminum alloy 2524-T3 was selected because it is a material commonly applied in fuselage structures due to its lower fatigue crack propagation rate when compared to other traditional aluminum alloys used in the aeronautical industry such as the 2024-T3, among others.

A review of the state of the art was conducted to identify the main crack propagation models and those related to the addition of retardation effects due to overload and plasticity on the crack tip. The Walker and Forman models were adopted for this work to characterize the propagation curves and the Willenborg and Wheeler models to quantify the retardation effect and overload interaction on fatigue life. The overall experiment followed a test matrix created to quantify the adjustment parameters of the models chosen, as follows:

- (i) tensile tests to characterize the mechanical properties of the material and the stress-strain curve in the elastoplastic regime;
- (ii) cyclic loading and constant amplitude tests for two loading ratios, to obtain the coefficients of the adopted propagation models;

- (iii) cyclic loading tests with decreasing amplitude for characterization of the fatigue crack growth threshold, aiming at the expansion of the propagation and retardation models studied;
- (iv) cyclic loading and constant amplitude tests, with one single overload, to characterize the coefficient of the Wheeler retardation model;
- (v) tests with multiple overloads to evaluate the effect of interaction between the plastic deformation fields during fatigue crack propagation and for verification of the propagation and retardation models considered in this work.

After the analysis of correlation between the models and experimental results, it was possible to observe an adequate fit of the propagation curves, considering the interaction of overloads when the Wheeler retardation model is coupled with any of the propagation models considered in the work.

Highlights:

Figure 6 shows an overview of the specimens tested and test setup. For the cyclic loading tests, thirteen specimens with nine loading configurations were employed for this test campaign. Different numbers of overloads and magnitudes of overloads were investigated. The stress ratio was $R=0.1$. Configurations 01 to 03 were applied to obtain the Wheeler coefficient after the application of a single overload. Configurations 04 to 06 were tested to evaluate the influence of the first overload when two overloads are applied, without interference between plastic zones, and Configurations 07 to 09 were tested to evaluate the retardation when there is intersection between plastic zones for two overloads. This test strategy is summarized in Figure 7.

Figure 8 shows a set of test results applied to obtain the Wheeler coefficients, in this case with an overload of 13 kN applied, while Figure 9 presents selected results corresponding to Configuration 04, where two overloads of 15 kN were applied at 14 mm and 16.5 mm of crack average length.



Figure 6 - Test machine with specimen and instrumentation installed.

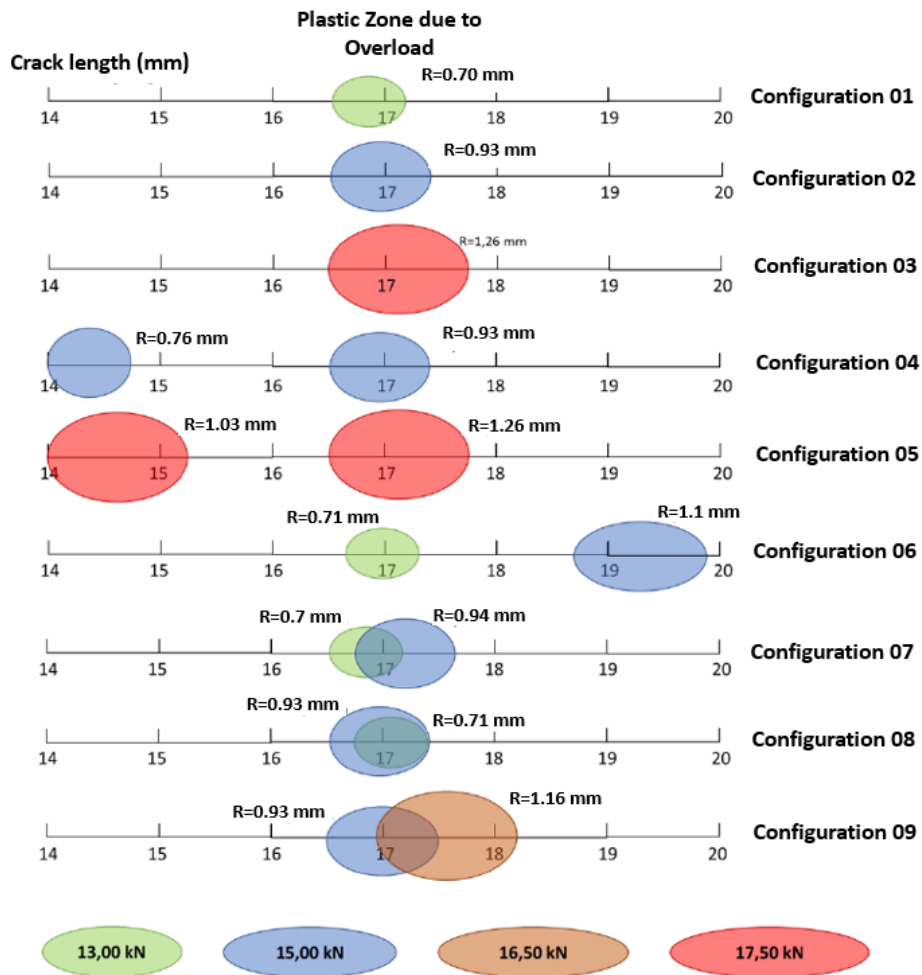


Figure 7 - Test matrix - number of specimens and overloads applied.

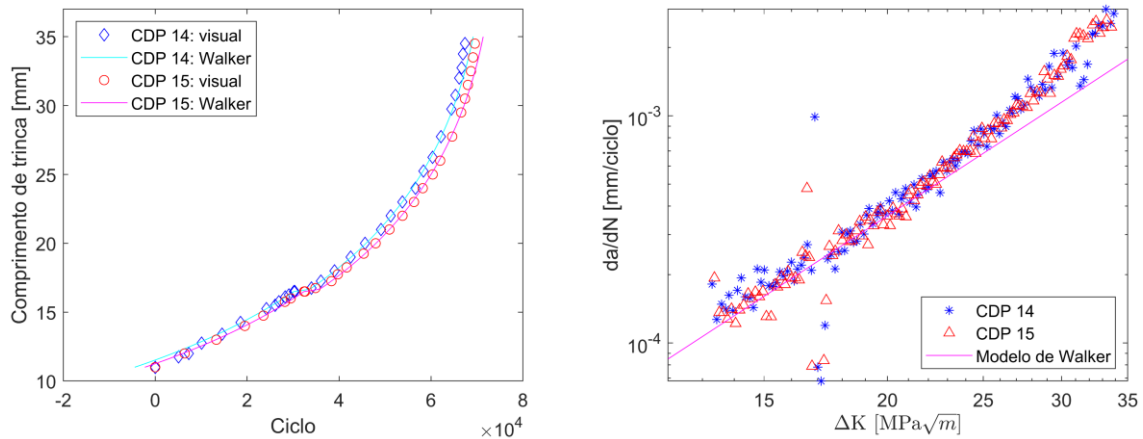


Figure 8 - Crack growth curves for specimens corresponding to Configuration 01 (single overload $P = 13$ kN, vertical axis in left plot corresponds to measured crack length).

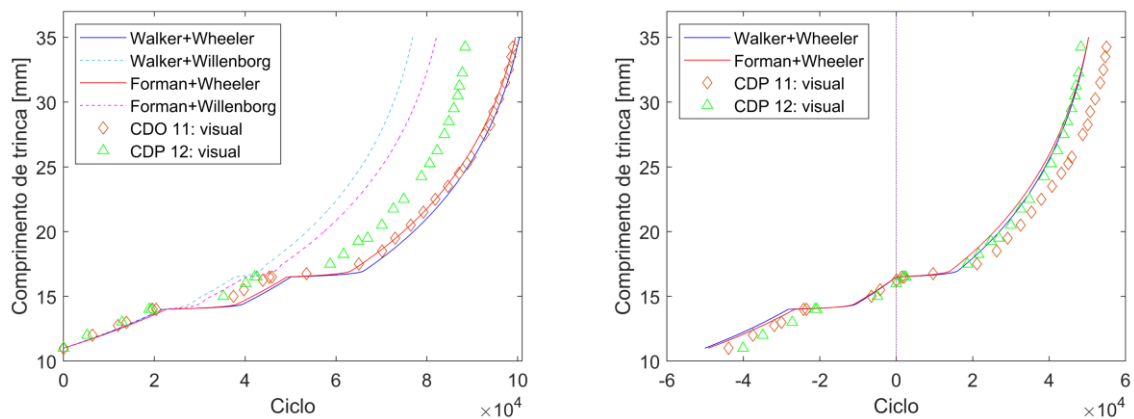


Figure 9 - Test results and model fit for Configuration 04 (vertical axis corresponds to measured crack length).

Crack growth retardation models under load interaction (Ref. [6])

Summary:

This work was developed together with the one presented above, and also aims to investigate the load interaction effects during fatigue crack propagation under the presence of overloads. The retardation models capable of representing the effects of plastic deformation on crack growth were identified, implemented, and verified using experimental results available. A modification of the Newman model is proposed and validated to allow the study of loads of variable amplitude with interacting overloads.

Then an analytical study shows the advantages of each methodology, the implementation challenges in each case, and its limitations when applied to aeronautical structures under variable amplitude loading. The validation of the results of each model is carried out from experimental results, using specimens made of material Al 2524-T3, which is widely used in structures of Embraer E2 series aircraft, the new generation of E-jets for commercial aviation. The results obtained for the material for the given boundary conditions indicate that the Wheeler model correlates adequately in the presence of overload since its empirical parameters are appropriately calibrated. The Willenborg and Gallagher models resulted in unsatisfactory crack propagation predictions, being recommended only for application in cases with a high load ratio. The modified Newman model developed in this work can represent the retardation effect without the need to adjust additional empirical parameters if it is submitted to a shut-off value lower than 1.5. Furthermore, other usage recommendations are indicated for each methodology.

Fretting Fatigue

Among the contributions received during this period, there were a number of high-level research activities related to fretting fatigue from the University of Brasilia (UnB) and coordinated by Professor José Alexander Araújo. These activities may be divided in three main groups, as follows:

1. Development of a four actuators fatigue fretting rig and tests for Ti-6Al-4V under multiaxial loading conditions, under room and high temperature conditions;
2. Development of a generalized ANN-multiaxial fatigue nonlocal model to estimate fretting fatigue life for aeronautical Al alloys;
3. Fretting fatigue under variable amplitude loading.

A selection of the main contributions referring to each of these three groups of research activities will be summarized along this section. Additional information about the third group will also be presented by the author during the ICAF Conference.

Additionally, a comprehensive fretting fatigue review article, published in 2023 by Professor Araújo and co-authors may be found in Ref. [7]. This article covers a range of topics, including some typical industrial applications, experimental configurations, and different analytical approaches related to fretting.

Four actuators fretting fatigue rig and tests with cyclic normal load for Ti-6Al-4V (Ref. [8])

Experiments, modelling and analysis of fretting fatigue for Inconel 718 and Ti-6Al-4V under time-varying contact normal load at room and high temperature (Ref. [9])

Summary:

In this work, a new four actuators fretting fatigue rig is presented. This machine is capable of performing tests at high or room temperature. Further, it is possible to independently control all the loads involved in the fretting tests (bulk, normal and tangential loads) in a static and cyclic way. In order to evaluate the influence of cyclic normal load on the fretting case, a new set of fretting fatigue and coefficient of friction tests were carried out for the Ti-6Al-4V alloy. Also, a finite element model (considering and neglecting wear) was used in conjunction with a critical plane parameter (SWT) and a non-local stress averaging approach to estimate fretting life. The experimental results have shown that cyclic normal load has a beneficial effect on fretting life compared with those under constant normal load. Further, no significant difference was noticed for the coefficient of friction measured under static and cyclic normal load conditions. Concerning the life estimate approaches considered in this work, for the constant normal load case, both implemented methodologies, whether accounting or neglecting wear, provided satisfactory results, with the former being slightly more accurate. However, life estimates were more accurate for the cyclic normal load case when disregarding wear.

Highlights:

One of the main objectives of this thesis was to upgrade the previous version of the UnB's fretting fatigue rig to work with cyclic normal load and high temperatures. The previous configuration of such a rig was already composed of two vertical actuators capable of independently applying fatigue bulk and tangential load. However, the normal contact load was applied only statically. Besides that, it would not be possible to attach a heating and cooling system to it.

In this way, to reach the goals of this work, a new fretting apparatus was specially developed to overcome all limitations of the previous one. The new normal load application system, the heating, and cooling systems were designed and successfully tested.

At the present moment, it can be considered one of the most versatile fretting fatigue machines globally. It is capable of applying the contact normal loads up to 15kN, tangential loads up to 100kN, and fatigue bulk loadings up to 250kN, dynamically. Furthermore, all four MTS hydraulic actuators are uncoupled and controlled by a new MTS FlexTest 60 controller. Also, all these loads can be applied

in-phase or out-of-phase, and tests can be carried out at temperatures up to 750°C. The Fretting Fatigue machine can be seen in Figure 10 and its schematic view in Figure 11. The forces, displacements, and temperature ranges of this experimental rig are reported in Table 1.

Table 1 - Forces, displacements, and temperature ranges of the new four actuators high temperature fretting fatigue rig.

| | Force range [kN] | Displacement range [mm] |
|-------------------------------|------------------|-------------------------|
| Fatigue actuator | ±250 | ±80 |
| Fretting actuator | ±100 | ±75 |
| Contact normal load actuators | ±15 | ±25 |
| Testing temperature | up to 750 °C | |

Regarding experimental tests, in this work an experimental campaign was especially designed to evaluate the influence of a varying contact normal load on the fretting fatigue strength for the Ti-6Al-4V and Inconel 718 alloys. In this way, two sets of tests were performed. The first one (Testing Set 1), with constant contact normal load and the second one (Testing Set 2) with cyclic contact normal load. Figure 12 shows an overview of the specimens used.

As main results and conclusions of this research work,

- (i) the new fretting fatigue apparatus was designed and successfully performed fretting fatigue tests with static and cyclic contact normal load at room and elevated temperatures,
- (ii) based on the experimental results, the presence of the cyclic contact normal load in the fretting tests provoked an advantageous effect on the specimens durability for both materials under study and at room and high temperatures, although these results should not be generalized for every material, temperature and loading condition,
- (iii) the increase of temperature from 20°C to 540°C lead to 39% reduction in fretting life for the Inconel 718 specimens under constant contact normal load (Testing Set 1),
- (iv) The available life methodologies considered in this work (non-local multiaxial fatigue) to estimate the fretting fatigue lives under the more challenging test conditions used in this work proved to provide life estimates within a factor of three. Therefore, they are capable to capture the effects of varying contact normal loading and temperature in fretting fatigue. Surely, to generalize such a conclusion, more tests are required.

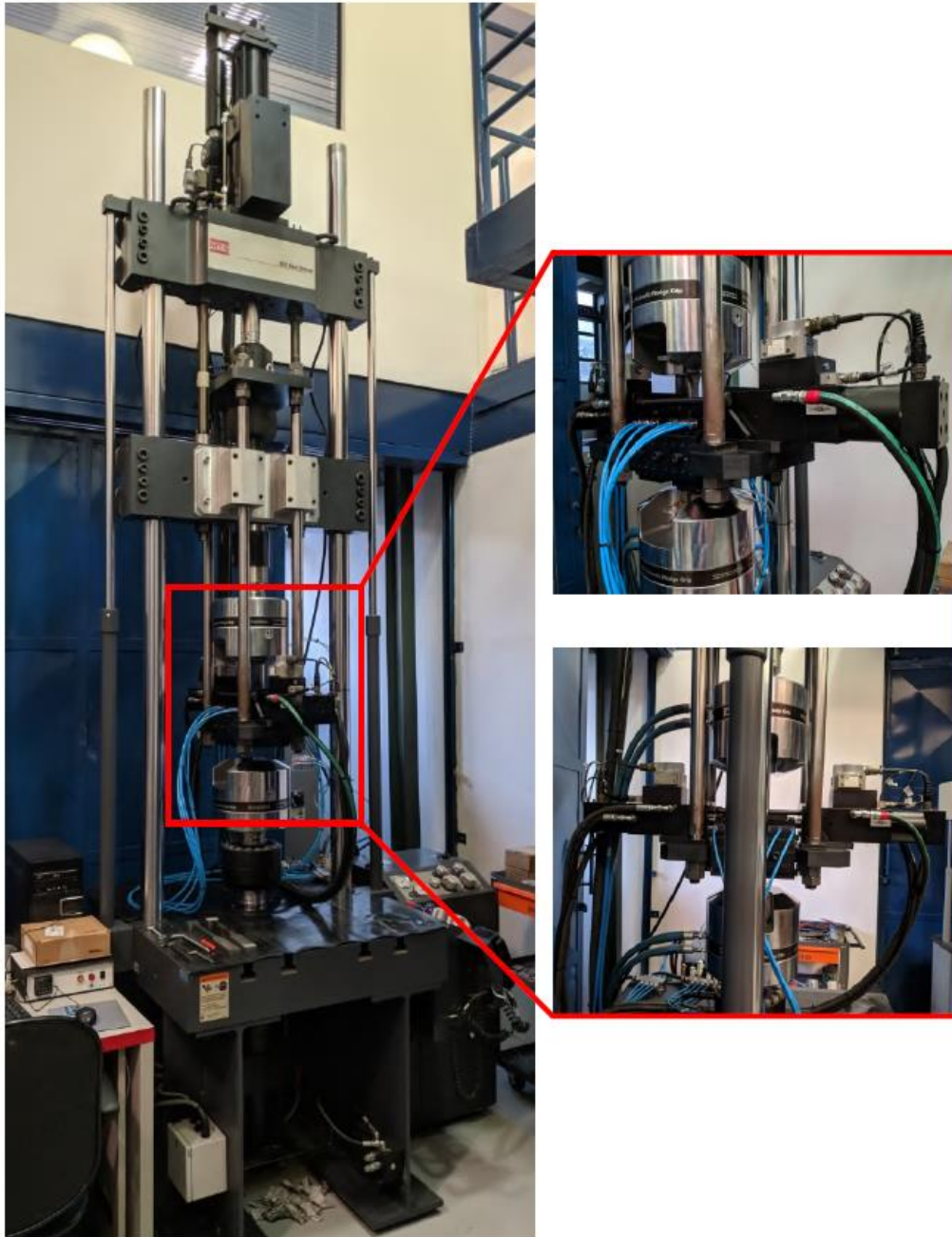


Figure 10 - New Fretting Fatigue Machine of the University of Brasilia (UnB).

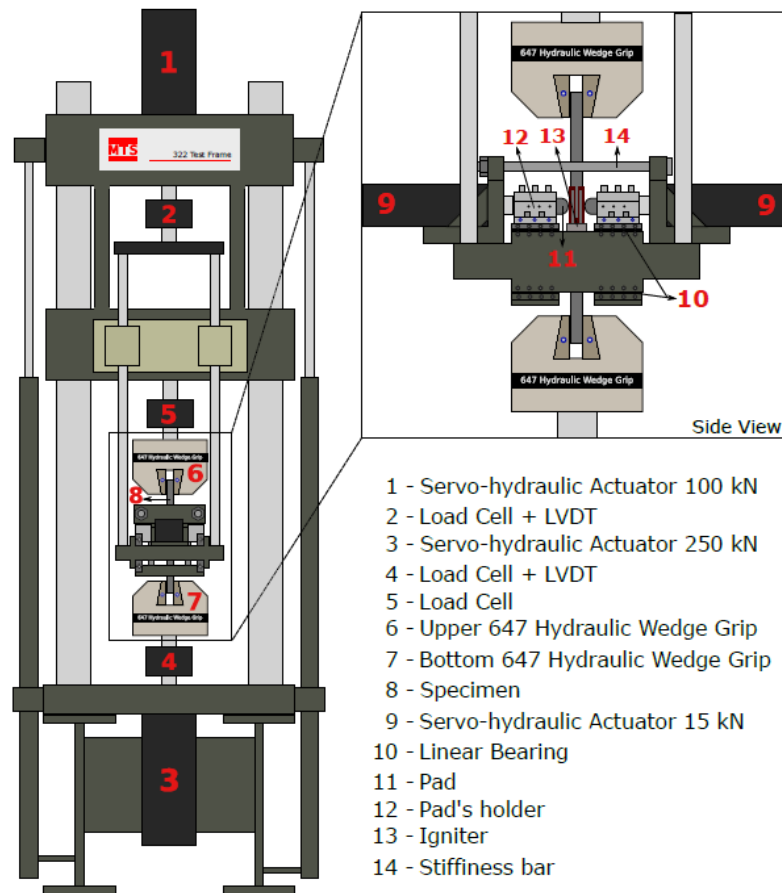


Figure 11 - Schematic view and component list of the new Fretting Fatigue Machine of the University of Brasilia (UnB).

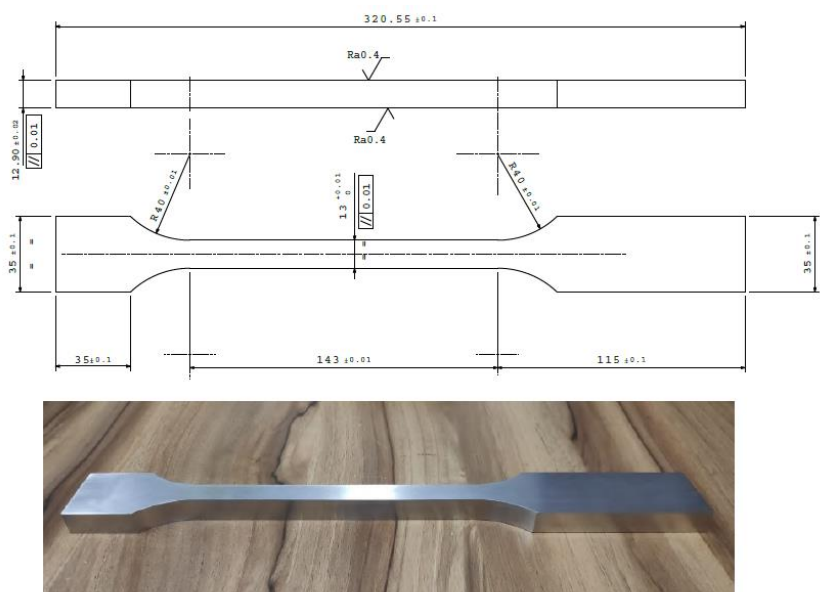


Figure 12 - Photo and dimensions of the fretting specimens.

A hybrid ANN-multiaxial fatigue nonlocal model to estimate fretting fatigue life for aeronautical Al alloys (Ref. [10])

Summary:

This work presents two new models, based on the use of Artificial Neural Networks (ANN) and non-local stress parameters physically related to crack initiation processes, to estimate fretting fatigue (FF) life. To train and validate these models, several FF data for different aeronautical Al alloys are gathered in the literature. To test the accuracy and generalization capability of the models, data related to two Al alloys not considered in the training phase are employed and life estimates are compared with those computed according to two well established multiaxial fatigue models. The ANN models provide more accurate estimates than those provided by the fatigue models examined, as well as showed a good generalization capability, which suggests their potential for future industrial applications.

Highlights:

Along with this work, the following subjects were discussed: some basic concepts about the two multiaxial models considered, i.e., the Modified Wöhler Curve Method (MWCM) and the Smith, Watson, and Topper (SWT) model are presented, as well as the so-called Theory of Critical Distances (TCD). Then, some basics concerning ANNs are addressed. In addition, the main parameters used as inputs of the ANN models are presented. All the experimental data collected from the literature are described. Finally, the work presents the numerical framework considered for obtaining FF stress solutions and the results obtained by applying the calibrated multiaxial models, the ANN models, and a comparative analysis is performed. In this report, only a few key information and results will be presented.

Figure 13 shows a flowchart where all the followed steps are divided into three phases. Phase I represents the pre-processing of the data, with the experimental data collection, the equivalent stresses computation, normalization of the results and selection of the three main datasets (training, test, and query data). Phase II is the ANN training phase, here the training and the test data are applied in the ANN and the training algorithm is used to minimize the empirical error through cross-validation, finally capturing the best values for the weights. In Phase III, these obtained weights are used to create a function capable of estimating the fretting fatigue life.

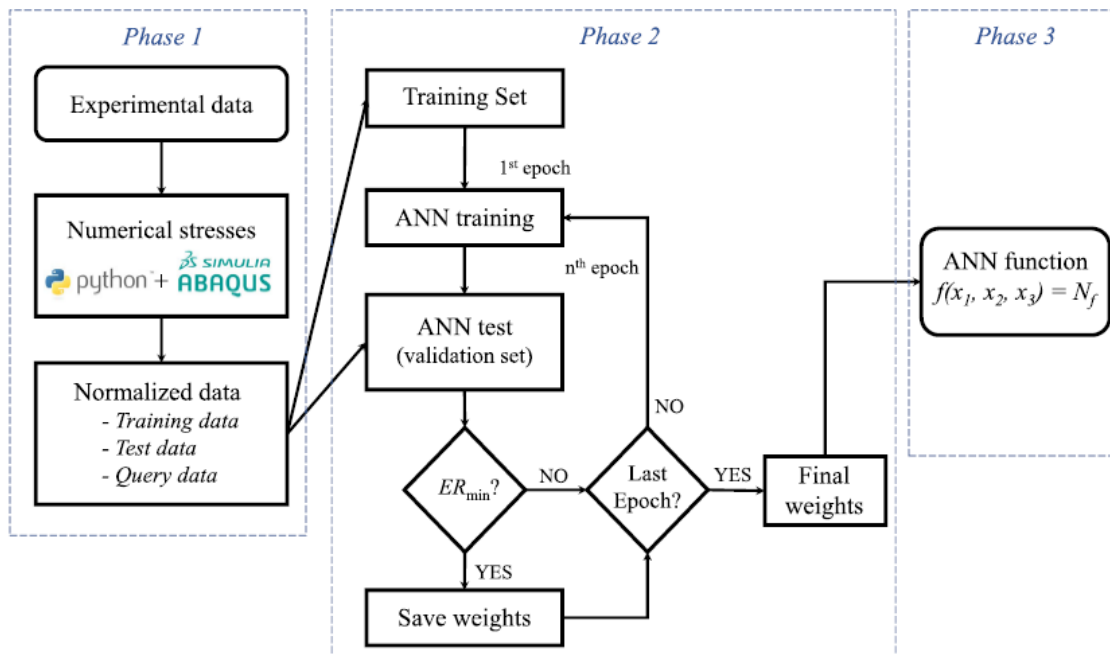


Figure 13 - Flowchart illustrating all the process to construct the ANN models.

Experimental uniaxial fatigue data for the 2024-T3 and 7075-T6 Al alloys were used to calibrate the SWT and MWCM multiaxial fatigue models. Expressions relating the SWT parameter with the number of cycles to failure are given in Figure 14(a) for the 2024-Al alloy. For the MWCM, Figure 14(b) shows the τ_a vs. N_f curve for the two aforementioned alloy.

Experimental vs. estimated fatigue life plots for the ANN_Shear and ANN_Normal models are showed in Figure 15(a) and (b), respectively. The solid black lines represent the exact estimates and the dashed ones the factor of two error boundaries. The blue squares, the red triangles and the green diamonds represent, respectively, the training, test, and query data. As can be observed, both models proved themselves promising by providing most of the life estimates for the query data within the error factor of two. Such results confirm the proposed methodologies' capability of accurately handling material, geometry and loading conditions other than those used in the ANN training.

Fatigue life can also be estimated by utilizing the SWT and MWCM multiaxial fatigue models for the fretting fatigue tests conducted on the 2024-T3 and 7075-T6 Al alloys (query data). Results for the 2024-T3 alloy are presented in Figure 16.

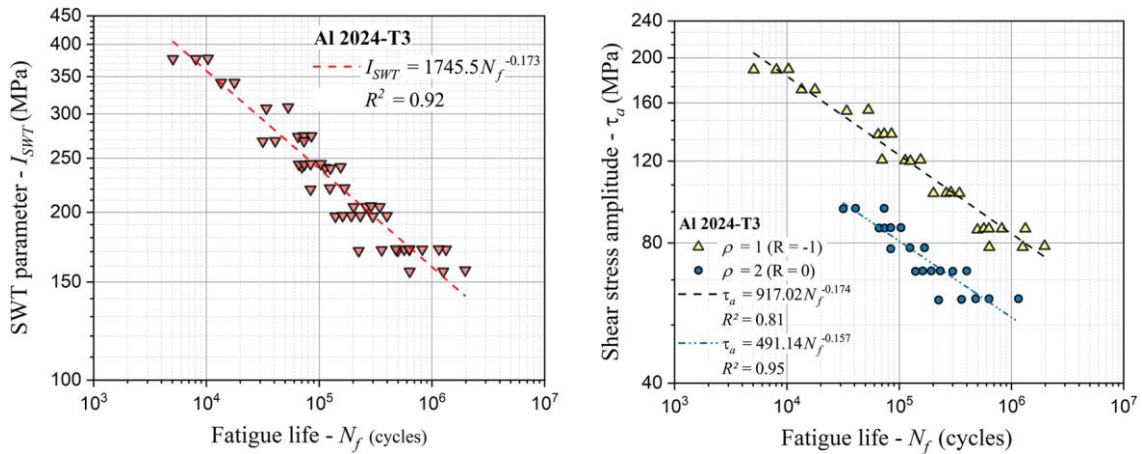


Figure 14 – (a) SWT parameter versus fatigue life for the 2024-T3. (b) Modified Wöhler curve for the 2024-T3.

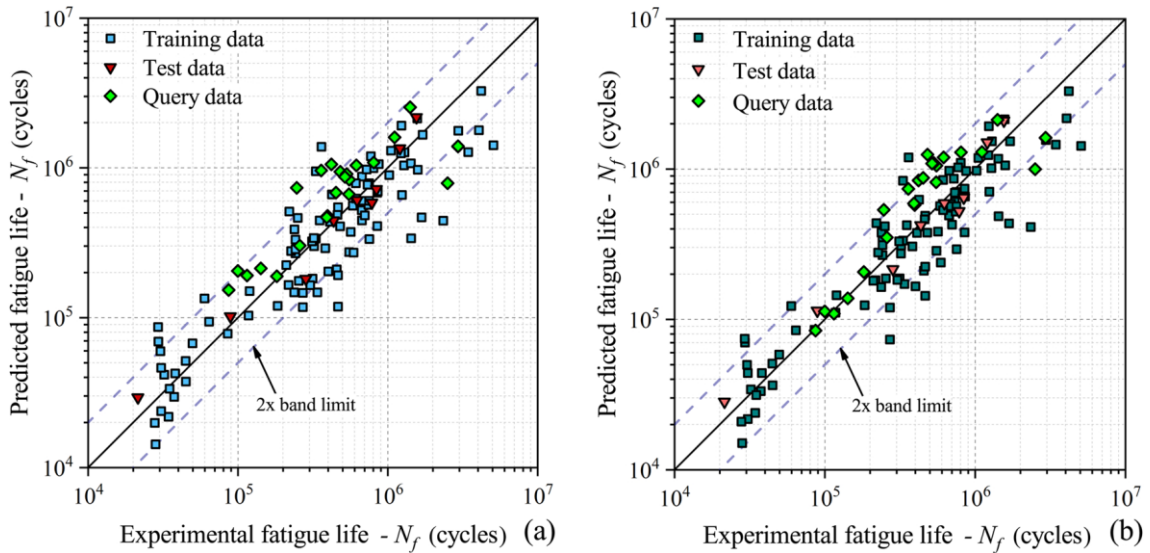


Figure 15 - Estimated fatigue life by the ANN_SHEAR model vs. the experimental one (a). Estimated fatigue life by the ANN_NORMAL model vs. the experimental.

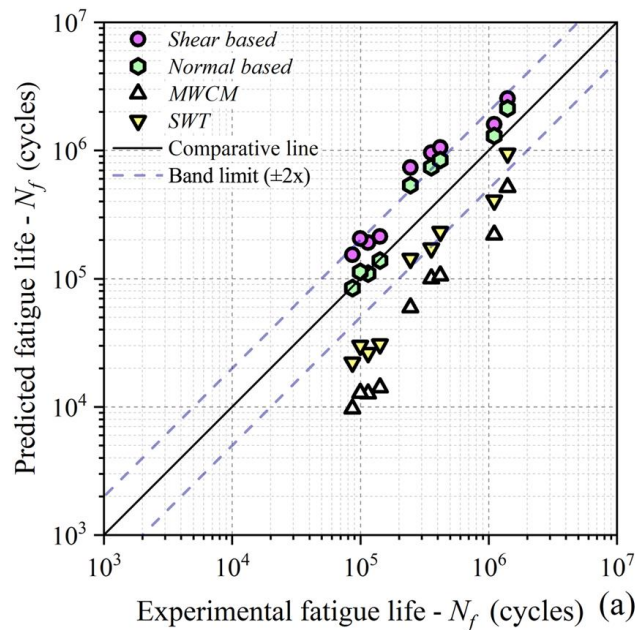


Figure 16 - Estimated fatigue life considering all the models vs. experimental data for 2024-T3 alloy.

Fretting fatigue under variable amplitude loading (Ref. [11])

Summary:

Generally, the fretting fatigue problem is treated with constant amplitude loading. However, this condition is not the reality for industrial applications. Although there are few studies on fretting fatigue under variable amplitude loadings, they use a simplistic approach to life estimation (unable to capture the effects of the complex multiaxial and non-proportional stress field that exists under the contact interface) and only the bulk fatigue load has its amplitude alternating.

The objective of this work is to propose a numerical methodology for the life assessment of components subjected to fretting fatigue under variable amplitude loading and to study the effects of these loads. For this, experimental tests were carried out by applying H-L (High-Low) and L-H (Low-High) loading blocks to the tangential load, that is, the contact normal load and the amplitude of the bulk fatigue load were kept constant while the tangential load has its alternating amplitude.

The numerical methodology proposed for fretting fatigue life assessment includes the wear effect and crack propagation. The multiaxial fatigue parameter SWT, the theory of critical distance TCD, and Miners' linear rule were used to compute the damage in the crack nucleation phase. The node-displacement algorithm based on Archard's law was applied to account wear. In the crack propagation phase, the CDM (critical direction method) was used to estimate the crack initiation angle

considering the worn contact surface, and then the crack is modeled and propagated.

The still limited range of experimental data done in this work for fretting fatigue under varying loading blocks seems to indicate that the loading sequence has an effect on the accumulated fatigue damage, mainly to the H-L loading sequences. Based on this observation, a new non-linear damage model was proposed. Using this new damage model, the life estimation results were within a scatter band of 1.2.

Highlights:

The first part of this work is a background of the fatigue problem, fretting fatigue, multiaxial fatigue theories, fracture mechanics, contact mechanics, wear modelling and damage accumulation.

The second part presents the experimental results for the characterization of aluminum alloy Al 7075-T651 and discusses the experimental methods used to study fretting fatigue behavior under variable amplitude loading, with a very detailed description of the fretting tests, from which some two-block test schemes were investigated (Figure 17). Besides this material, others whose data was available in the literature were also assessed.

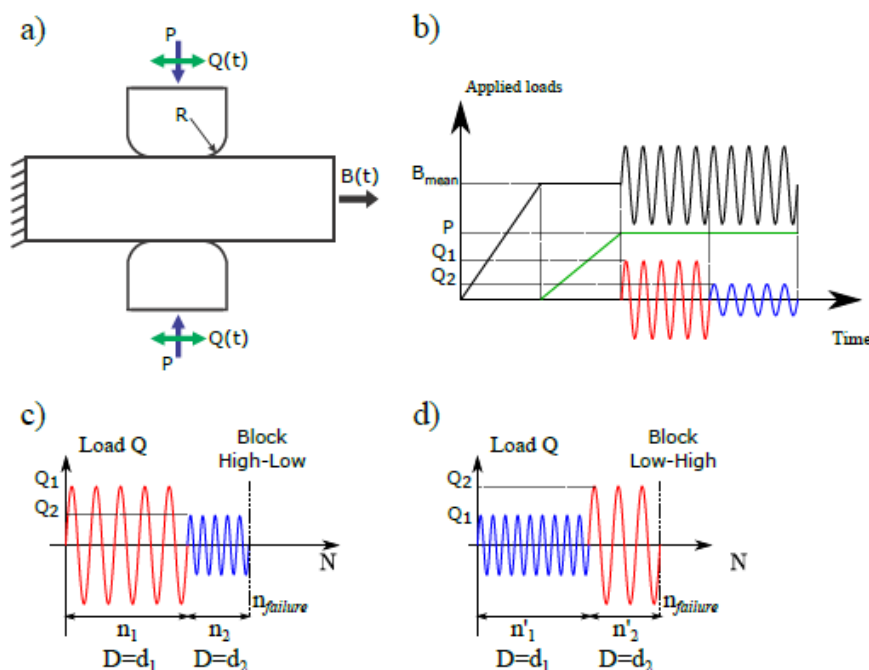


Figure 17 - Schematic representation of the application of loads in the fretting fatigue test: (a) representation of where each load is applied to the specimen,(b) order of application of test loads, and the representation of the H-L (c) and L-H (d) loading blocks.

The third part of the work proposes a new methodology for fretting fatigue life assessment. It uses a combination of multiaxial fatigue criteria, the theory of critical distances and a node-displacement wear algorithm to account for the initiation life under fretting. A new method is also introduced to predict the crack propagation path under nonproportional loading conditions.

A FE model was developed for the analyses, as outlined in Figure 18, where P is the normal load and Q is the tangential load applied. Additionally, XFEM models were developed for calculation of crack paths. Then the fretting fatigue lives were estimated with and without the crack propagation, and compared with experimental results.

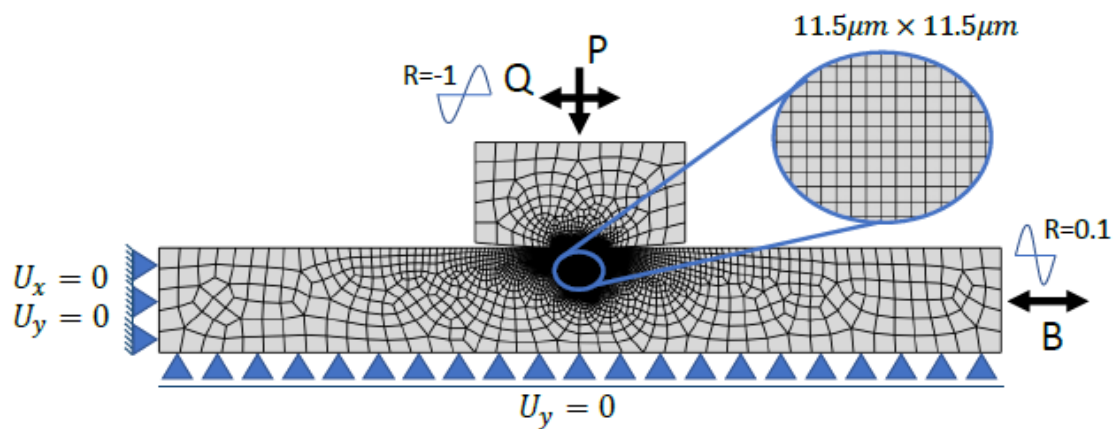


Figure 18 - FE model for the fretting fatigue problem.

In the fourth part of the work two different methods to predict crack initiation direction in fretting problems subjected to partial slip conditions are investigated. In addition, the influence of considering wear in the crack initiation direction estimates is also investigated. These methods are the Critical Direction Method and the Method Based on LEFM.

Finally, a robust numerical methodology for accessing component life under fretting fatigue conditions is presented in this chapter. This method is applied to fretting fatigue under variable amplitude load and validated with experimental results.

This work led to five publications in high impact journals, one publication in peer reviewed conference proceedings, and four additional publications in conference proceedings. More details about the work will be presented during the ICAF 2023 Conference and Symposium.

Mechanical Processes and Surface Treatments

Numerical and experimental analyses of the stress field ahead of fatigue cracks in laser-treated AA2198-T851 alloy (Ref. [12])

Summary:

Techniques such as shot peening, cold expansion and laser shock peening are well-known in the aircraft industry as residual-stress-based approaches. Compared with the latter, laser heating is a less expensive technique, because it can be applied with continuous wave laser equipment; and it has been successful in reducing fatigue crack propagation rates in laboratory specimens. Although this effect is usually related to the original residual stress field, it is known that cyclic loading and crack growth can cause relaxation and redistribution of residual stresses.

In this work, M(T) specimens made of 2.0 mm thick AA2198-T851 alloy sheets with L-T and T-L crack orientations were treated with a fiber laser (power 200 W, displacement speed 1 mm/s) to produce two heating lines ahead of each of the crack fronts, on one of each specimens' face. The specimens with and without laser treatment were tested under constant amplitude loading at a ratio of $R = 0.1$. Electrical resistance strain gages bonded along the crack path right next to the first heating line on the treated specimens and in a similar position on the non-treated ones were employed to register the deformation behavior ahead of the approaching crack tip.

Additionally, a numerical model for the stress-strain state ahead of the fatigue crack considering an elastoplastic material with strain hardening behavior was developed. From the symmetry condition, half of the specimen was discretized with plane quadrilateral finite elements of linear order. The constitutive model included plane-strain conditions, linear elastic response, the anisotropic Gurson-Tvergaard-Needleman (GTN) yield criterion coupled with damage, associative plastic flow rule and nonlinear isotropic hardening Swift model. The mesh refinement was concentrated around the crack-tip and strain gauge regions. Numerical simulations were successful in describing the measured strain behavior in the as-received specimens. The experimental results showed significant fatigue crack growth retardation experienced by the laser-treated specimens; this effect was more pronounced in the L-T orientation. Thereafter, the model was calibrated with imposed average compressive stresses to reproduce the experimental deformation behavior ahead of the crack tip, qualitatively showing how crack extension affects the residual stress field.

Highlights:

Some relevant results from this investigation are presented below.

The specimen dimensions, including the heating lines position, are shown in Figure 19. The two promising laser heating conditions (laser power 200 W and speeds of 1 mm/s and 10 mm/s), from here referred to as L01 and L10, were adopted for the fatigue crack growth tests in a comparative study with the as-received (AR) material. The raw fatigue crack growth data obtained in the tests with load ratios $R = 0.1$ (with $P_{max} = 800$ N), as plotted in Figure 20.

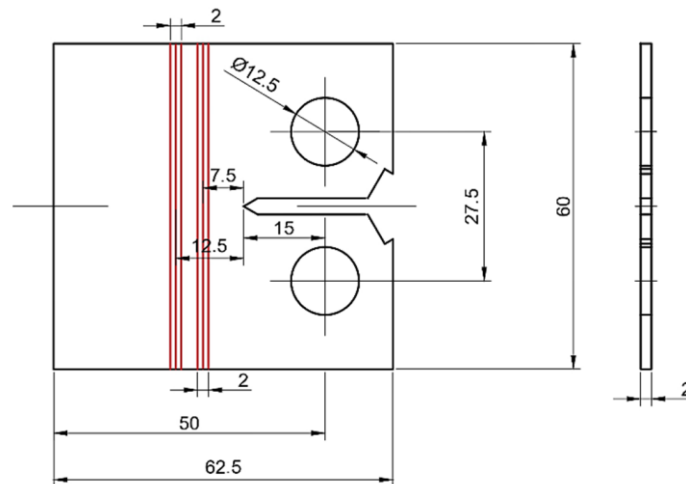


Figure 19 - Geometry and dimensions (mm) of the FCG specimens, including laser lines positioning.

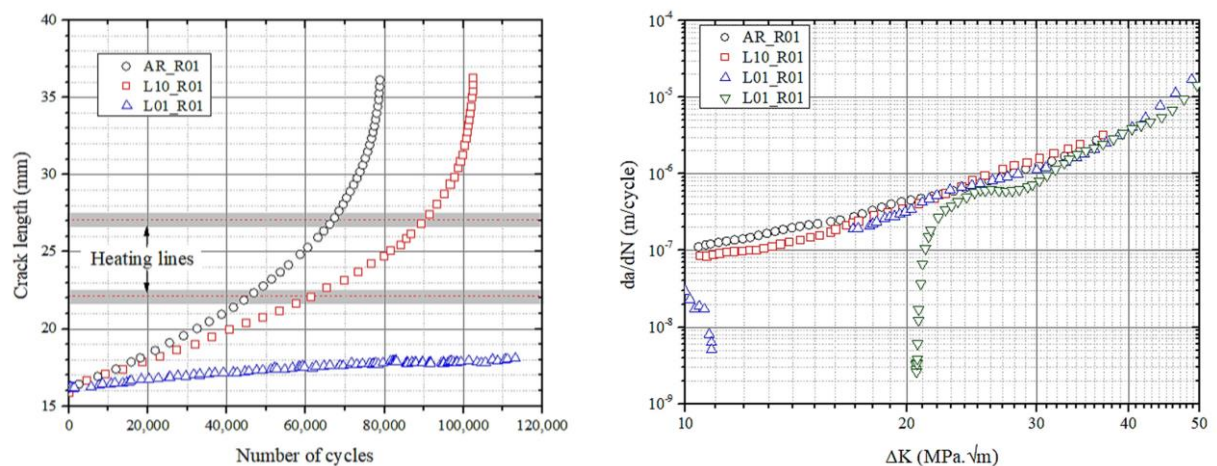


Figure 20 - FCG test results: (a) crack length vs. number of cycles for $R = 0.1$, (b) crack growth rate da/dN vs. ΔK plots for $R = 0.1$.

Effects of the secondary aging heat treatment T6I4 on fracture toughness and fatigue crack growth resistance of AA7050 alloy (Ref. [13])

Summary:

The tensile response and the fatigue behavior of aircraft age-hardenable aluminum alloys are strongly influenced by factors like the size, spacing and volume fraction of strengthening precipitates. Recent papers have pointed out that the secondary aging T6I4, by producing a higher density of fine strengthening precipitates as compared to the conventional T7451 temper, can improve the ability of AA 7050 alloy to accommodate plastic strain during loading and promote a more uniform strain distribution. In this sense, this work has as main goal to evaluate the effects of T6I4 aging on the fracture toughness and fatigue crack growth behavior of AA 7050 plate samples. The alloy was previously hot rolled at approximately 400°C to 75 mm thick plate and received in the commercial T7451 temper condition. Its chemical composition was determined by optical emission spectrometry. The T6I4 condition was obtained from the as-received material by means of a solution treatment (486°C / 4h) followed by two-step ageing (145°C / 30 min and 65°C / 24h).

The fracture toughness of the material in both T7451 and T6I4 conditions was determined using the Chevron notch methodology according to ASTM E1304-97(2020) standard. The fatigue crack growth tests were conducted under constant amplitude ($R = 0.1$ and 0.5) and variable amplitude loadings. In the former case, C(T) notched specimens in accordance with ASTM E647-15e1 standard were employed and the crack length was measured by the compliance method. In the latter case, the Mini FALSTAFF spectrum loading of dog-bone test specimens was adopted and the crack length was measured by quantitative fractography according to the method developed by DSTG (Australia). The results showed an expressive increase of the materials' KQ_{VM} values for the T6I4 condition, as well as a significant decrease on the crack growth rate, especially during the early stages of fatigue at lower constant amplitude ratio, possibly due to a more pronounced crack closure. The specimens treated to T6I4 condition and tested under spectrum loading also presented fatigue lives greater than twice the fatigue life presented by the T7451 material condition.

This work will be presented during the ICAF 2023 Conference and Symposium.

Metallic Structures

Post-Buckling Fatigue Crack Propagation on Curved Stiffened Panels (Ref. [14])

Summary:

In the project of aeronautical structures, the buckling phenomenon might occur in loads lower than the envelope limit ones. Under these conditions, the post-buckling behavior must be analyzed, where the load initially resisted by the buckled component is redistributed to adjacent elements and internal stiffeners. Therefore, inside the operational envelope, buckling might be frequent, resulting in cyclic loadings that may originate crack nucleation and propagation due to fatigue.

The objective of this work was to propose a calculation methodology to quantify the effects of stress fields resulting from the post buckling regime on the crack propagation in aeronautical stiffened panels subject to cyclic loading.

Along with the work, an original methodology is proposed and validated in order to obtain the geometric correction factor of structures under buckling, allowing to quantify the propagation rate of cracks under these conditions. In this context, a modification of the Virtual Crack Closure Technique (VCCT) was also proposed and validated, allowing to consider the out-of-plane bending effects in the geometric correction factor for cracks propagating predominantly in Mode I. The results obtained demonstrated the relevance in considering the post-buckling effects on the crack propagation rate for the proposed stiffened panels configurations, indicating potentially non-conservative results when linear elastic analyses are considered without including the stress redistribution, inherent to loadings in the post-buckling regime.

Highlights:

In order to perform the analysis of the stiffened curved panel proposed and to simplify its implementation for aircraft applications, an elliptic geometry simplification was proposed to represent the skin shell, as presented in Figure 21, where L is the shell length, a is the width of the shell measured in the ellipse's main axis, b is the height of the shell measured in the ellipse's secondary axis and c is the position of the stiffener measured in the ellipse's main axis. As boundary conditions, CE stands for clamped edge and SS stands for simply supported edge. Further, a crack was assumed to exist in the middle of the right clamped edge, as shown in detail in the right side of Figure 21.

Sixteen configurations were initially evaluated, encompassing 4 different stiffener geometries, whose dimensions are shown in Table 2, and located in 4 different positions. The selection was based on industry available stiffeners and compatible

plate dimensions with aircraft projects. The configurations were evaluated by stiffener position where the highest stress levels were highlighted.

These identified configurations were subject to a final comparison, where the least critical case is the configuration where the stiffener type 3 is placed at 60% of the main axis and the most critical configuration is where the stiffener type 1 is placed at 90% of the main axis. The former will be called from now on “Configuration 1” and the latter will be called “Configuration 2”

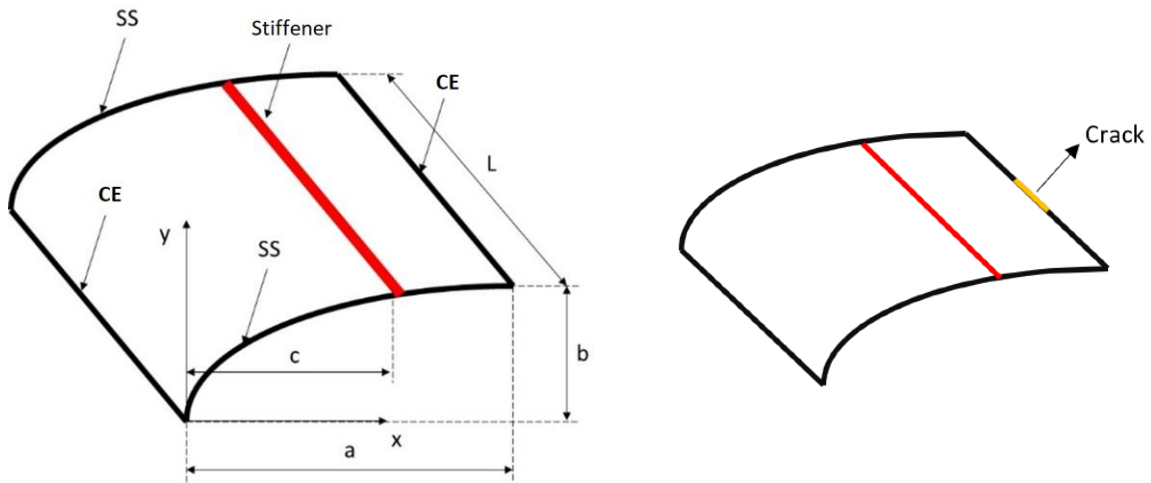


Figure 21 - Geometric properties and assumed crack location for the problem under analysis.

Table 2 - Stiffener types and dimensions.

| Stiffener Number | Model | A (mm) | B (mm) | t_A (mm) | t_B (mm) | R (mm) | I (mm ⁴) |
|------------------|---------------|--------|--------|------------|------------|--------|----------------------|
| 1 | AND10135-0401 | 12.70 | 12.70 | 1.02 | 1.02 | 1.52 | 1274.38 |
| 2 | AND10135-1001 | 25.40 | 17.53 | 1.27 | 1.27 | 1.91 | 10996.74 |
| 3 | AND10135-1004 | 25.40 | 22.35 | 2.03 | 2.03 | 2.97 | 19878.64 |
| 4 | TMS60-19794 | 28.58 | 20.65 | 2.39 | 2.39 | 2.97 | 28661.37 |

A numerical model was built by drawing the elliptical cross-section in the XY plane and then the curve was extruded in the positive z direction. The model was meshed using plate elements for the elliptical skin shell and beam elements representing stiffeners. These stiffeners were represented with an offset defined inside the property to properly represent their position. The connection between stiffener and plate was performed by the coincident nodes, where the stiffener was considered integral to the skin. The model was evaluated for different mesh sizes using the force versus displacement graphs in order to verify an equilibrium between convergence and computing efficiency. Loads were applied such as to simulate displacements driven by a wing box.

Based on typical parameters of aircraft projects, the geometry of the plate analyzed was defined by the properties listed in Table 3, which follows the schematic geometry proposed in Figure 21. The material selected for the shell is the Aluminum 7475-T7351 alloy, as it is commonly used in the aerospace industry for structures under compressive loadings.

Table 3 - Plate geometry.

| a (mm) | b (mm) | c/a | L (mm) | Plate thickness (mm) |
|--------|--------|---------|--------|----------------------|
| 340 | 160 | 0.6-0.9 | 340 | 1.5 |

First, a parametrical buckling analysis was performed. All 16 possible geometries were analyzed in the uncracked configuration and the results are shown in Figure 22.

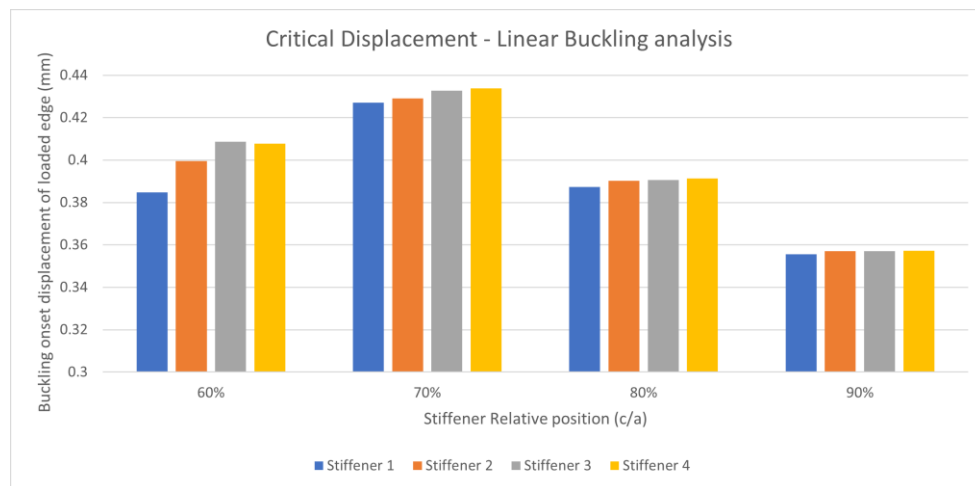


Figure 22 – Critical displacement – linear buckling comparison.

After performing the configuration selection process, from where Configurations 1 and 2 were obtained, three numerical analyses were performed, considering semi-crack (a) sizes of 0 mm, 60 mm, and 165 mm. One example of the force x displacement analysis for Configuration 1 and a semi-crack size $a = 60$ mm is presented in Figure 23.

The analyzed configurations were subject to a cyclic loading with R equal to zero, where the reference stress oscillates from zero to the highest stress obtained from the VCCT analyses. The highest stress was identified as 140 MPa for Configuration 2 under the prescribed displacement of 0.8 mm, then this value of applied stress was used for all the subsequent crack propagation analyses.

Crack growth analysis was performed assuming three conditions, considering (i) pre-buckling, (ii) intermediate buckling and (iii) post-buckling geometry correction factors. Each of these analyses led to considerable different results. As an example, the results for a post-buckling condition are presented in Figure 24.

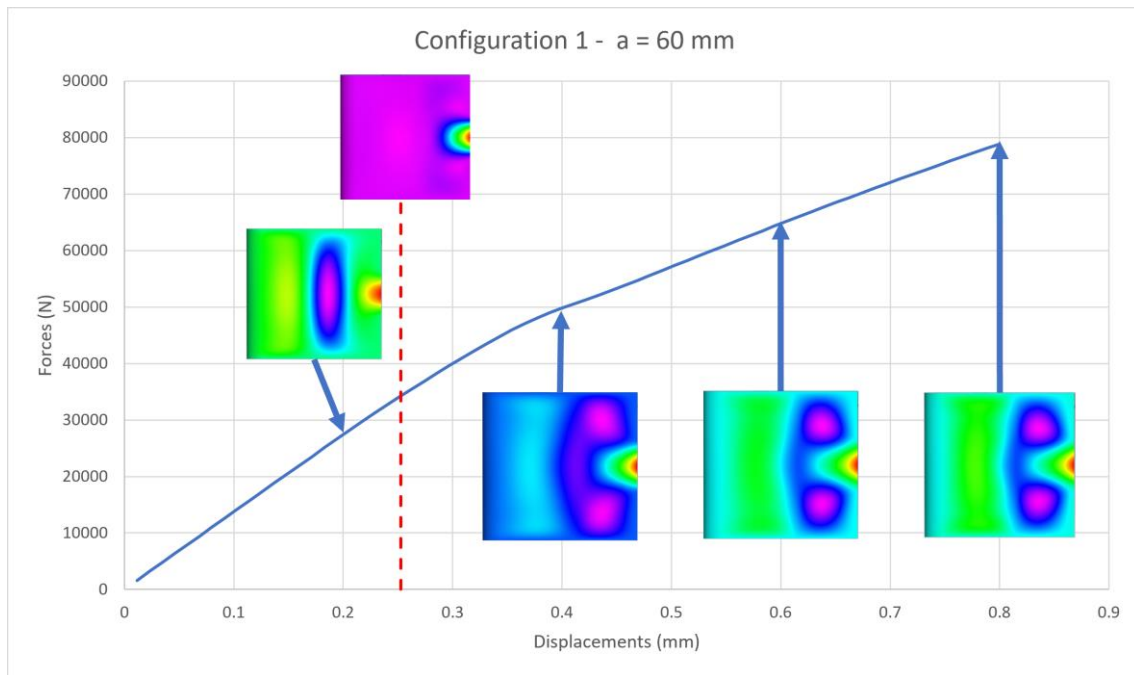


Figure 23 - Force x displacement - $a = 60$ mm - Configuration 1

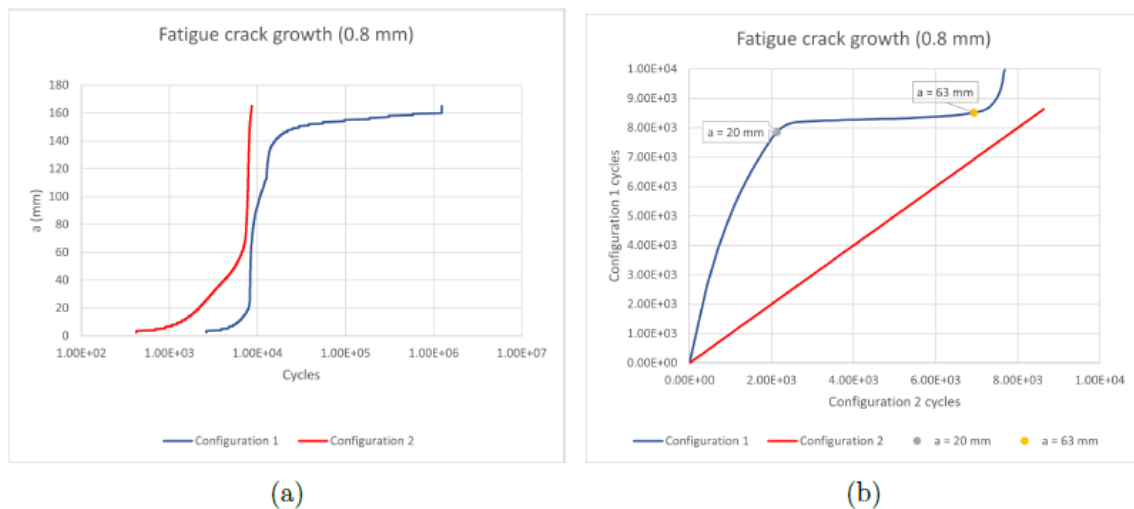


Figure 24 - Comparisons for the post-buckling geometric correction factors: (a) crack growth cycles, (b) crack growth rate.

Characterization Of MSD in emerging metallic structures in fuselage lap joints (Ref. [15])

Summary:

In partnership with Arconic and Embraer, the Federal Aviation Administration (FAA) is evaluating the behavior of multi-site damage (MSD) for emerging aluminum alloys in a generic fuselage lap joint configuration. This program is a

comparative study of the initiation and growth characteristics of MSD for two aerospace aluminum alloys, namely: 2524-T3 aluminum-copper alloy (baseline) and 2060-T8 aluminum-lithium alloy (new generation). This behavior is being studied by conducting fatigue testing on a common lap joint design at three different specimen sizes, namely: (1) single rivet column coupons, (2) wide flat panel specimens, and (3) curved sub-scale panel specimens. Data from this study will be used to assess the relevance of existing regulations and to inform whether additional safety standards and regulatory guidance should be developed to provide improved safety beyond that afforded by the existing airworthiness standards. Additionally, results will be used to support potential improved weight and structural safety performance expectations of the EMST and to evaluate the effect of specimen scale on fatigue performance.

As part of this program a subset of the 2524-T3 wide flat panels and curved sub-scaled panels were manufactured with an initial MSD scenario. The purpose of the MSD scenario was to establish a common starting point for the crack growth and residual strength portions of the tests to facilitate better post-test comparisons. Additionally, based on finite element modelling it was anticipated that the wide flat panels would experience higher secondary bending of the joint compared to the curved sub-scaled panels. So, a subset of the MSD wide flat panels was also tested in a constrained manner to bring it closer to the predicted curved panel behavior. This paper will provide a brief overview of this program with focus on the test and analysis of the wide flat and curved sub-scaled panel with the initial MSD scenario.

In this report, a summary of the tests performed in Embraer facilities, in Brazil, will be included. This work will be presented during the ICAF 2023 Conference and Symposium.

Highlights:

The loading mechanism for wide flat and curved sub-scale panels is different. The flat panels are uniaxially loaded while the curved sub-scale panels are mounted in a test frame which constrains all sides and is internally pressurized (leading to membrane hoop and longitudinal loads). As the finite element model results show in Figure 25, this difference has a significant effect on the bending for the two different specimens. The wide flat panel is expected to have considerably more bending compared to the curved sub-scale panel.

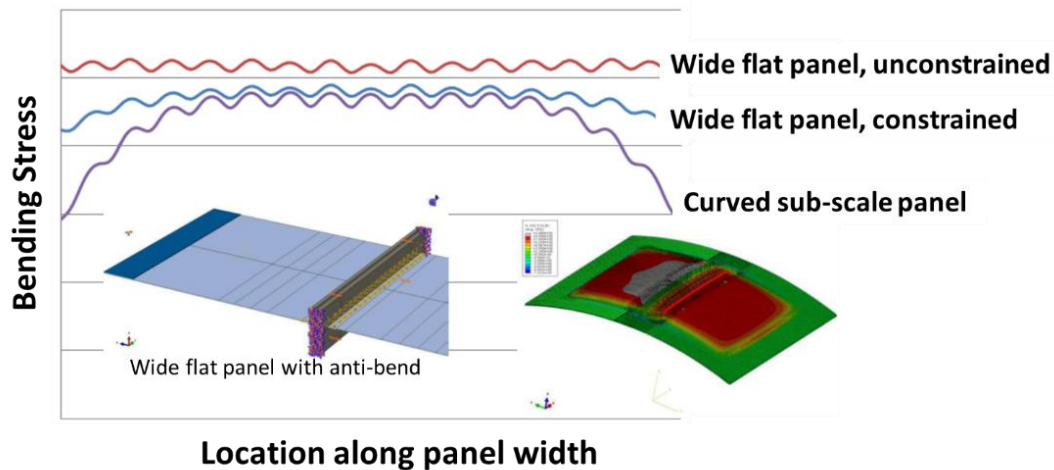


Figure 25 - Bending stress (obtained from FEM analysis) for a flat panel (unconstrained and constrained) and for a curved panel.

Embraer performed testing for the curved sub-scale panels. This was done on a customized fixture made to test curved panels under internal pressurization. The fixture, shown below in Figure 26, is designed to test panels with a radius of 1143 mm. The panels are fixed on all four sides to the fixture and internally pressurized by air. The tests were run at a rate of approximately 0.5 hertz. A total of five panels were tested.

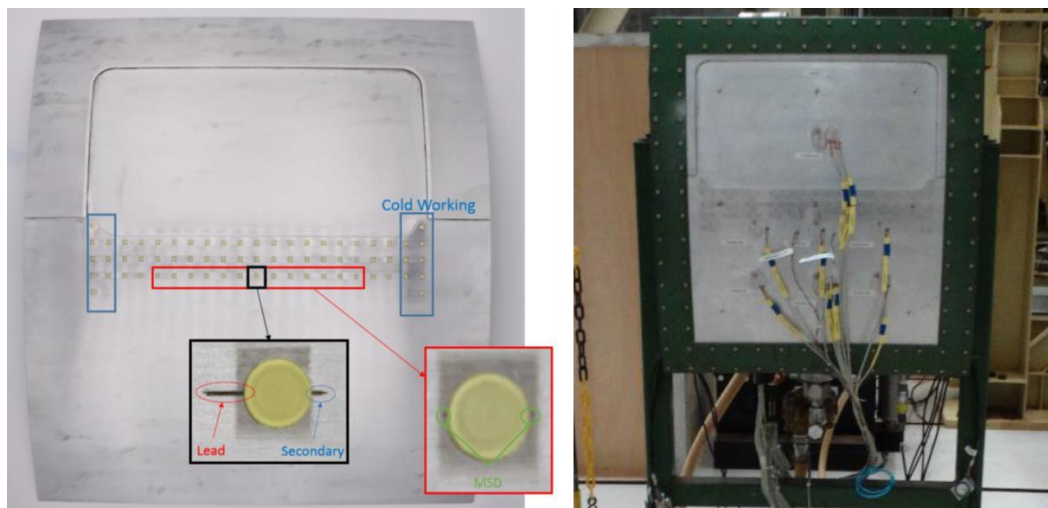


Figure 26 - Curved Sub-scale Panel Test Setup.

Among other results, the crack growth for the lead crack and MSD cracks was compared between the flat and curved panels. The experimental results for this test matrix did not clearly show the effect of curvature in the crack growth, as predicted by analytical models. Effects that may influence these results such as the secondary bending, stress biaxiality, and boundary conditions are being investigated and the work is still ongoing.

Crack growth analysis of fiber metal laminates stiffened panels (Ref. [16])

Summary:

There is a large potential for increasing use of fiber metal laminated stiffened panels in aerospace applications, due to their low crack propagation rates and excellent residual strength behavior. In order to compare the traditional built-up aluminum constructed stiffened panels and fiber metal laminates materials under the context of damage tolerance, two stiffened panels were designed, tested and compared against numerical (finite element) analysis results: (1) aluminum skin with riveted stringers and (2) fiber metal laminate skin with bonded stringers. The two panels exhibited significantly different results, with the fiber metal laminate stiffened panel having the best response in both crack propagation and residual stress. With the objective of obtaining an accurate analysis tool for these two panels, filling a gap of available commercial software, detailed Finite Element Models are built aiming the use of Virtual Crack Closure Technique to obtain Stress Intensity Factors, taking into account the delamination phenomenon during crack propagation on fiber metal laminates materials. Numerical results show that the proposed technique is able to reach good correlation and it is observed that the chosen delamination shape largely dictates crack growth behavior on the fiber metal laminates stiffened panel.

Highlights:

To verify the numerical approach to be applied in this work, a detailed experimental analysis was carried-out to provide reliable experimental data for comparison. Two stiffened panels were built and tested to further investigate crack growth behavior: (1) monolithic aluminum skin with riveted stringers (code-named REB) and (2) FML skin (Glare®) with glued stringers (code-named FML).

The specimens have the dimensions shown in Figure 27, for both stiffened panels. Each plate has 5 stringers attached, with the central stringer being cut to simulate complete failure. The skin of the stiffened panel has a 6mm circular notch and a 12 mm cut to simulate a small initial crack. Anti-bending bars were positioned next to the crack growth region, in contact with stringers and skin, to simulate pure Mode I loading on the crack growth zone by avoiding out of plane bending caused by the stiffened panel's inherent asymmetry. The materials used in each stiffened panel are shown in Table 4, along with the stringer connection methodology. The Glare® layup used in the FML plate is shown in Table 5, where 0° corresponds to the longitudinal direction of the stiffened panel.

The experimental tests were conducted using a servo-hydraulic testing machine with 2Hz cyclic load application frequency and $R = 0.1$ (minimum over maximum load ratio), applying a P_{max} load to the riveted stringer panels and $1.2 P_{max}$ to the FML panel to induce a gross stress on the aluminum sheet compatible with a

common stress value found in fuselage skins under service and an initial stress intensity factor of $500 \text{ MPa}\sqrt{\text{mm}}$ for the riveted panels, and $600 \text{ MPa}\sqrt{\text{mm}}$ for the FML panel. Applied loads, displacements, crack length and strain distribution along the specimens were measured during the crack growth test and residual strength test by load cells, displacement sensors, a couple of crack gages and rosettes glued in the adjacent bays from the cracks site, for far field strain reading. Crack sizes were visually monitored as well using a couple of CCD cameras, one for each crack front. A residual strength test followed each crack propagation test. The experimental setups are shown in Figure 28. The crack propagation results are shown in Figure 29, for each panel and crack front. The experimental results from the residual strength tests are shown in Figure 30, where the applied load, and crack growth are measured until final fracture.

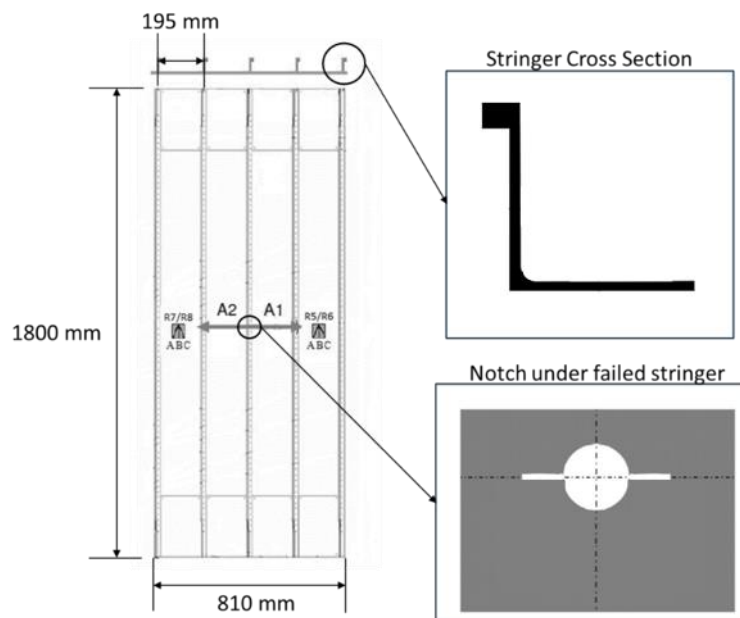


Figure 27 - 4 Plate and stringer geometry – with A1 and A2 as the two crack front directions.

Table 4 - Stiffened panel materials.

| Panel | Plate Material and Thickness | Stringer Interface | Stringer material |
|---------|------------------------------|--------------------------|-------------------|
| Riveted | Al 20XX, 1.25mm | Al 21XX Rivets, 3.969 mm | Al 70XX |
| Glare | Glare®2A – 2/1 – 0.4, 1.06mm | Cytec Adhesive | Al 70XX |

Table 5 - Glare® skin layup.

| Ply | Material and Thickness | Orientation |
|-----|------------------------|-------------|
| 1 | Al 20XX, 0.4 mm | - |
| 2 | Glass Fiber tape | 0° |
| 3 | Glass Fiber tape | 0° |
| 4 | Al 20XX, 0.4 mm | - |



Figure 28 - Experimental test setup for fatigue tests (left) and residual strength tests (right).

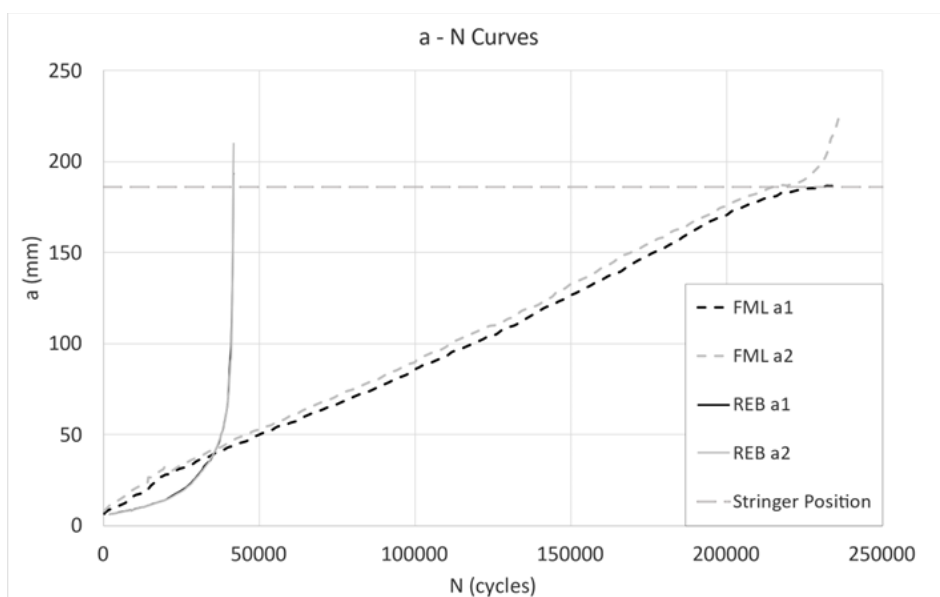


Figure 29 - Crack propagation result for each stiffened panel and crack front.

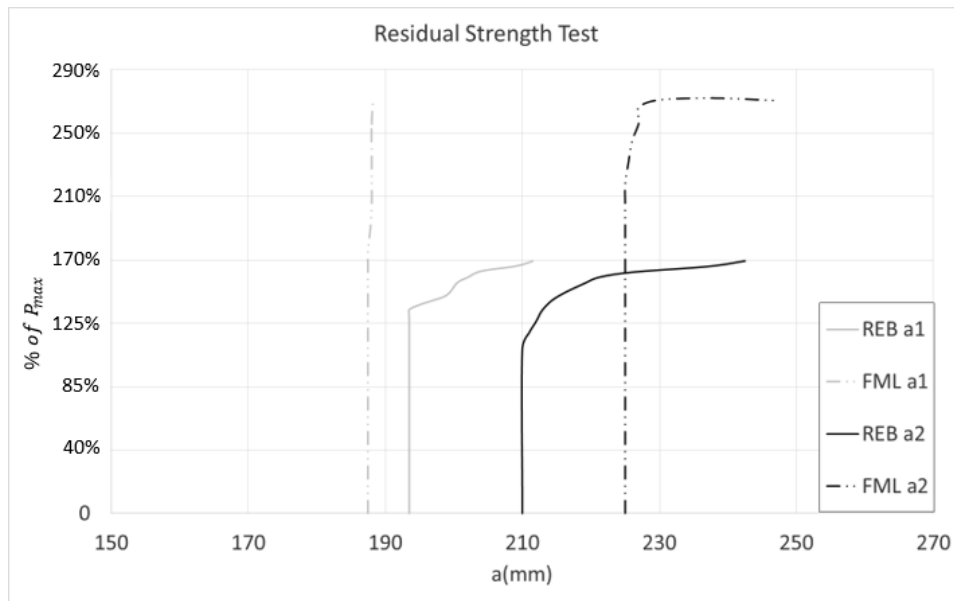


Figure 30 - Residual strength test results.

Finite element models for both stiffened panels were built using a common baseline model, with identical geometry to the tested panels. In general, the skins were built using linear plate elements (CQUAD4), 3mm size on refinement region (where crack propagation occurs) and 9 mm on coarse region (outside the crack propagation region). Only half of each stiffened panel was modelled, using the crack propagation plane as symmetry plane (XZ plane), with constraints on Y translation, X and Z rotations. Loads were applied through a rigid element (RBE2), imposing the same constraints as observed in tests. To simulate the anti-bending setup applied during experimental tests, linear gap elements were created on the same regions as the bars were positioned in tests, thus avoiding out of plane movement. A schematic of the model is shown in Figure 31.

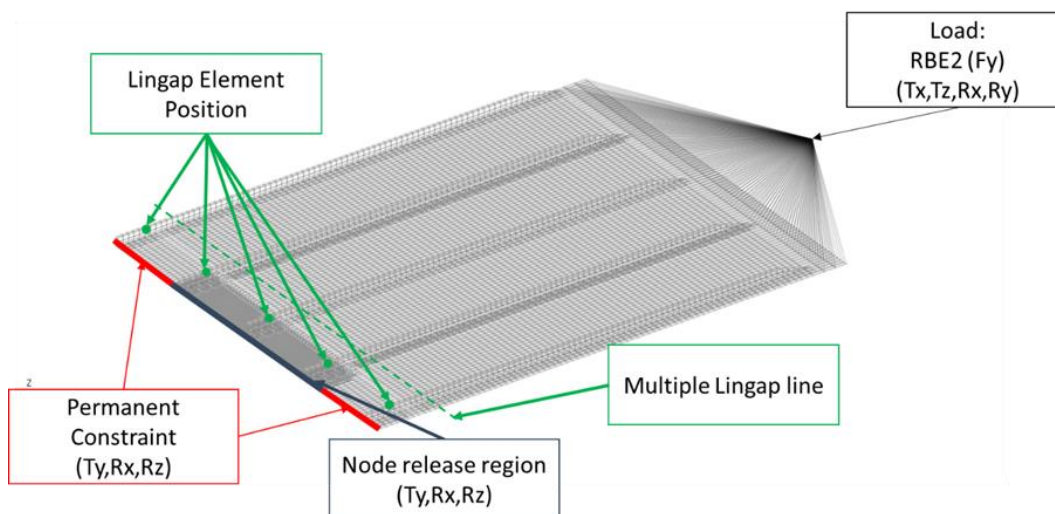


Figure 31 - FEM model - schematic.

To simulate the delamination phenomenon, a straightforward method was proposed where a linear correlation between the crack size and the delamination area is used, considering a predetermined proportion, assuming a delamination shape through crack length. The crack was grown in both aluminum layers symmetrically on both flanks and following the node releases occurring on the crack front, the MPC interface between layers was also undone as the cracks propagate, simulating the adhesive failure, illustrated in Figure 32. Through this image, a b/a (delamination length at the notch root divided by crack size) relation of 0.28 was visually determined trying to compensate the irregularities on the test shape (due to stringer induced torsion), being used for analysis. Four delamination shapes were studied: triangular, elliptical, cosinoidal and parabolic. The Glare® panels were then analyzed, using the different delamination shapes for crack propagation. Two analyses were performed: the first to obtain delamination shape effects in SIF behavior, and the second to assess the b/a proportion (delamination length on notch versus crack length) for each delamination shape. Finally, the $a-N$ curve using the SIF values obtained from this analysis was obtained and is illustrated in Figure 15.

More details about this work will be presented by the authors during the ICAF 2023 Conference and Symposium.

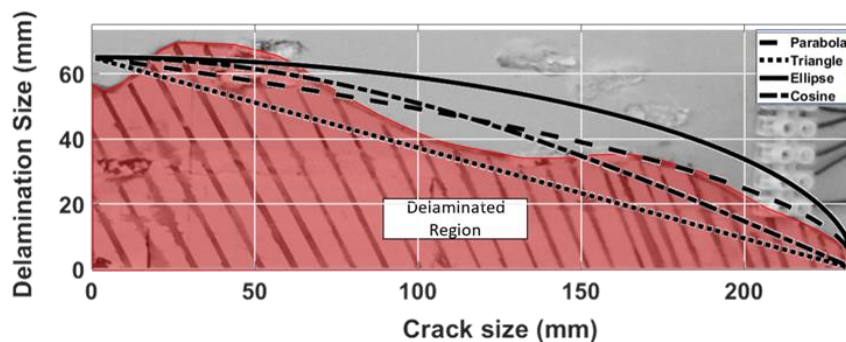


Figure 32 - Numerical delamination shapes tested and compared against the experimental delamination shape, measured using NDT testing.

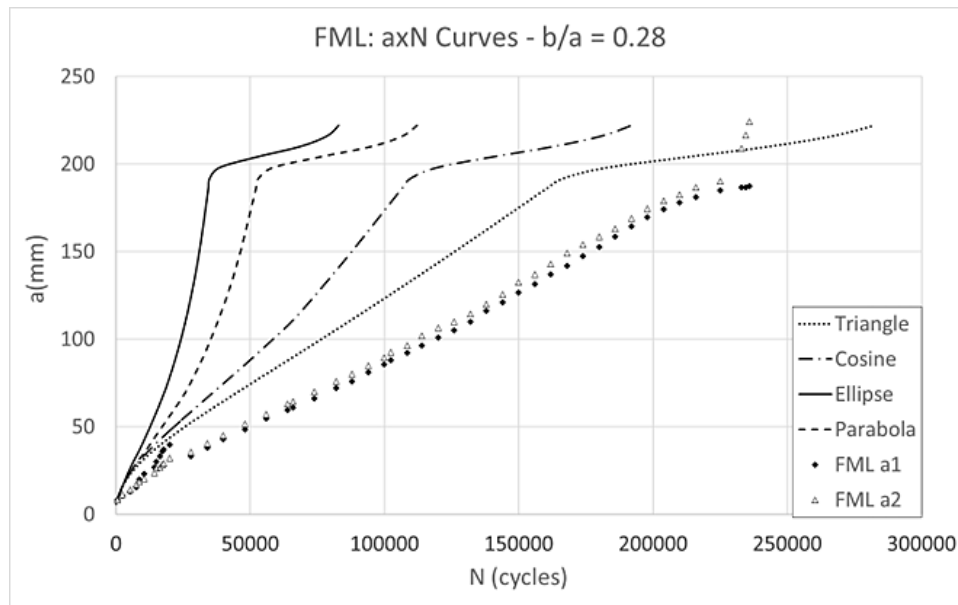


Figure 33 - a-N curves obtained by delamination shape.

Comparative study of adhesive fatigue in aeronautical bonded joints: A numerical approach in the frequency domain (Ref. [17])

Summary and Highlights:

This work investigates a procedure for fatigue life prediction of an aeronautical bonded joint under random loads, in particular, the cohesive failure of the adhesive layer in a skin-to-stiffener bonded joint.

The use of two different adhesives is investigated, and Dirlik's method is employed to predict the stress response in the adhesive layer, from which the fatigue life is obtained. The effect of damping is also investigated, and it is shown that increases in damping result in higher fatigue life estimations.

The work is analytical, and the analyses are based on the structure shown below in Figure 34.

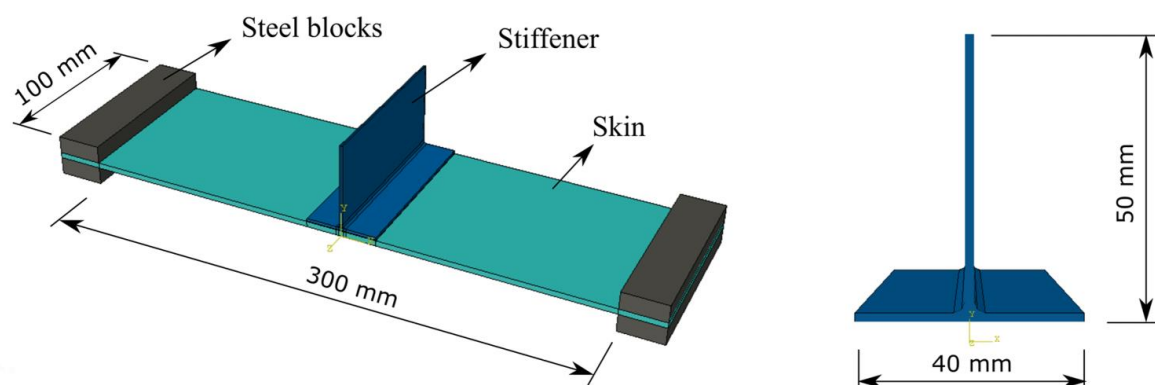


Figure 34 - Model used in the simulation (left) and detail of the stiffener (right).

Component and full-scale fatigue tests overview

Currently there are two full-scale fatigue tests being performed. The KC-390 multi-mission aircraft test specimen, presented in the previous ICAF report, and the Embraer 195 E2 (second generation) aircraft test specimen.

Parallel to the Embraer 195 E2 full-scale fatigue test, this development test is being performed for verification of the Embraer 190 E2 wing fatigue behavior. This is because while the fuselage of the Embraer 190 E2 and Embraer 195 E2 have very similar constructions, their wings present some differences. Figure 35 shows the overview of this test, that is currently being performed.

The empennage fatigue test for these aircraft has completed three lifetimes without relevant findings.

The landing gear tests for Embraer E2 aircraft as well as the KC-390 are currently being performed in Embraer facilities, in São José dos Campos, Brazil.

Additionally, the horizontal stabilizer of Embraer 175-E2 aircraft, that is made of composite materials, finished full-scale static and fatigue tests in Brazil, according to related certifications requirements.

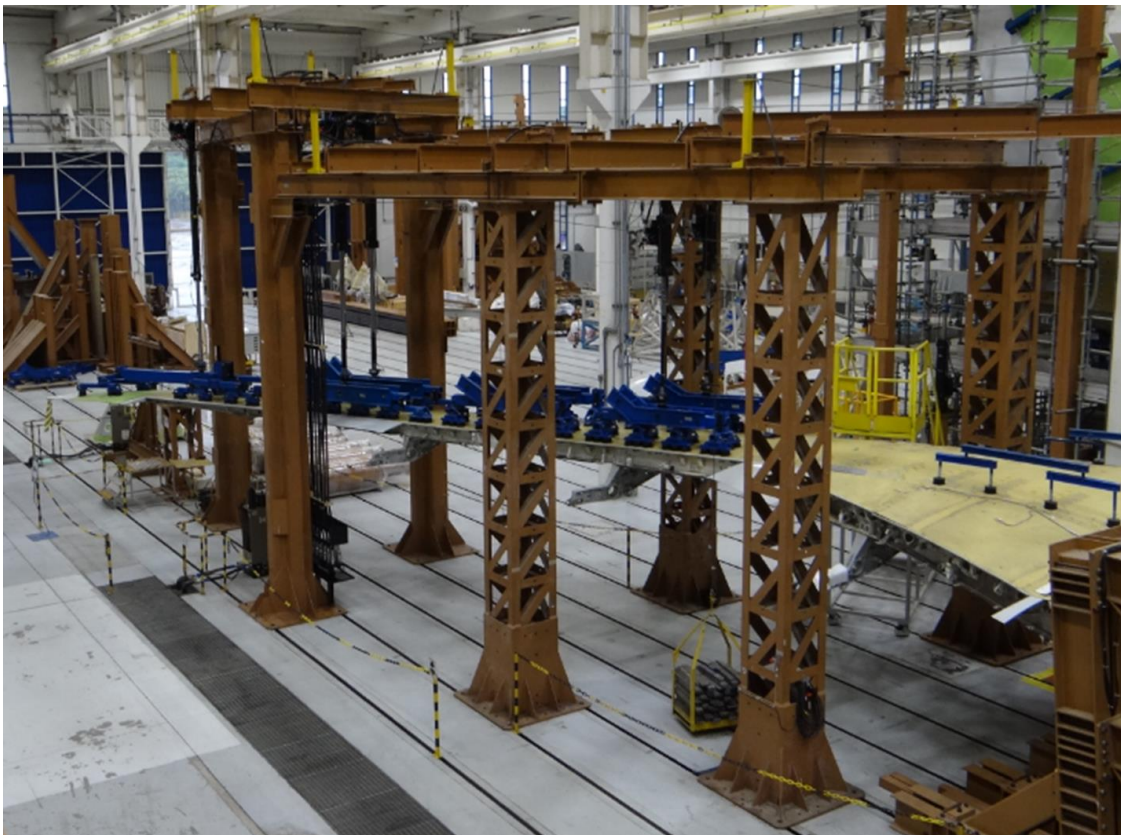


Figure 35 - Embraer 190 E2 (second generation) wing full-scale fatigue test overview.

Structural Health Monitoring

Damage detection and fatigue life estimation under random loads: A new structural health monitoring methodology in the frequency domain (Ref. [18])

Summary:

This work presents a methodology for structural health monitoring of fatigue cracks under stationary random loads. The methodology is composed of two parts: an empirical correlation to monitor the evolution of damage indices and a numerical scheme for fatigue life estimation. The damage indices are based on the variation of the vibrational response of the structure due to crack propagation.

Two damage metrics are studied, and the methodology is verified for a cantilever beam subjected to random base excitation. The case study validates the effectiveness of the methodology and shows that both metrics have the potential for damage detection. For the numerical estimation of the fatigue life, the proposed framework uses the probability density function of the stress, which is obtained from frequency-domain methods, and an equivalent stress approach based on the Walker's equation for fatigue crack growth. Excellent agreement is found between the predicted fatigue life and the experimental values.

Highlights:

The objective of this research is to integrate a methodology based on VBM for damage detection and fatigue life estimation of structures under spectrum loads. Two different DIs are used for damage quantification, and an empirical correlation is developed to relate the DI values to the fatigue life of the structure. Besides the empirical correlation, a numerical framework is presented for the estimation of fatigue crack growth using a frequency domain approach and an equivalent stress concept. Figure 36 shows an overview of the methodology used in this work.

To evaluate the proposed methodology, a case study is examined, using an aluminum sheet in Al7075-T6. The geometry is a cantilever beam with 1.27-mm thickness, while the other dimensions are shown in Figure 37. Two pre-cracks are accurately machined in the specimen through an electrical discharge machining (EDM) process. The small radius (approximately 0.2 mm) of the machined pre-cracks makes sure that the crack propagates immediately from the beginning of the random vibration tests. Five specimens were tested.

Among other results, the stress response under vibration spectrum loads is obtained and damage indexes were also obtained as function of time. Figure 38 shows the progress for one of the DIs obtained. The crack propagation was also

measured for one specimen and compared with the model predictions. Because there are two edge cracks and two surfaces to be inspected (top and bottom), four crack measurements are made each time. During the whole test, only very small differences between the four crack sizes are observed, validating the previous assumption of symmetric propagation of the crack. In Figure 39, the mean value of the crack size (i.e., the sum of each crack size measured in each step divided by four) is plotted versus the time of load application. The figure also includes the numerical result obtained from the numerical integration of the Walker's equation, using the equivalent stress approach, that is explained in detail in the work.

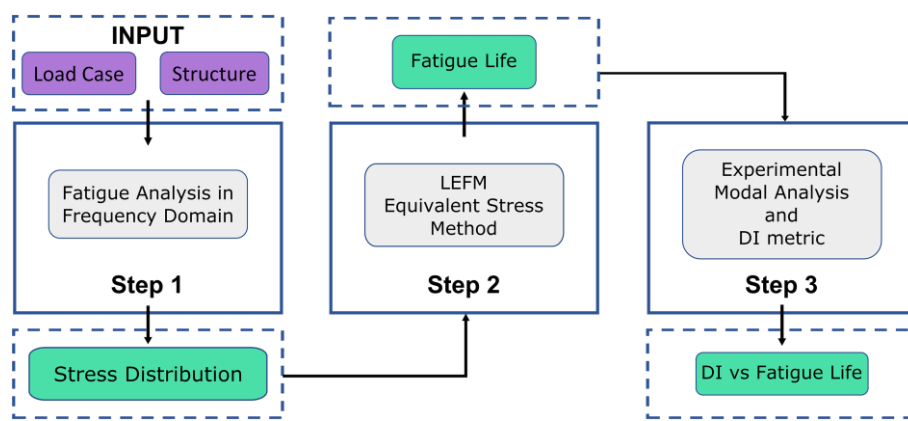


Figure 36 - Methodology used in this work.

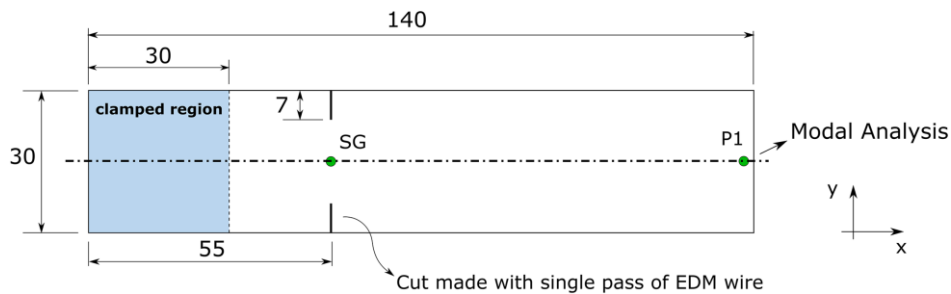


Figure 37 - Specimen geometry used in the random vibration tests.

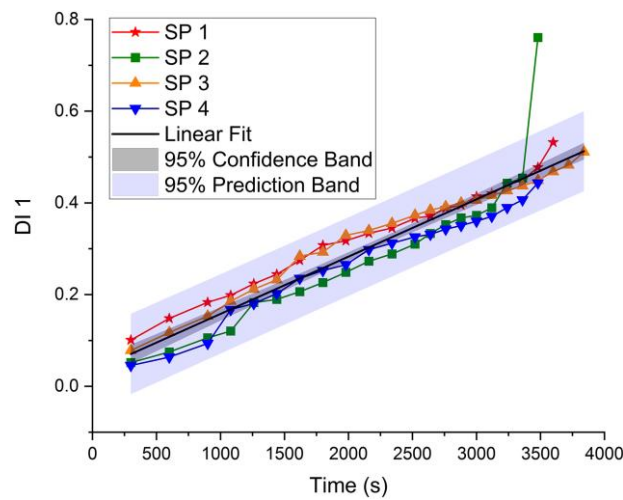


Figure 38 - Damage index "DI 1" versus time.

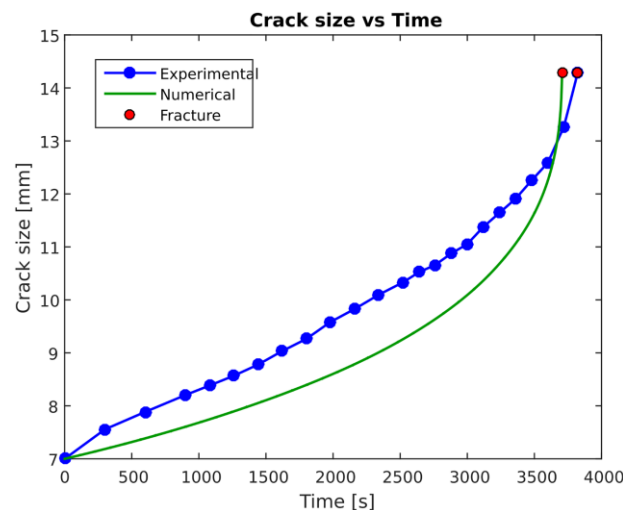


Figure 39 - Crack size versus time: experimental and numerical values.

Sensitivity and uncertainty analysis for structural health monitoring with crack propagation under random loads: A numerical framework in the frequency domain (Ref. [19])

Summary:

The quantification of uncertainties in a system and the ability to identify the most influential parameters for a given structural health monitoring (SHM) strategy constitutes an important step for an in-depth analysis of the problem. It is used in reliability assessment and for the definition of proper inspection intervals. In the previous work (Ref. [18]), the authors proposed a methodology for SHM and fatigue life estimations of structures under random loads.

This work expands over those concepts and presents a framework for sensitivity and uncertainty analysis for SHM of structures in the frequency domain. The

structure is a Euler–Bernoulli beam, which is modeled with the Ritz method. The conceptual simplicity of the Ritz model keeps the computational cost low. The results showed that the Walker parameter for the crack propagation law, C_0 ; the modal damping factor; and the input acceleration are important parameters affecting the variance of the remaining useful life.

Highlights:

The analysis starts with the derivation of the equations of motion of the cantilever beam using the Ritz approach. After this derivation, the stress PSD is calculated, spectral-based methods can be used to determine the probability density function (PDF) of the stress response. For wideband processes, approximate solutions such as the ones proposed by Dirlik and Benasciutti (Ref. [20]) could be employed. In the linear elastic fracture mechanics approach, the rate of crack propagation, da/dN , can be described by the Walker equation as a function of the SIF range.

The geometry under analysis is the same as previously presented in Figure 37, where the crack and ligament geometry and loading are shown schematically in Figure 40 below.

Finite element models were created with ABAQUS® for the intact beam and for the cracked beam, for the sake of comparing the reduction in natural frequencies caused by the presence of a symmetrical edge crack. Figure 41 shows the geometry and details of the mesh used to model an 8 mm long edge crack.

The last result highlighted in this report is the DI (damage index). The uncertainty in the proposed DI is evaluated for different crack lengths. The randomized inputs are considered according to the distributions shown in a table available in the paper. These inputs are . Figure 9 shows the DI distributions that are Young’s modulus, Poisson coefficient, density, length, width, thickness, tip mass, crack position, fracture toughness, modal damping, PSD amplitude and others. Figure 42 shows the DI distributions that are expected for crack sizes close to 8 mm.

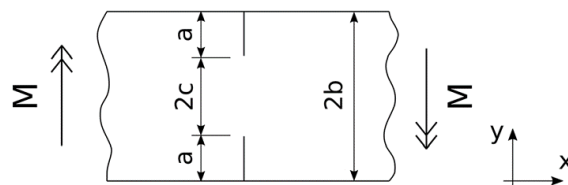


Figure 40 - Strip with edge cracks subjected to bending moment.

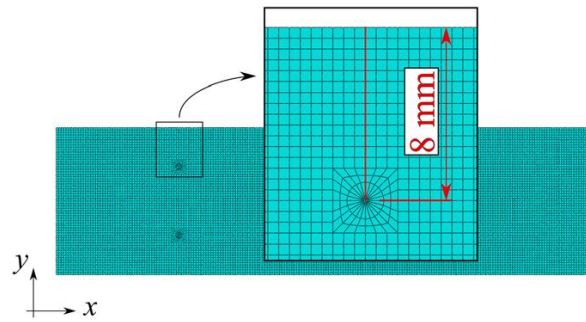


Figure 41 - Geometry and detail of the mesh around the crack used in the numerical analysis.

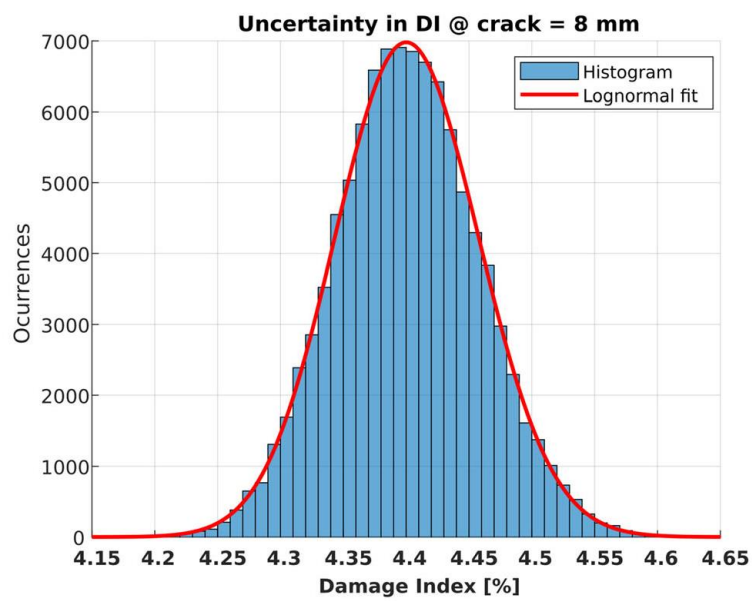


Figure 42 - Uncertainty in damage index values for a crack size close to 8 mm.

4. COMPOSITE MATERIALS AND STRUCTURES

Composite Materials

Static and fatigue resistance evaluation in fiber/epoxy composites under compressive loading and with different porosity levels (Ref. [21])

New jig adapted for compression fatigue tests on composite materials (Ref. [22])

Summary:

Composite materials are already widely used in the aerospace industry due to their low-density characteristic combined with high mechanical strength, under both static and fatigue conditions. Aeronautical and aerospace structures undergo, during their operation in service, mechanical stresses of tension, compression, bending and shear. In the case of structural composites, the compressive stresses are significantly dependent on the matrix. Furthermore, due to the anisotropic characteristic, inherent to composites, the damage accumulation mechanism in fatigue processes is more complex, compared to isotropic materials.

There are several methods for experimental determination of static compressive strength in composites, among them the CLC (Combined Loading Compression) method has been widely used by the scientific community because it combines two types of simultaneous load application, end-loading, and shear loading.

A new testing jig based on the CLC method was developed for the determination of static strengths and fatigue strength in laminated composites of carbon fiber/unidirectional epoxy and two types of bidirectional fabrics (8HS and Plain Weave) with different levels of porosity, as well as a cured epoxy resin that represents the matrix.

With this new testing device, first static compression tests were carried out at an application rate of 1 mm/min., later, fatigue tests were carried out with constant cyclic loading in the sinusoidal form, with a stress ratio $R=10$ and a frequency of 12 Hz up to the limit maximum of 120,000 cycles and lastly, residual strength tests were performed on samples that did not fail after 120,000 fatigue cycles. In static tests, the unidirectional composite with ~2% pore volume, for example, had an average mechanical strength in compression of 802 MPa and an average modulus of elasticity of 95 GPa. These values are ~40% higher, compared to the unidirectional composite with ~7% porosity. The fatigue strengths for these same composites were 596 MPa and 317 MPa, a difference of ~30% in relation to their respective static strengths, and the residual compressive strength and residual modulus of elasticity between these same two composites were 760 MPa, 75 GPa and 393 MPa and 46 GPa, respectively.

Highlights:

Some extracts from the second reference from the above are being added to this report. a newly adapted jig to perform quasi-static and fatigue compression tests based on the CLC, ASTM D6641 standard. This new jig is proposed to enable the performance of both static and fatigue tests accommodating various types of composite materials, different test standards, and coupons sizes. In order to validate the new testing jig, quasi-static and fatigue tests were performed in a composite with bidirectional carbon-fiber fabric type 8HS (Hardness Satin) with epoxy resin matrix (the number 8 on 8HS means that during the production process, the warp yarn goes over seven before going under one fill yarn). The static and fatigue compressive stresses obtained for the 8HS composite were 643.2 MPa and 436.6 MPa respectively. Figure 43(a) shows a schematic perspective drawing, of the compression jig and Figure 43(b) shows a detail of a coupon assembled on the jig. Figure 44(a) and Figure 44(b) show four coupons tested in fatigue and in detail the failure mode obtained for all samples tested, respectively.

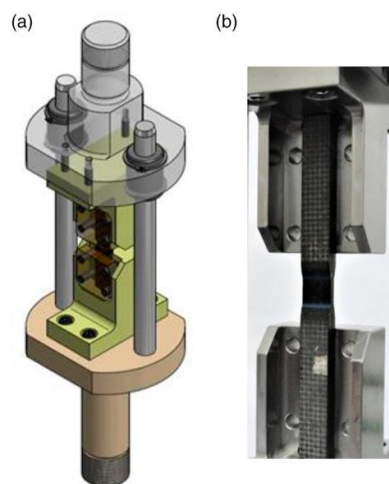


Figure 43 - (a) Schematic perspective drawing of the new jig and (b) a detail of a coupon assembled on the jig.



Figure 44 - (a) Coupons after the fatigue tests and (b) detail of the failure mode obtained in a sample coupon.

Mechanical characterization and fractographic study of the carbon/PEI composite under static and fatigue loading (Ref [23])

Summary:

The fatigue life of carbon fiber reinforced thermoplastic matrix composites is of great interest for many engineering applications. This work evaluated the influence of poly(etherimide) (PEI) on the fatigue life of laminated thermoplastic composites reinforced with carbon fibers. The mechanical characterization of the carbon/PEI composites was performed by static loading (tensile test) and cyclic fatigue. Tensile strength obtained was used to calculate 5 stress levels for cyclic fatigue testing with $R=0.1$ and 12 Hz for 85, 80, 70, 60, and 55%, this being last stress level found as the infinite life. These stress levels allowed plotting a well-described SN curve. Seeking to understand the fracture behavior of carbon/PEI composites, a fractographic study by scanning electron microscopy (SEM) was performed. SEM micrographs confirm the good quality of carbon/PEI laminate with good adhesion between fibers and matrix and also confirmed the nature of fatigue life showing in-plane fracture for high loads and explosive fracture for lower loads.

Highlights:

Tensile tests and tensile cyclic (fatigue) tests were performed. After the specimens failed, a detailed fractographic analysis was also performed to evaluate the morphology of the fractured faces.

Figure 45 shows the fractured specimen and fractured surfaces. These specimens were later assessed by SEM, and the work brings additional conclusions obtained from the SEM analysis. Figure 46 shows the S-N curve for the carbon/PEI composite, where 5 stress levels were tested: 85, 80, 70, 60, and 55% from the mean tensile strength obtained in the static tests (504 MPa).

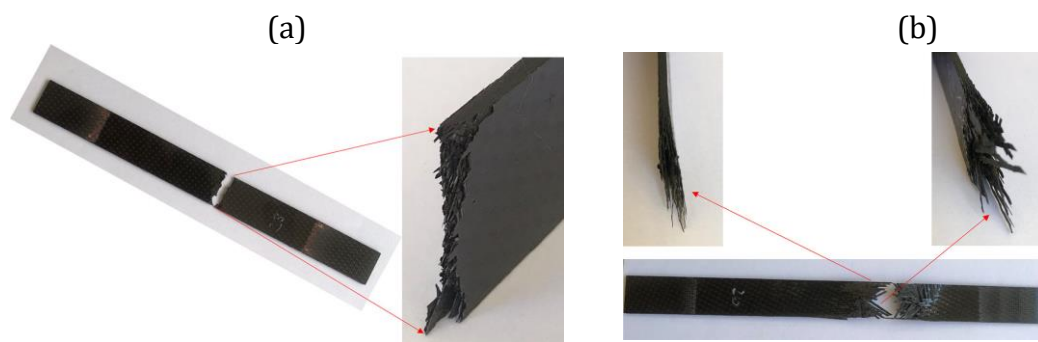


Figure 45 - Specimens fractured in the cycling test (a) with 85% of the tensile strength, (b) with 60% of the tensile strength and with the pronounced presence of delamination.

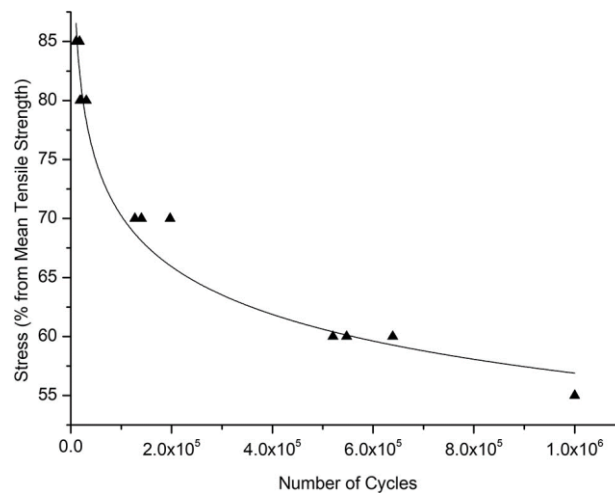


Figure 46 – S-N curve for carbon/PEI composite.

A finite element unified formulation for composite laminates in bending considering progressive damage (Ref. [24])

Summary:

This work proposes a novel approach to develop higher-order finite elements by taking progressive damage into account in the formulation. The approach is based on Carrera's unified formulation (CUF) while the damage model is based on continuum damage mechanics (CDM) principles, which is implemented as a UEL (User Element subroutine) written in FORTRAN and linked to Abaqus. The approach is assessed by simulating a plate under distributed and sinusoidal loads. Besides, a progressive damage analysis of a composite coupon under three-point bending is simulated, and the numerical predictions are compared against experimental results, showing good correlation. The main findings show that the implemented UEL is accurate and fast enough to predict progressive failure events and the in-plane damage mechanisms for composite laminates under bending loadings.

Fatigue in carbon-glass fiber/epoxy hybrid composite: the influence of hybrid interface in individual Mode I and II (Ref. [25])

Summary:

Developments in the aeronautical industry have led to the search for materials that meet the mechanical requirements for structural application, aimed at obtaining more efficient structures. The adoption of a carbon-glass fiber in hybrid composite could be a viable solution aiming to reduce the manufacturing costs and environmental impacts, because the carbon fibers used for aeronautical/aerospace applications are mainly coming from fossil fuels, which is currently a scarce

material. Recent applications have shown that varying the stacking order can alter the mechanical behavior of the hybrid laminate, as a response to the number of hybrid interfaces, i.e., carbon-glass fiber.

Aiming to understand the behavior in the hybrid interface to solve the design variability, this work purpose was to characterize the interlaminar damage progression in hybrid composites (continuous carbon/glass fiber) and to develop an analytical crack propagation model, considering the physical fracture mechanisms for two or more applied reinforcements. The energy balance principle method described the energy release of the hybrid composite with a greater energy available for fatigue delamination growth as a response of a synergy between reinforcements stiffness. The physics-based explanation for this enhancement is associated with the rougher fractured surface (tortuous crack propagation) due to a microscopic change in the crack direction at the carbon fiber/epoxy and glass fiber/epoxy interfaces. Additionally, Silane coupling agents influence the interaction at the carbon-glass/epoxy interface, enhancing the toughness behavior. The proposed model for the fatigue delamination growth rate of a hybrid composite was developed based on the fiber bridging zone phenomenon. A more realistic prediction model was obtained by considering the microfracture pattern measurement. The microscopic patterns formed during delamination growth reflect the growth rate at the macroscopic level under cyclic loading.

Lastly, the hybrid composite design using interspersed carbon-glass fiber (1×1) stacking sequence in a hybrid laminate is a reliable approach to increasing the delamination resistance, since the hybrid interface requires more energy for damage propagation, resulting in a longer life under fatigue loading.

Work Summary and Highlights:

Materials and processing: to evaluate the behavior of a carbon-glass/epoxy hybrid composite during Mode I delamination, fatigue tests were performed using three laminate composites: a carbon fiber composite (CFC – [0/90]_{4S}), glass fiber composite (GFC – [0/90]_{6S}) and hybrid composite (HC – [0/90]_{4S}). The hybrid laminate composite was produced with a hybrid interface (interleaved carbon and glass fiber). Crack propagation occurred at both reinforcement interfaces in the mid-plane of the laminate. The direction at the mid-plane interface reinforcement is 0C//0G, which presents parallel direction to the crack propagation for all laminates. The fabric located in the composite mid-plane was parallel aligned with the crack propagation direction. A fluoropolymer film was inserted at the laminate mid-plane to produce a pre-crack of 50 mm.

Mechanical delamination test: the fatigue test in Mode I and the specimen dimensions were those established in ASTM D6115 (Mode I) and ASTM D7905 (Mode II) in a universal servo-hydraulic machine, with a 2 kN load cell. Tests were

carried out with displacement-controlled conditions at a frequency of 5 Hz, with R-ratios of 0.2, 0.4 and 0.5 at constant amplitude. These tests were performed in duplicate for each material studied in 150 x 25 x 3.2 mm³. The minimal displacement (δ_{\min}) varied according to the R-ratio, keeping the maximal displacement (δ_{\max}) constant. The δ_{\max} used in the fatigue tests was determined based on the quasi-static test. The crack growth was associated with the minimal and maximal load values to analyze the strain energy release rate (SERR), using appropriate similitude parameters.

Results And Discussion: following the Paris model, the SERR (ΔG) range related to crack propagation (da/dN) is similar for CFC and GFC. The hybrid composite (HC), the energy range is significantly higher, associated with more intense interfacial resistance in the HC for both models. The synergy in of reinforcements (carbon-glass fiber) stiffness increasing the damage behavior dispersion during cyclic loading application. The effect of the R-ratio on $\Delta\sqrt{G}$ similitude parameter certifies the increase in the strain energy release rate required for the delamination in the hybrid composite. However, for more precise analysis and to better understanding of the microstructural fracture behavior on the hybrid interface in response to this increase in energy, the use of physical propagation approaches is needed.

The slope for the HC laminate was lower due to the greater amount of energy that needs to be overcome before damage occurs. This phenomenon may be associated with the delamination resistance of HC, which withstands a higher number of cycles when compared to non-hybrid laminates. The results also confirm that the hybrid composite increases the delamination resistance, with more damage features on the surface, meaning that a higher amount of energy is needed for delamination crack propagation.

The hybrid laminate exhibited regions with carbon and glass fiber fracture features along the fracture surface, which indicates a micro-change in the crack direction between the carbon/epoxy and glass/epoxy interfaces. The direction change was associated with the difference in stiffness and interfacial adhesion of the two reinforcements. When the crack directions differ for the two reinforcements (hybrid laminate), additional energy is required to overcome the heterogeneous path restriction. Figure 47 and Figure 48 show the da/dN vs. ΔG results obtained for R = 0.2, 0.4 and 0.5 and for CFC, GFC and HR.

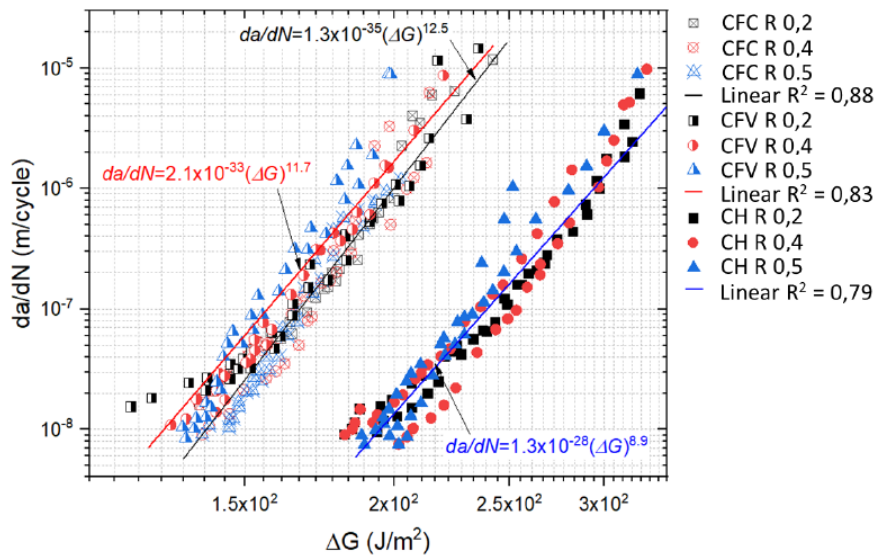


Figure 47 - Paris model results - Mode I (CVF = glass fiber composite, or GFC).

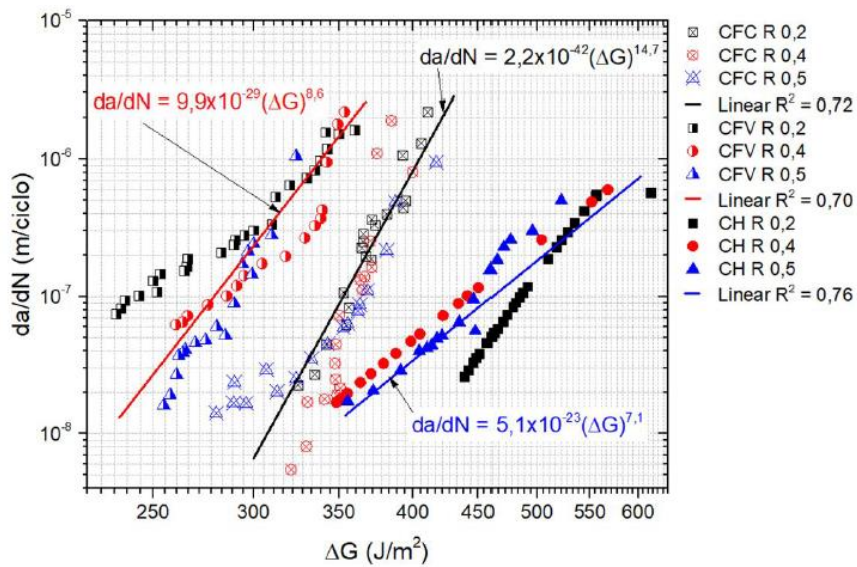


Figure 48 - Paris model results - Mode II (CVF = glass fiber composite, or GFC).

Failure analysis in secondary bonded T-stiffened composite panels subject to cyclic and quasi-static compression loading (Ref. [26])

Summary:

Adhesive bonding technologies are widely used for the assembly of stiffened panels manufactured in advanced composites for structural applications in aeronautics. However, stiffened panels are prone to the occurrence of defects or damage in the skin/stiffener junction, which will reduce the damage tolerance properties and affect structural integrity. The presence of unstable irregularities in the bonding region contributes to the decrease in the level of adhesion, limiting the resistance of the adhesive/laminate interface when subjected to mechanical loads. This article presents an experimental fracture analysis of flat panels with a longitudinal T-stiffener integrated into the skin by secondary bonding. The panels were produced in quasi-isotropic carbon/epoxy laminates with an artificial insert film replacing the adhesive film in the center of the bonding, to induce the initial damage.

The tests were performed under cyclic loading followed by static axial compression loading at room temperature up to collapse. The panel selected for visual and fractographic analysis reached buckling instability with 14% of the final load, in the time interval when the failure propagation induced slight reductions in stiffness.

The results obtained from this work showed the influence of the failure mechanisms combined with the formation of the failure modes and fractographic aspects that characterized the complexity of the fracture morphology provided by debonding of the skin/stiffener junction. The information revealed was relevant to the understanding of the failure process resulting from a critical defect on secondary bonding joints, applied in the integration of composite stiffened panels for aeronautics applications.

Highlights:

Figure 49 shows the experimental set-up applied for T-shaped single stiffened panel fatigue and compression tests. The post-fatigue residual strength test results are presented in Figure 50. This figure provides information regarding normalized load and strain readings along with the panel-loading time history. In the same plot different points numbered from (I)-(V) were included to help identification of initiation and development of the fracture process in the instrumented stiffened panel for the test and selected for the study.

The work also supplies results about ultrasonic scanning for different cycling, macroscopic observations, and the fracture morphologies in different regions along the skin and stiffeners.

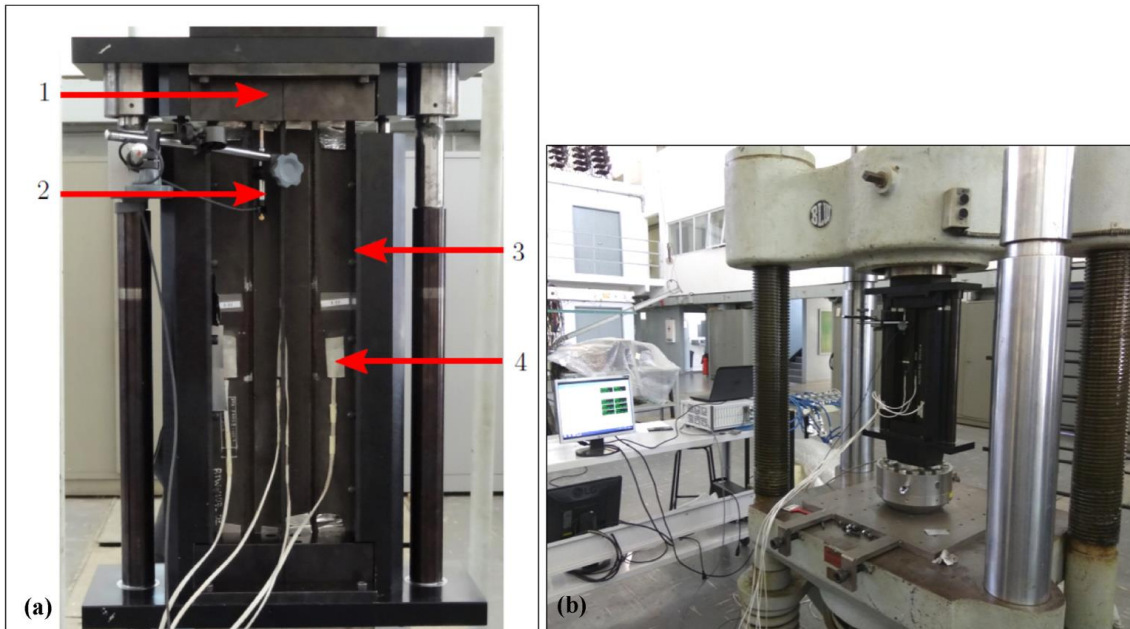


Figure 49 - Experimental test set-up: (a) Load frame and stiffened panel (1-clamped ends, 2- LVDT, 3- Anti-buckling edge supports, 4- Strain gauges), (b) servo-hydraulic load frame for quasi-static compression test.

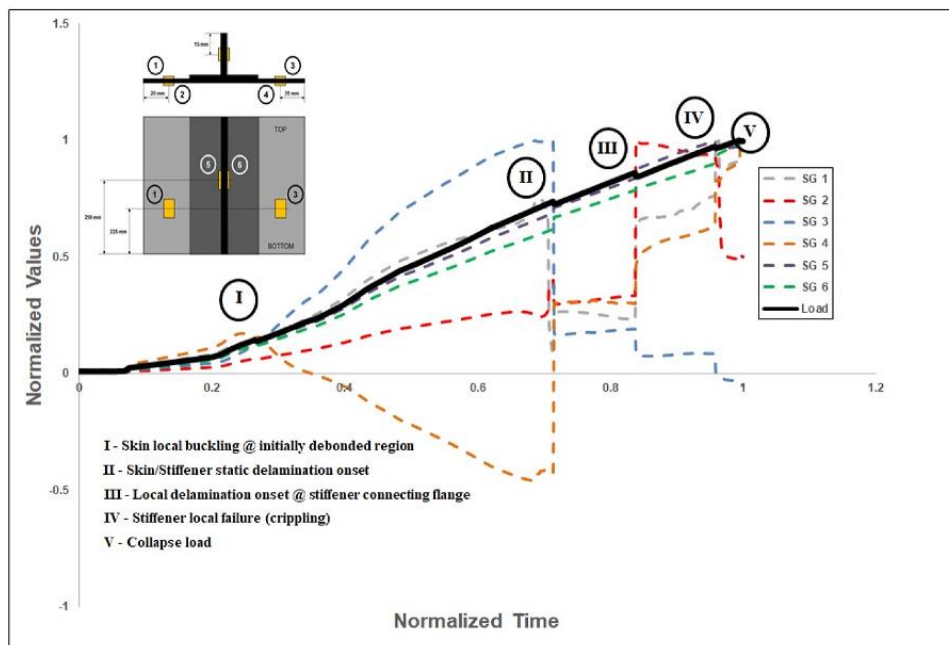


Figure 50 - Normalized results obtained from residual strength tests for a typical composite T-stiffened panel integrated by secondary bonding technology.

A progressive damage model for composite laminates based on non-linear continuum mechanics—Static and fatigue loadings (Ref. [27])

Summary:

Efficient yet reliable predictive modelling tools for damage tolerance analysis became an aerospace industry requirement as composite materials provided the potential for design performance. As damage can be separated into interlaminar and intralaminar, different approaches were developed over the years. For fracture analysis of intralaminar damage, a physical link to the Linear Elastic Fracture Mechanics (LEFM) provides a reliable framework for Continuum Damage Mechanics (CDM) models. These models, however, may exhibit pathological problems related to mesh dependence, objectivity, and convergence issues.

Differently from Cohesive Zone Modelling (CZM) for interlaminar damage, most intralaminar models are based on phenomenological approaches for fatigue analysis and life prediction. This work provides a description of some of the current intralaminar CDM models shortcomings, related to large strain analysis and finite element topology. A novel progressive damage model is proposed where damage variables are linked to the deformation gradient. Additionally, a fatigue damage behavior under the assumption of a Paris law for crack evolution is implemented in the proposed methodology. Both static and fatigue analysis were performed on a Compact Tension (CT) specimen geometry and compared to experimental data available in the scientific literature. Model predictions and experimental data were confronted allowing for conclusions to be drawn.

Highlights:

Figure 51 displays the finite element model, developed with ABACUS®, with three mesh configurations ahead of the notch tip. The numerical analysis was carried out with a displacement-controlled loading in the upper pin, while the lower one was fixed in translations.

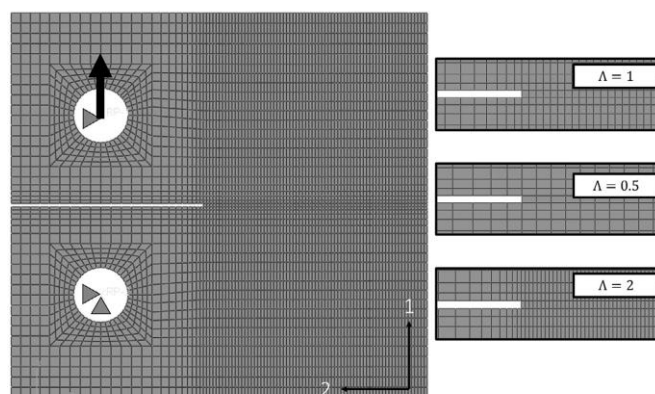


Figure 51 - Finite element meshes for compact tension coupon test specimen.

Figure 52 displays the reaction force as a function of the prescribed displacement on loading point. Both Figs. 8(a) and 8(b) display similar results for square elements ($\Lambda = 1$) and displayed a good correlation with experimental data reported in Souza et al. (Ref. [28]).

The CT specimen verification extends to cyclic loading, where crack propagation curves are different mesh sizes and compared with the experiment. In this case, a strong dependency on the refinement level is observed. As the mesh refinement increases, it was observed that a x N plots get closer to the prescribed crack evolution Paris law curve.

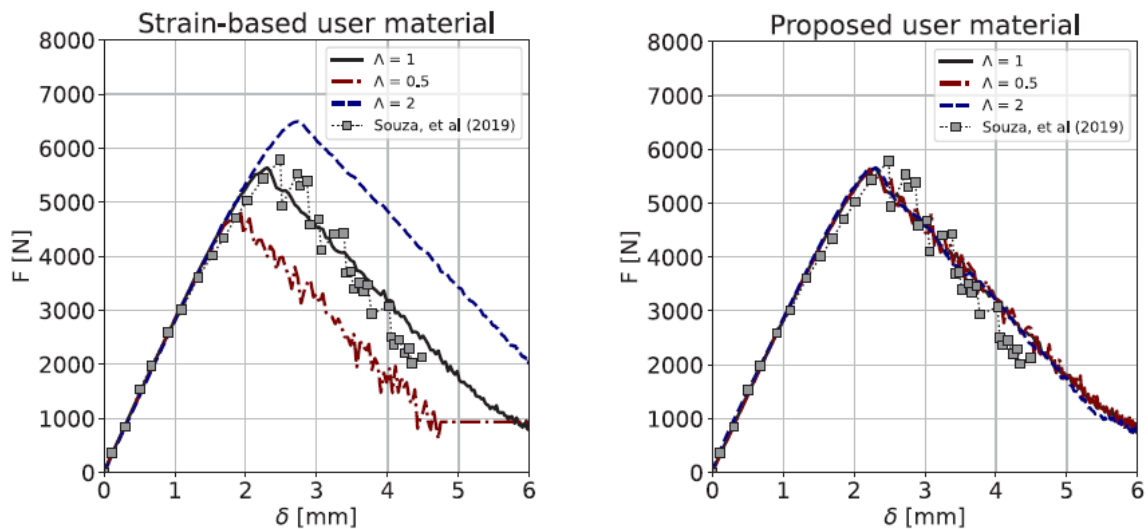


Figure 52 - Coupon level results for different progressive damage formulations and aspect ratios. (left: strain based variable formulation, right: proposed damage variable formulation).

Effects of mean load on interlaminar fracture behavior of carbon-epoxy prepreg fabric laminates under Mode I fatigue loading (Ref. [29])

Summary:

In this work, Mode I delamination fatigue crack growth behavior was investigated in a carbon-epoxy prepreg fabric laminate by evaluating the mean load effects. The fatigue crack growth rate was determined as a function of the maximum Mode I strain energy release rate considering an exponential fitting function according to the Compliance Based Beam Method (CBBM). Classical data reduction techniques were combined with the proposed method, indicating less scatter on results, and satisfying basic assumptions of smoothness and continuity for the fatigue crack growth process. The delamination growth rate curve proved to be strongly affected by the applied mean load as the fatigue onset delamination. The number of cycles to onset is higher for lower load levels and, considering the stable propagation region, a higher delamination growth rate was reported for higher

load levels. The fractographic analysis has confirmed the effects of cyclic loading and the mean load levels on fracture surfaces. For a higher mean load, failure mechanisms expose static aspects and substantial presence of microcracks at fiber imprints, while, under lower mean load were noticed significant wear and plasticity and featureless fiber tracks.

Highlights:

First, the CBBM is briefly described, helped by a workflow. Then, the methods and experimental procedures for Mode I delamination growth rate (including the test set-up, specimen characteristics and fractographic analysis) are explained.

From the various results obtained, Figure 53 shows the da/dN vs. G_I curves for the various load levels tested (for example, CDB_15.40_01 was tested for a mean load level $P_m = 15.40N$).

Results exposed in this work demonstrate that the fatigue crack growth was heavily influenced by the applied cyclic load. The crack grows faster as the load level increases, and delamination growth rate curves for higher load ranges are steeper.

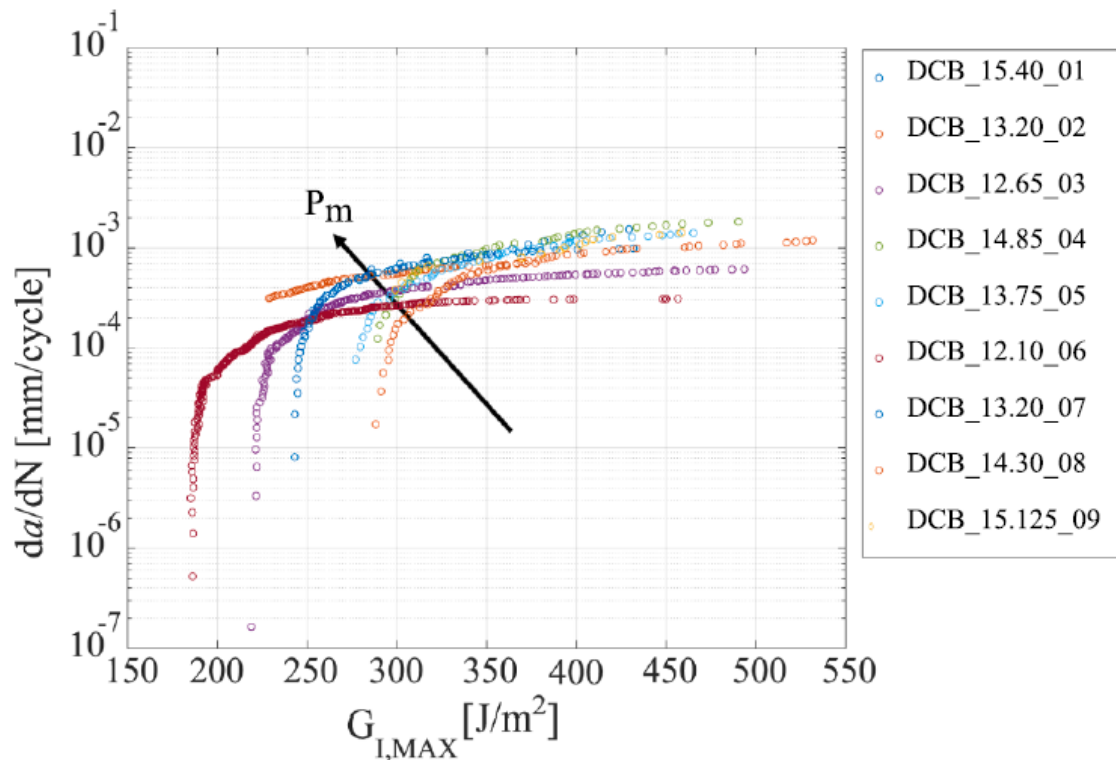


Figure 53 - Full-fatigue curve for various load ranges values.

Compliance methods for bonded joints: Part I - investigation of the standardized methods to obtain the Strain Energy Release Rate for Mode I (Ref. [30])

Summary:

The double cantilever beam (DCB) is the most acceptable geometry to obtain the critical strain energy release rate (G_{Ic}) of adhesive joints under Mode I. However, there are still some areas of uncertainty in the standardized compliance methods recommended by the ISO and ASTM standards in terms of accuracy in estimating the compliance of a bonded double cantilever beam and, consequently, G_{Ic} . In this work, an investigation of the standardized compliance methods for fracture characterization of bonded joints under Mode I is conducted, employing a finite element model to obtain the compliance of a double cantilever beam, considering different crack lengths. The compliance values determined from the finite element model are compared with those recommended by the standards. It is concluded that the standardized compliance methods are very sensitive to issues derived from crack length measurements. The crack length correction methodology proposed by the corrected beam theory is inadequate, which can lead to a wrong interpretation of the structure's behavior and the structural integrity assessment. The best approach to obtain the compliance of a double cantilever beam in respect of crack length is to use a compliance calibration method, fitting an expression for the experimental curve.

Compliance methods for bonded joints: Part II - Investigation of the equivalent crack methodology to obtain the strain energy release rate for Mode I (Ref. [31])

Summary:

The present work investigates the equivalent crack methodology by considering the Double Cantilever Beam (DCB) test to obtain the strain energy release rate of adhesive joints, using different compliance methods rather than the Compliance Based Beam Model (CBBM). This procedure allows the determination of the crack length based on the compliance of the specimen, which avoids crack growth monitoring during tests. The compliance values predicted by the analytical methods were studied and compared with a computational model, considering different crack lengths. Results showed that the preciseness of the crack length obtained by the equivalent crack method relies on the accuracy of the respective compliance method in predicting the load-displacement curve of a bonded double cantilever beam. The Euler-Bernoulli and Timoshenko beam models are not recommended to obtain an equivalent crack length based on the specimen's compliance since they overestimate the actual crack length. Best crack length predictions were obtained using compliance methods based on the beam-on-elastic foundation models, including an elastic interface to model the adhesive

layer joint. Similar strain energy release rate results were found for different compliance methods when using the equivalent crack methodology.

Structural Health Monitoring

Multi-objective Sensor Placement Optimization in Helicopter Main Rotor Blade Considering the Number of Sensors and Mode Shape Interpolation (Ref. [32])

Summary:

Sensor location optimization plays a key role in the application and development of structural integrity monitoring methodologies, especially in large mechanical structures. Given the existence of an effective damage detection and identification procedure, the problem arises of how many and how the acquisition points (sensors) should be placed so that the efficiency is maximum in the monitoring system. In this study, an innovative methodology is proposed in order to maximize the quality of modal information and minimize the number of sensors in SHM system. On maximizing the quality of modal information, it considered the reconstruction of mode shapes using kriging interpolation. The study was carried out on plate-type composite material structures for initial validation and later applied and validated on a main rotor blade of the AS-350 helicopter. The initial modal information (modal deformation) was obtained through the finite element method and the multi-objective Lichtenberg algorithm was used in the complex optimization process. The proposed method presented in this work allows distributing a minimum and sufficient amount of acquisition points in a structure in the best possible way in order to obtain more modal information for a better modal reconstruction from a kriging interpolation of these minimum points. Numerical examples and test results show that the proposed method is robust and effective to distribute a reduced number of sensors in a structure and at the same time guarantee the quality of the information obtained. The results also indicate that the modal configuration obtained by multi-objective optimization does not become trivial when a set of modes is used in the construction of the objective function. This strategy is an advantage in experimental modal analysis tests, as it is only necessary to acquire signals at a limited number of points, saving time and operating costs in vibration-based processes.

This work will be presented by the authors during the ICAF 2023 Conference and Symposium.

Highlights:

The main objective of the present study was to optimize the number of sensors and their respective locations in complex mechanical structures, and the major contributions of this study are (i) to perform a multi-objective optimization of sensors using the Lichtenberg algorithm (MOLA) and consider the sensor number variable; (ii) to apply the proposed methodology in a real AS-350 helicopter blade. The methodology proposed in this work is extremely important in modal testing, reducing signal acquisition time and costs, especially for large structures.

Starting from the experimental analysis of the main rotor blade, a numerical model was created by inverse modelling, in which the blade geometry is created from a single material. The mechanical properties of the model are obtained by a search algorithm in such a way that the numerical model behaves like the real one.

The blade is 4665 mm long, of which 3880 mm corresponds to the aerodynamic section whose profile is NACA0012. The numerical model of the blade was also developed in ANSYS® APDL from two symmetrical shells in the aerodynamic region (Figure 54). The material to be investigated by the search algorithm is a laminated composite of 12 layers having a thickness of 1.08 mm each.

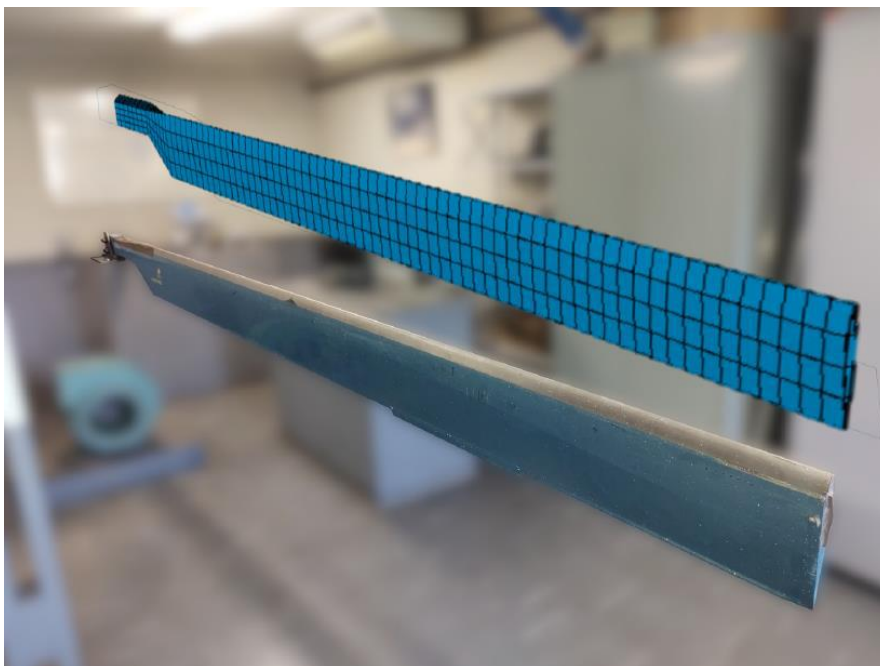


Figure 54 - Detail on the real model of the AS HB-350 blade and numerical model.

The approach with the kriging algorithm proved to be quite effective for the reconstruction of mode shapes for a plate. Modelling under the helicopter rotor blade seeks to apply this methodology to a practical problem in the SHM process. Due to the

complexity of the blade geometry, some simplifications in the boundary conditions and sensor layout were adopted to evaluate the problem.

Having determined the blade geometry and its mechanical properties, the modal analysis was performed numerically in order to obtain the first six mode shapes. The difference between the natural frequency calculated by the numerical model and the experimental model, in all modes evaluated, was less than 1%, except for the second mode, where the natural frequency varied 5%.

The positioning of the sensors resulting from this simulation is shown in Figure 55, for 8, 16, 22 and 48 sensors. The paper also shows the reconstruction of the mode shapes for these sensor positionings, from which it is clearly observed that with the increase in the number of sensors, the interpolation by kriging in order to obtain the continuous mode is significantly improved.

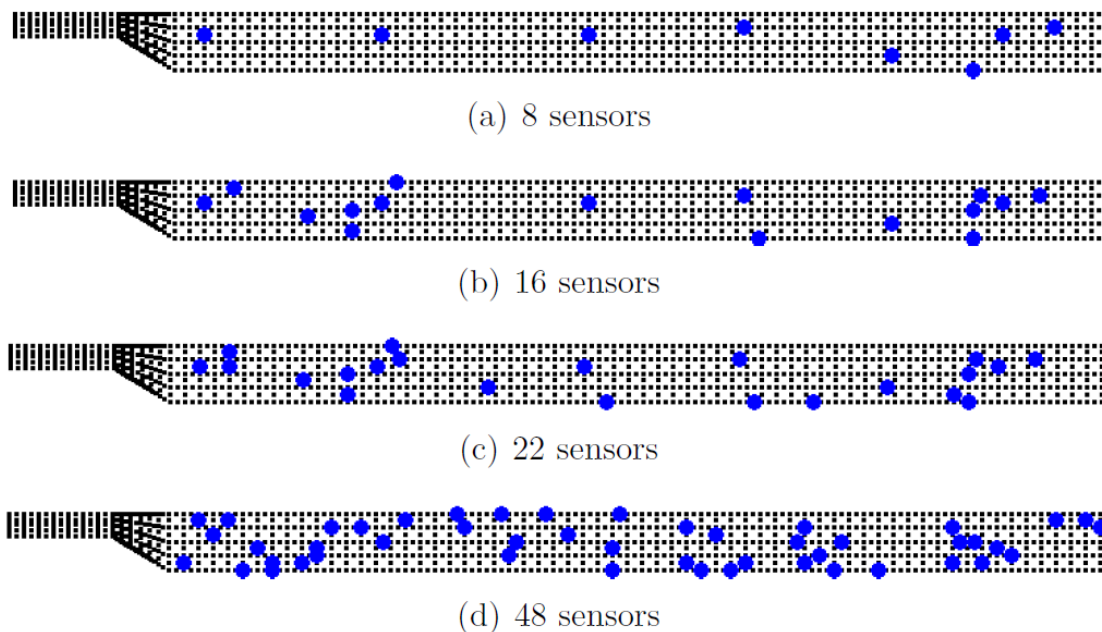


Figure 55 - Positioning sensors after optimization.

Delamination identification in sandwich composite structures using machine learning techniques (Ref. [33])

Summary:

Recent advances in machine learning have enabled powerful strategies for autonomous data-driven damage detection and identification in structural systems. This work proposes a novel method for 3D delamination identification in sandwich composite structures. Sandwich structures are prone to damage that is

difficult to detect, necessitating efficient and complex inspection techniques. In this context, automated structural health monitoring techniques are of great impact and importance in engineering. Such techniques use data obtained by sensors to identify damage to the structure.

In this paper, a complete methodology for damage (delamination) identification in sandwich composite structures using machine learning is proposed. The damage was parameterized in two different ways: as parametrized two- and three-dimensional ellipses, and it was considered in three different groups: the core, interface, and skin.

The modal data, obtained by the finite element method, was used to train several machine learning models in order to classify the location of the damage. In addition, modal dataset was also used to train artificial neural network regression models for damage localization and sizing. Both classification and regression strategies showed substantial results, and the models proved to be robust enough to identify a wide variety of damages. Results showed that classification models correctly identified the damage on the composite skin and incorrectly identified the interface core-skin damage. The regression model proved to be reliable in identifying an approximate location with an average accuracy of 85%. However, damage sizing is still a challenge to predict based only on modal datasets.

Highlights:

First a theoretical background about damage in composite structures is presented, followed by the description of certain important algorithms for optimization and machine learning methods. Then a numerical-experimental methodology is presented. Three numerical models were developed, one of the pristine plates and two with a core damage (3D) and an interface damage (2D). Figure 56 shows the overview of this model and the core damage location.

For the validation of the proposed method, specimens with and without damage were manufactured. The specimens were tested in a free vibration modal testing in order to obtain the modal data (natural frequencies and mode shapes) of the sandwich structure. Figure 57 shows the setup for testing of these plates.

Figure 58 shows the comparison between predicted and real damage locations and sizing, in this case for the core locations. Similar results are presented for the skin and interfaces. Besides this result, comparisons of modal responses and other parameters related to damage evaluation are presented and compared with the actual structure response.

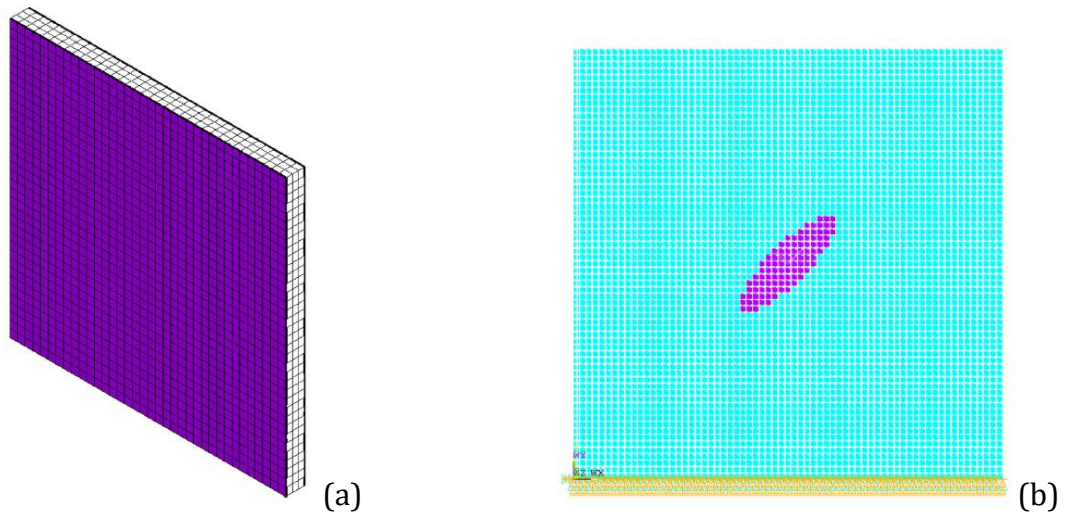
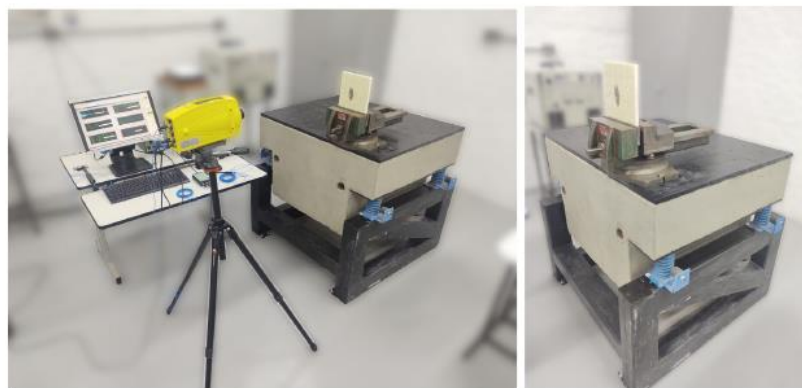
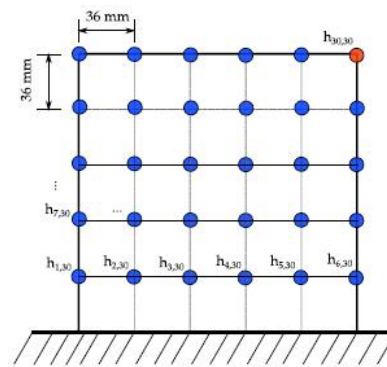


Figure 56 - Numerical model (a) isometric view, (b) parametrized damage.



(a) experimental setup

(b) inertial table detail



(c) discretized plate specimen

Figure 57 - Experimental setup for the modal testing.

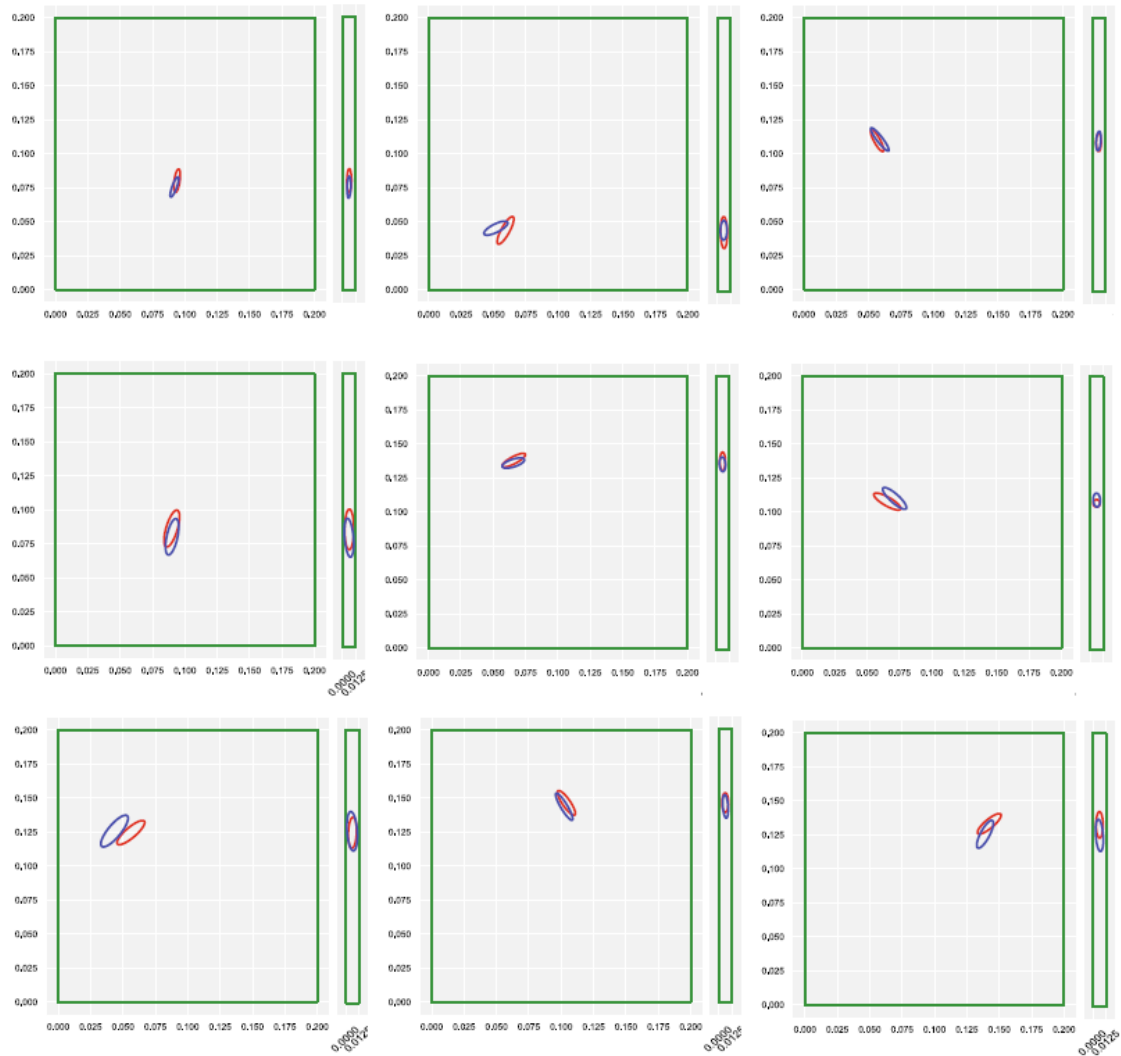


Figure 58 - Damage identification and sizing results for the damage type in core (actual and predicted).

5. PROBABILISTIC MODELLING AND RISK ANALYSIS

A Probabilistic methodology for analysis of secondary cracks in riveted structures (Ref. [34])

Summary:

Aeronautical structures are subjected to damages such as fatigue cracks due to their inherently cyclic loading. Therefore, it is important to understand the process of nucleation and propagation of cracks for application in modern aeronautical projects that use the damage tolerant approach. In this context, there are situations in which components or structural details may present the nucleation and propagation of an initial or primary crack, and after a determined number of load cycles, it may occur the nucleation and propagation of a secondary crack, in the proximities of the primary crack, due to the load redistribution caused by the primary crack. The nucleation and interaction of primary and secondary cracks in structural aeronautical components is relevant to the design of damage tolerant structures.

This work proposes an analysis methodology for the characterization of the nucleation, propagation, and interaction of primary cracks (or lead cracks) and secondary cracks in aeronautical components, considering probabilistic aspects and the current practices employed for the treatment of riveted structures. The methodology developed considers a random distribution of stress by fatigue life curves (S-N), that results in cases in which secondary cracks initiate, and cases in which they do not initiate (in consequence of the catastrophic failure of the component occurring beforehand due the propagation of the primary crack). From the cases in which the initiation of secondary cracks occurs, the simultaneous propagation of leader and secondary cracks is analyzed to quantify how the cracks influence each other or interact during their propagation. The results obtained indicate that the distributions of leader crack lengths at the moment that the secondary initiates tend to be normal, while the distributions of secondary crack lengths tend to be lognormal, in coherence with the Equivalent Initial Flaw Size methodology, currently employed in certain segments of the industry. From the propagation analysis, it was identified that secondary cracks tend to grow faster than the lead cracks, and the relative sizes between secondaries and lead cracks followed the general behavior found in data from detailed fleet inspections. With this, the present work offers a contribution to improve the design of aeronautical structures with a probabilistic approach for evaluation of primary and secondary cracks, both in terms of initiation and simultaneous propagation of fatigue cracks.

Highlights:

The work addresses secondary cracks, which are cracks that appear after a first initial crack named “lead” or “primary” crack, as the example in Figure 59. Starting from a diagram with tear-down inspection data that correlates the lengths of secondary and leader cracks (Figure 60), the authors developed a methodology to model the initiation and propagation of secondary cracks.

The methodology is applied to a riveted lap-joint based on NASM 1312-21 for a scenario with three cracks (one leader and two secondaries), and the results obtained (Figure 61) showed good correlation with the tear-down inspection data, Figure 62, plotted in units of millimeters and linear scale.

The process developed uses a random distribution of stress-life fatigue curves to model the variability in material properties. As result, the authors found that lead crack lengths when the secondary initiates tend to form a normal distribution, while the lengths of secondary cracks at initiation tend to form a lognormal distribution. This result agrees with what is currently employed in the Equivalent Initial Flaw Size methodology, which also uses lognormal distributions of cracks. The work also presents that secondary cracks tend to grow faster than lead cracks, and this has been associated with load redistribution.

The results presented in this work have been obtained analytically and lack of experimental verification, but nevertheless the work contributes to modelling and predicting the behavior of secondary cracks in aeronautical structural components in terms of initiation and simultaneous propagation, in a scenario that all cracks influence one another.

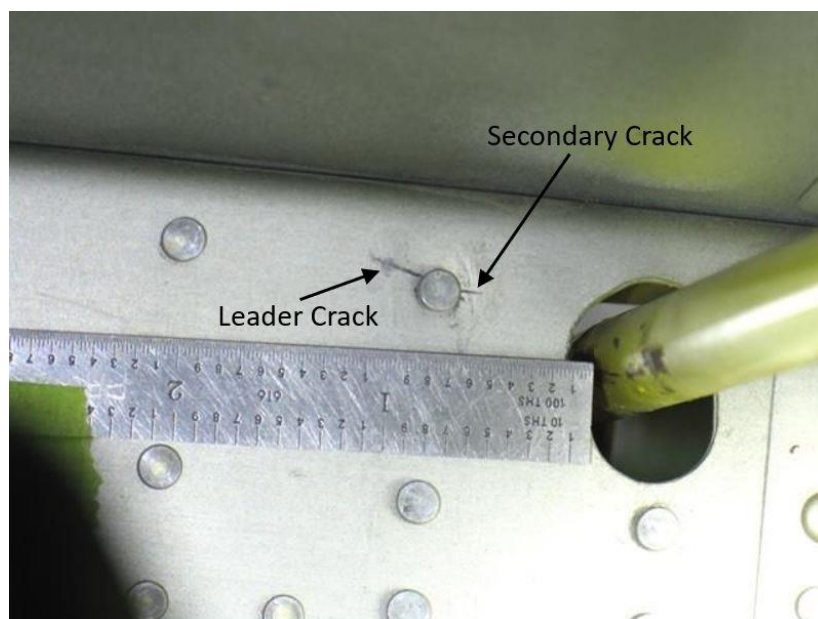


Figure 59 - Cracks on the web of the rear spar of a wing structure. Adapted from Ref. [35].

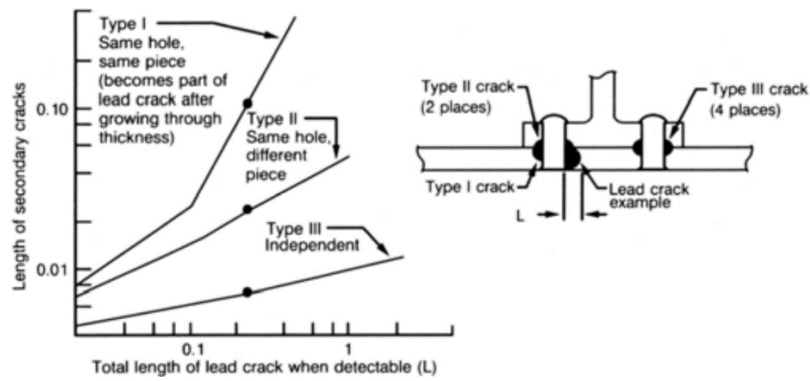


Figure 60 - On the left: length of secondary relative to length of lead crack when it is detectable. On the right: types of secondary cracks (Ref. [36]).

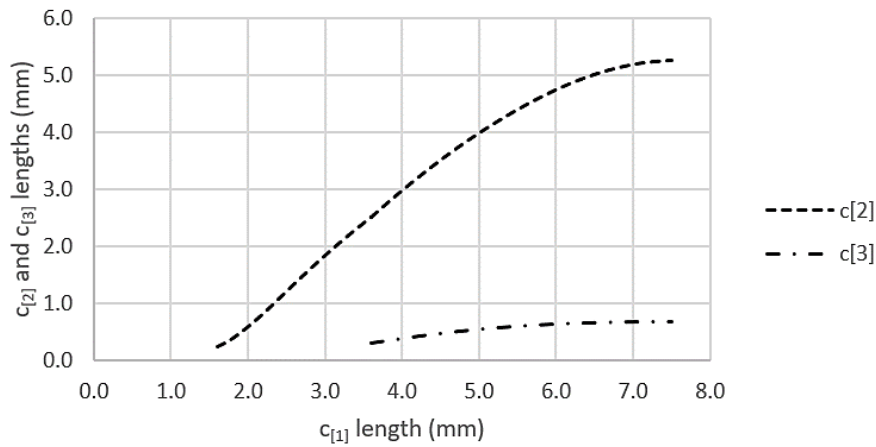


Figure 61 - Length of the secondary cracks ($c_{[2]}$ and $c_{[3]}$) relative to the length of the lead crack ($c_{[1]}$).

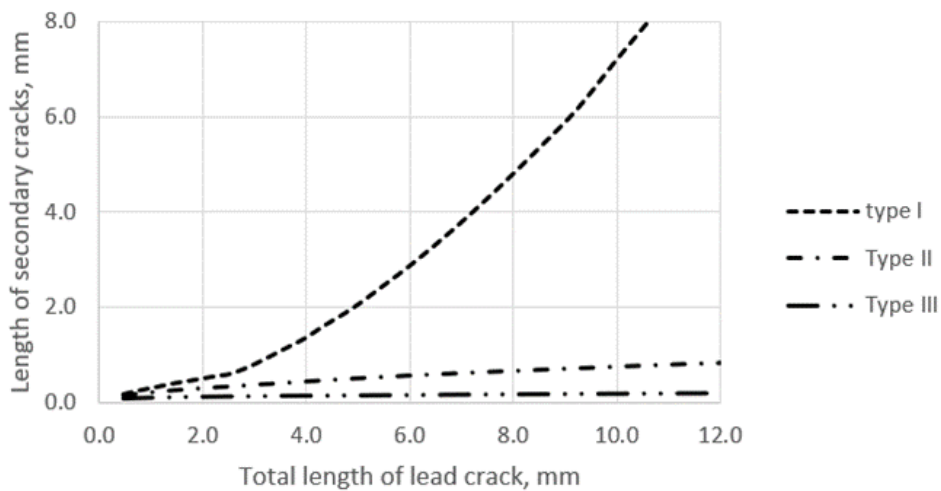


Figure 62 - Reconstruction of the chart presented in Figure 60 (Ref. [36]). Crack lengths converted to millimeters and curves plotted in linear scale.

6. FATIGUE LOADS

Towards deriving loads spectra representing operational life: equivalent flight profile versus single flight profiles (Ref. [37])

Summary:

Deriving the loads spectra is an essential task for structural sizing in order to achieve an acceptable economical life for a certain product. Furthermore, compliance with certification requirements shall be based on typical loading spectra expected in service. The task that arises consists in deriving loads spectra that represent an operational life comprising different flight profiles whose features may vary from one operator to another.

The current work aims to present two possible approaches to address this issue:

- (i) treating each flight profile distinctly, or
- (ii) deriving one equivalent flight profile that intends to accommodate all the former ones.

The work presents a stress analysis study performed for a hypothetical scenario, to compare the results for these two approaches. Moreover, it analyzes the benefits and risks that result from adopting one approach or another. Additional recommendations for the correct application of each approach throughout the airplane development and sizing are presented and discussed.

Highlights:

In general lines, the work presents some idealized flight profiles (named Flight 1, Flight 2, Flight 3, etc.) and their respective percentages of usage. Then, by using such profiles two approaches are outlined, as follows:

- The first approach is based on single flight profiles, where each flight profile originates its own flight load sequences, and a fatigue analysis must be performed in terms of each one. Then, the final fatigue life is obtained from weighted linear combination of each flight profile fatigue life, by the respective flight profile percentage of occurrence. This approach is summarized in Figure 63, with three flight profiles in this case.
- The second approach is based on an equivalent flight profile that intends to accommodate all the flight segments of all the typical flight profiles, pondering each segment duration by the corresponding flight profile percentage of occurrence in the proposed usage. In this solution, flight load sequences are derived from the equivalent flight profile and then the fatigue analyses are

performed in terms of this unique flight profile loads results. This approach is presented in Figure 64.

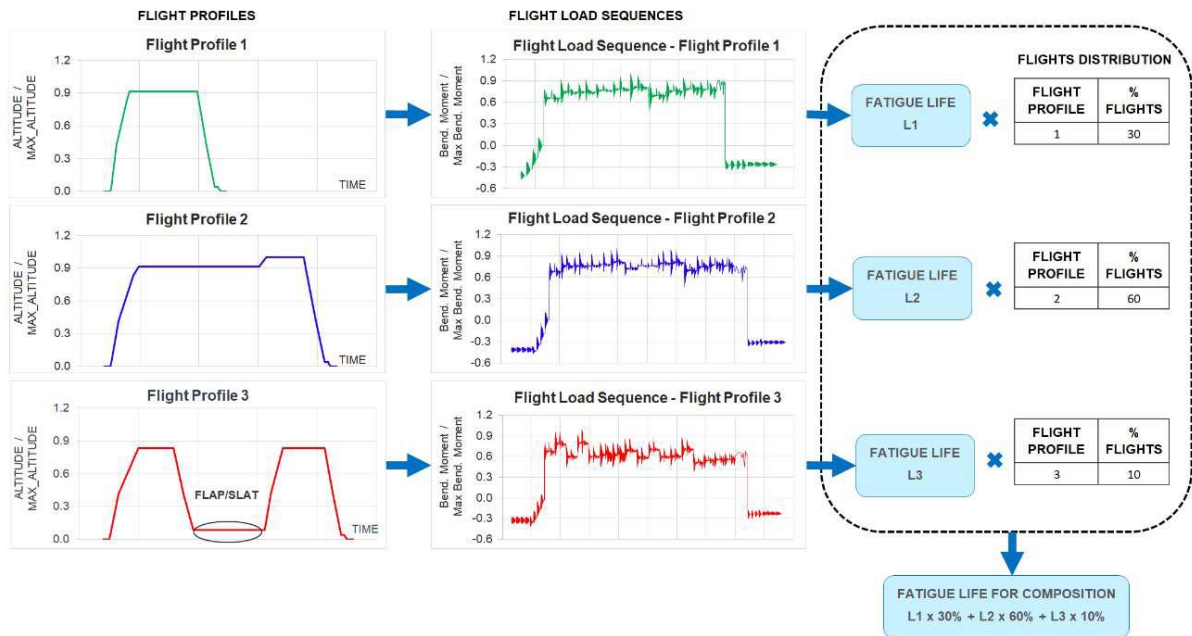


Figure 63 - Single flight profiles solution.

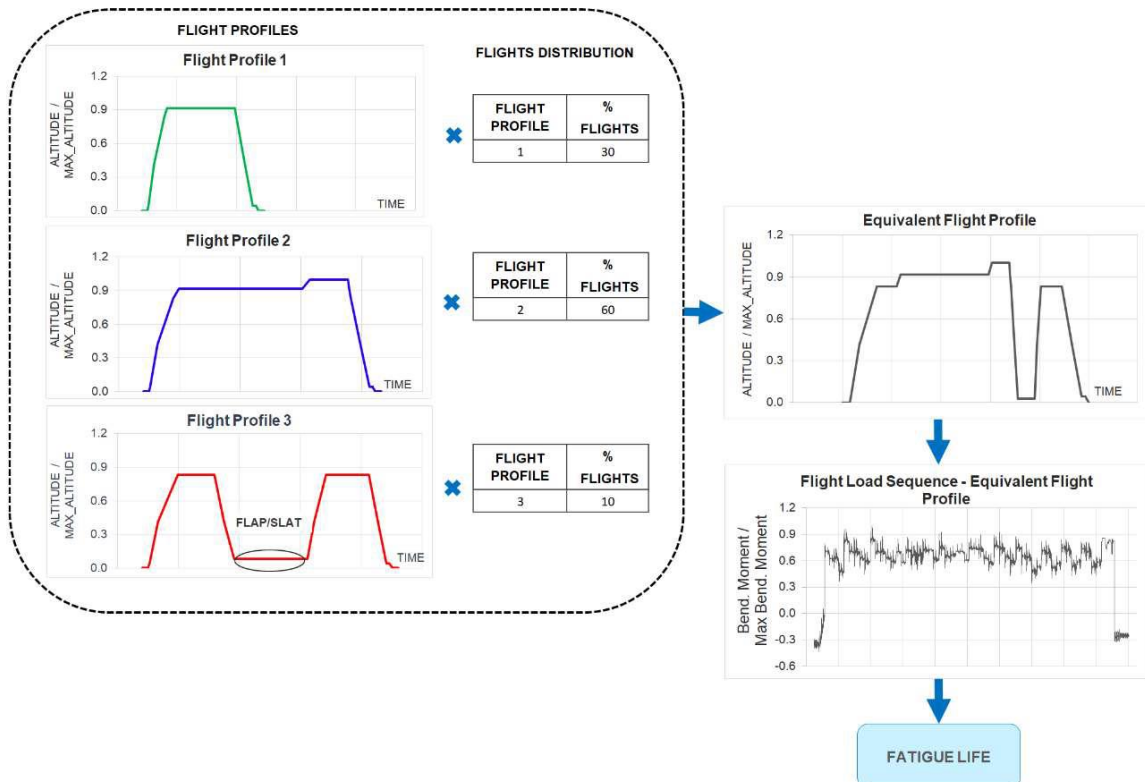


Figure 64 - Equivalent flight profile solution.

As a practical example, a component made from AA 7050 has a structural detail whose stress concentration factor is $K_t = 3.5$ and is analyzed with the application of spectra resulting from both approaches outlined above. There are four flight profiles for this example. The first three profiles (A, B and C) are frequently observed in transport missions, while flight profile D represents a specific scope of operation, that includes a low altitude and low speed cruise phase. Refer to Figure 65.

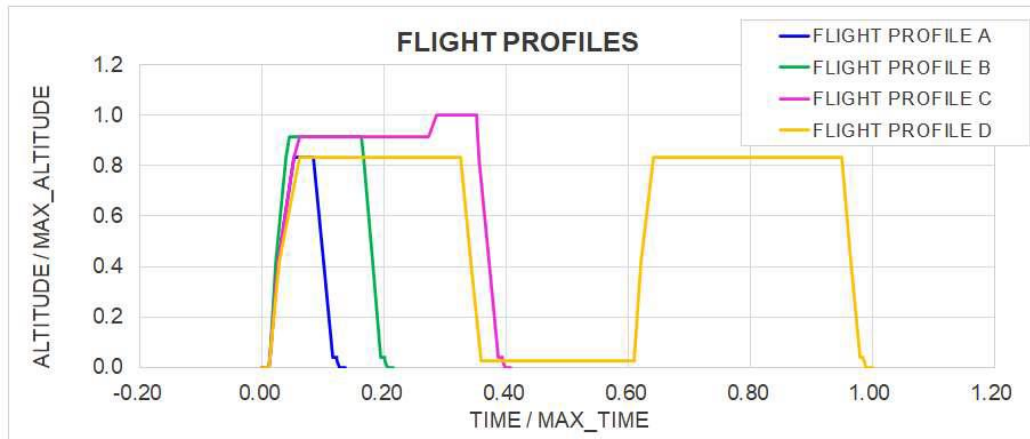


Figure 65 - Flight profiles A to D.

The different results in fatigue life for this example may be observed in Figure 66, which shows the number of lives obtained for the repetitions of each flight. The equivalent flight was taken as a reference, whose number of lives for failure of this structural detail was set to unity. For this example, it is clearly observed that the approach based on the composition of single flights leads to almost twice the life of the equivalent flight approach.

More details about this work will be presented by the authors during the ICAF 2023 Conference and Symposium.

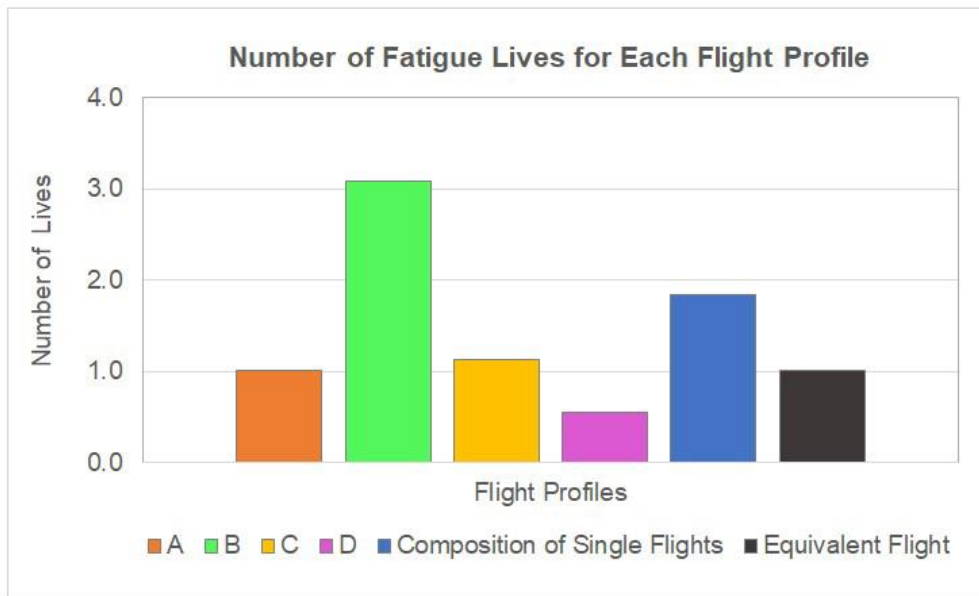


Figure 66 - Number of lives for the flight profiles and composition.

Plasticity effect on fatigue life of aeronautical structures considering a variable amplitude loading (Ref. [38])

Summary:

This work analyzes the effect of plasticity in the fatigue life of aeronautical structures that experience a variable loading scenario, by comparing a strain-based fatigue approach against a classical stress-based fatigue approach, which is lately modified to account for plastic deformation through a simple plasticity correction model. This work uses a representative loading scenario based on what airplanes experience throughout their operational life, by implementing the standardized TWIST loading sequence. Moreover, MINITWIST was used to verify the impact of a reduced spectrum that intends to be more suitable for testing. The material analyzed was aluminum 2024-T351 alloy and the geometry considered was an open-hole plate with 5 different stress concentration factors (1.0, 2.0, 2.5, 3.0, 3.33) in order to obtain a wider range of results. Rainflow cycle counting method is used to quantify the number of cycles per flight. A stress-life curve coupled to the Smith-Watson-Topper's mean stress correction and the Palmgren-Miner cumulative damage rule were used to determine the total fatigue damage. In addition, plastic deformation effects were accounted for by adjusting the maximum stresses of cycles that overcome the material yield strength, using Neuber's rule and Ramberg-Osgood equations iteratively. The numerical results showed that, for the spectra considered, the consideration of plasticity effects has increased the fatigue life by approximately 23% for the maximum stress concentration factor of 3.33 but has nearly no impact for the minimum stress concentration factor of 1.0

where plastic deformations didn't happen. Besides that, the use of MINITWIST loading spectra presented similar results to TWIST, indicating that for the scope of this study small amplitude load cycles do not affect much in fatigue life.

Highlights:

In this work three different methodologies were implemented, analyzed, and compared using a common use case. The first one was strain-based and the other two used the S-N curve coupled with SWT's equation for mean stress correction. The difference between the two stress-based approaches is that one considers the plastic effects by simple corrections and the other does not. All methods use the Palmgreen-Miner cumulative damage rule for fatigue life estimation, since this rule is largely tested providing more studies and results, and the standardized load sequence is based on TWIST methodology for all cases.

The number of occurrences was defined according to TWIST method. The procedure of generating the spectrum was divided for each flight stage, taxi, takeoff/landing roll and airborne. Airborne loads considered in this work are related to departure, climb, cruise, descent, and approach. Figure 67 shows one example of discretization obtained for airborne.

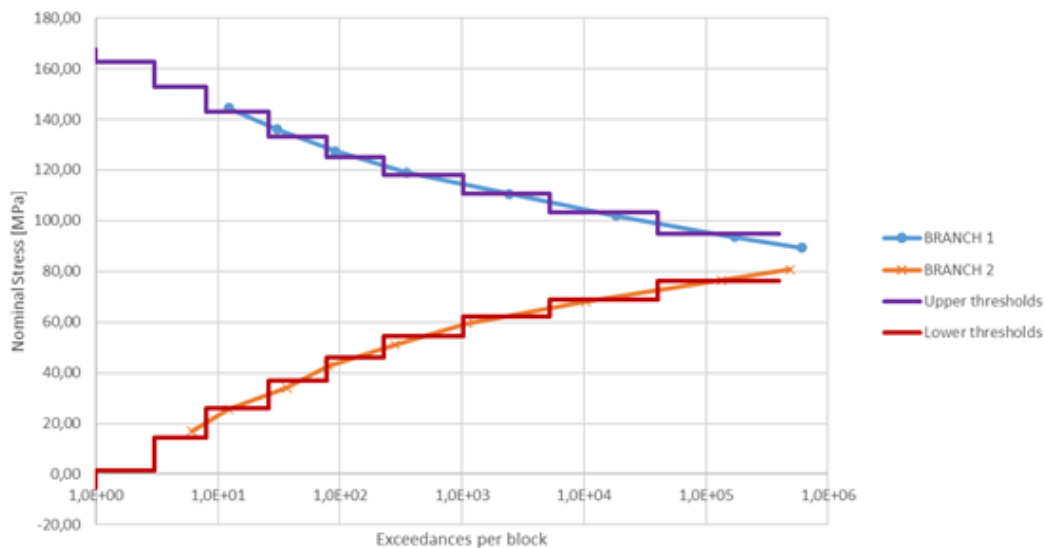


Figure 67 - Airborne spectrum discretization.

After discretizing the load cycles of each stage, these load groups were aligned following the flight stages presented in XX, to generate the flight load sequences and then go through a rainflow cycle counting method, having as output the count, the stress range, and the mean stress of each cycle of all ten flight types. To get the load sequences, the discretized load cycles of each flight stage were aligned simulating the ground-air-ground operation, respecting their number of occurrences, in the following order: taxi, roll, airborne, roll and taxi.

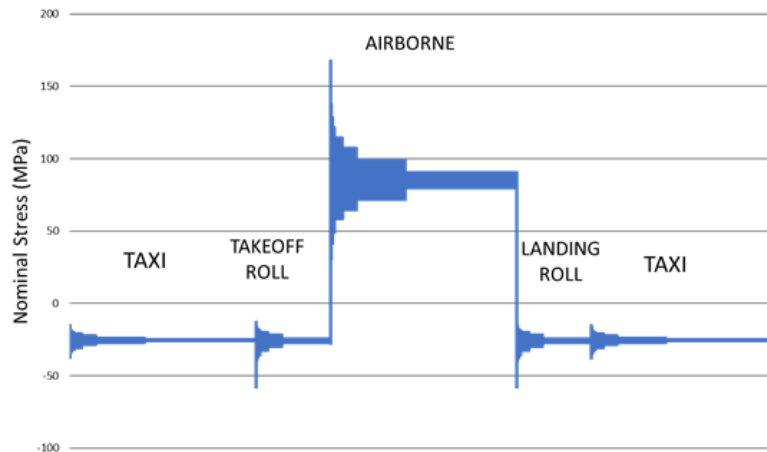


Figure 68 - Load sequence for TWIST Flight Type A.

While the first method applied for estimation of fatigue life is a conventional stress-life approach and the third method is a strain-life approach, for the second method the estimation of fatigue life was similar to the first one with addition of a plasticity correction in cycles that overcome the yield strength of the material. The idea behind this is to adjust only the cycles in which the maximum local stress is higher than yield strength by correcting the σ_{max} and σ_a as shown in Figure 69. This adjustment is not considered for subsequent cycles.

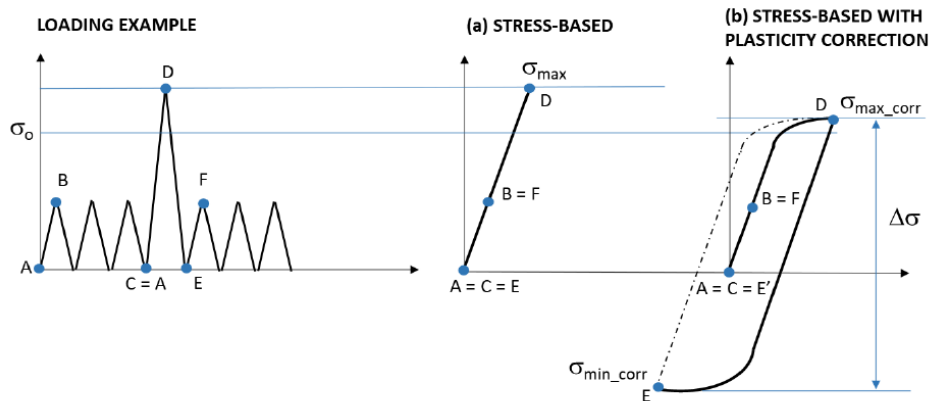


Figure 69 - Simple plasticity correction.

The damage per flight type for different stress concentration levels was then obtained. As a tittle of example, Figure 70 shows the damage per flight for $Kt = 3$.

For $Kt=3$, the closer values of block damage in relation to expected in real life, the strain-based method had 16,0% difference when compared to the stress-based method without plasticity correction. Thus, as a general conclusion from this work when fatigue is limiting the design of an aeronautical structure, the impact of

plasticity must be considered. The work lacks experimental validation, but similar observations based on test results may be found in Ref. [39].

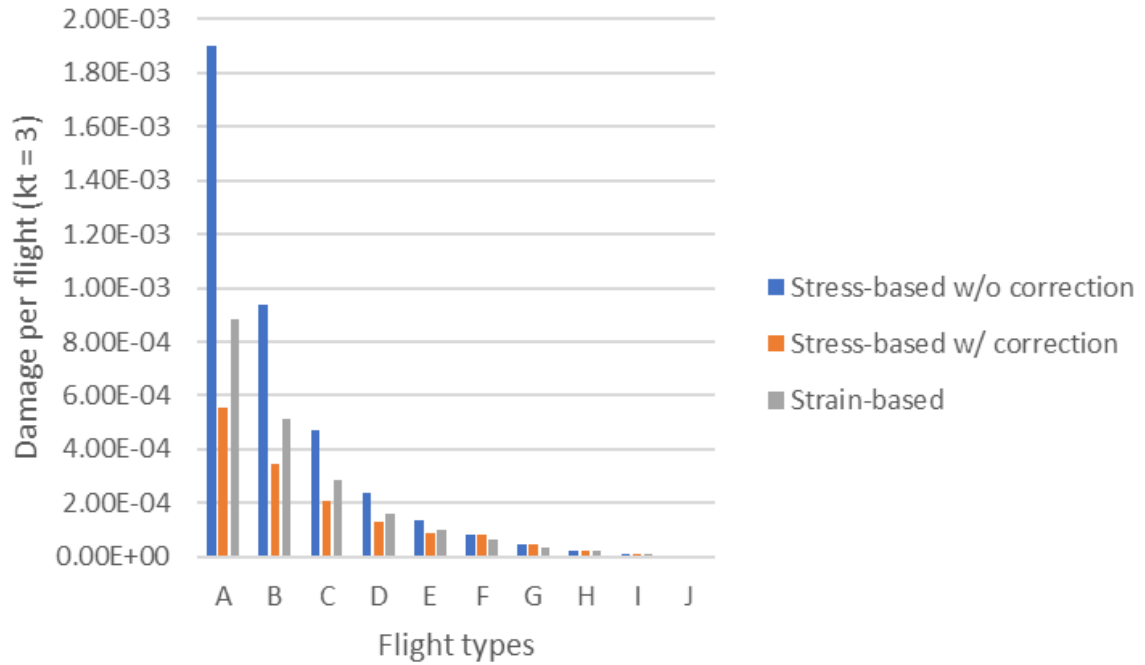


Figure 70 - TWIST damage per flight type for Kt=3.

7. AIRWORTHINESS

On the development of statistical knock-down factors for WFD assessment (Ref. [40])

The nucleation of multiple fatigue cracks over large areas, how they interact, and whether they can lead to a catastrophic event has been for a long time a concern, not only for the OEMs and the Regulatory Agencies, but also for the entire community involved in aircraft fleet management, as long as the fleets age. The phenomenon of Widespread Fatigue Damage (WFD) has been investigated for decades, and to demonstrate freedom of WFD up to the LOV for large transport aircraft structures became mandatory in the latest amendments of the regulations.

During the ICAF Symposium in 2013, Safarian (Ref. [41]) proposed an approach to assess WFD based on fatigue life estimation and the application of a set of knock-down factors. The present work provides an in-depth investigation for each of these factors, bringing a deduction or an explanation for them based on statistical approaches, together with some examples of application. By understanding each and every factor's origin and eventual built-in conservativeness, the engineer in charge can propose alternative approaches and come out with more realistic results, eventually saving weight and resources, without compromising safety.

The work, besides supplying the statistical basis of the knock-down factors of Ref. [41], intends to present some examples of that approach, extending its application while reducing some intrinsic conservatisms.

Highlights:

The work brings an in-depth investigation for the factors from Ref. [41], presenting a background and deduction or an explanation for them based on statistical approaches.

The Reliability and the Confidence Factors convert the mean or average values into values that meet the lower probability of failure or higher reliability targets, at the same time that accounts for the uncertainties due to the reduced test samples. The Testing Factor has no statistical origin, being more related to the shortcomings of the Pålmgren-Miner rule and has to be further investigated and understood.

The Confidence Factor has a similar effect of requiring higher reliability levels and may be either optimistic or overconservative based on the statistical distribution chosen. In addition, it is derived from the assumption that the failure of an entire assembly occurs when its first individual element presents a crack nucleation, what is also conservative because it does not account for crack growth, crack

interactions, load redistribution, among other effects on the actual structure. Such conservativeness can be further removed by testing structural arrangements as close as possible the actual structural arrangement.

Four practical examples were discussed and explained: (i) the origin of typical scatter factors for fatigue, (ii) calculating an intermediate scale factor, (iii) calculating the knock down factors for different “Alfa” (referring to Weibull statistics) and (iv) obtaining the knock-down factors for different distributions.

By understanding each and every factor’s origin and built-in conservativeness, the engineer in charge can propose alternative approaches and come out with more realistic results, eventually saving weight and resources, and developing optimized structures without compromising safety.

More details about this work will be presented by the authors during the ICAF 2023 Conference and Symposium.

Aircraft structural reliability/risk estimate with limited data using possibility theory (Ref. [42])

One of the most important fields of aircraft structural reliability is related to fatigue failures. Although several analyses and predictions are made during the design phase, only Full-Scale tests or fleet occurrences can identify some failures modes on specific details. Test data (and, in some cases, fleet data) can usually be a limited set, due to the inherent complexity, costs and time that a complete Full-Scale test demands, or due to a single isolated fleet leader occurrence.

This work proposes an approach to estimate structural reliability when limited data is available. While there is a known (possible) range, but not a properly known distribution for parameters as material properties, geometrical variation due to manufacturing tolerances, loading variation, etc, typical analysis proceeds by picking one value inside this range (it may be the mean, or the most conservative value). As predictions and conclusions made by a single observation point may carry a high amount of uncertainty, it will be useful to somehow quantify the effect related to the assumed parameters. Probabilistic calculation depends on well characterized distributions for inputs, which often is not available, so, alternatively, the Possibility Theory was used to explore the parameters that are usually estimated. A typical scenario was modelled and evaluated. Uncertainty propagation was performed with Independent Random Sampling (IRS) algorithm from R/RStudio software (HYRISK library). The analysis consists of a trunnion collar failure from a Main Landing Gear during a Full-Scale Fatigue Test, and risk prediction for fleet. The results are assessed and compared with typical calculation from reference literature. The proposed approach helps to better quantify and understand uncertainty in the prediction of aircraft structural

reliability/risk when only limited data is available. This gives a better and most realistic picture of reliability/risk ranges and each factor contributions, allowing for more appropriated and sound decisions.

Highlights:

First, the article supplies a brief review of some key statistical parameters, Uncertainty Theories, the Possibility Theory, and the Evidence Theory, among others. Then an example from Ref. [43]) is revisited, by applying the concepts introduced in this work. The example is about a trunnion collar made from 300M steel with $FTu=1930\text{ MPa}$. Due to manufacturing tolerances the stress concentration factor (K_t) in a certain detail of this component ranges from 10 to 13. The detail under analysis is shown in Figure 71. The purpose is to determine when this structure will reach a *SFPOF* (i.e., the probability of failure at one flight given that the aircraft has survived up to that point.) of 10^{-4} . A trunnion collar from a Main Landing Gear failed during the full-scale fatigue test after 2,310 simulated landings.

A set of *SFPOF* plots were presented in the work. In Figure 72, The effect on variability due to only material variation (α) is evaluated by “pinching” (fixing) K_t at its average level of 11.5. The minimum value on Possibility pinched curve is 340 FC, which matches the calculation from Tuegel et al. (Ref. [43]), that disregarded K_t variability and took the minimum (i.e., the most conservative) value of α ($\alpha = 2$). It can be noted that, for this case, the epistemic uncertainty is greatly reduced once the K_t variability is suppressed (as both Possibility and Necessity curves approaches each other). For this particular case and with the assumptions made, 340 FC would be the point for a safe intervention on the fleet.

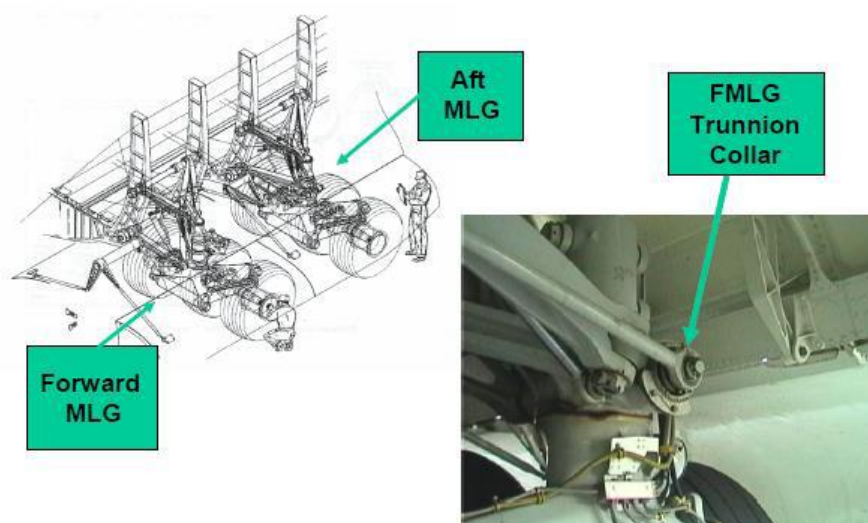


Figure 71 - MLG trunnion collar location, from Tuegel et al. (Ref. [43]).

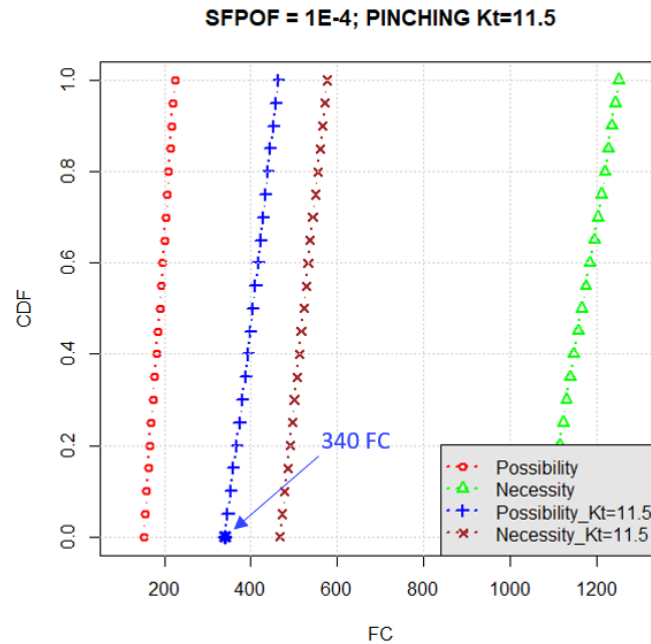


Figure 72 - CDF of SPOF= 10^{-4} point in FC; K_t Pinching Results.

EASA Part 26 Requirements (Ref. [44])

In 2021, EASA released Part 26 Ageing Aircraft Requirements. There are many categories of aircraft affected by this requirement, including families of commercial and executive jets made in Brazil.

Most of the requirements present commonality with previous FAA and ANAC Part 26 requirements. Others may require additional documentation for compliance.

This is a long-term work, and some activities may last until 2026 or later.

8. REFERENCES

Crack Growth Analysis and Simulation

1. Cruz, A. L., Donadon, M.V., *A mixed-mode energy-based elastoplastic fatigue induced damage model for the peridynamic theory*, Engineering Fracture Mechanics 275 (2022) 108834.
2. Cruz, A. L., Donadon, M.V., *An elastoplastic constitutive damage model based on peridynamics formulation*, International Journal of Non-Linear Mechanics 142 (2022) 103978.
3. Lopes, F.J.L. Lins, R.M., Arbelo, M.A., *Extraction of stress intensity factors via the displacement correlation method from stable generalized finite element solutions*, COBEM 2021 - 26th International Congress of Mechanical Engineering, Virtual Congress, Brazil - November 22-26, 2021.
4. Murakami, Y., *Stress Intensity Factor Handbook*, Pergamon Press, Oxford, 1987.

Metallic Materials – Fatigue and Fracture Properties

5. Cordeiro, R.M., *O Efeito de Retardo Devido a Sobrecargas na Propagação de Trinca por Fadiga*, MSc Dissertation (in portuguese), Aeronautics Institute of Technology, 2021.
6. Magalhães, A.L.R., *Crack Growth Retardation Models Under Load Interaction*, MSc Dissertation, Aeronautics Institute of Technology, 2022.

Metallic Materials - Fretting

7. Araújo, J.A., Nowell, D., Castro, F.C., *Fretting Fatigue*, Editor(s): M H Ferri Aliabadi, Winston O. Soboyejo, Comprehensive Structural Integrity (Second Edition), Elsevier, 2023, Pages 249-282, ISBN 9780323919456, <https://doi.org/10.1016/B978-0-12-822944-6.00004-9>.
8. Almeida, G.M.J., Cardoso R.A., Garcia, M.A., Chassaing, G., Pommier, S., Araújo, J.A., *Four actuators fretting fatigue rig and tests with cyclic normal load for Ti-6Al-4V*, Theoretical and Applied Fracture Mechanics 119 (2022) 103292.
9. Almeida, G.M.J., *Experiments, modelling, and analysis of fretting fatigue for Inconel 718 and Ti-6Al-4V under time-varying contact normal load at room and high temperature*, PhD Thesis, Universidade de Brasília and Université Paris-Saclay, September 2022.

10. Oliveira, G.A.B., Cardoso, R.A., Freire Jr., R.C.S., Araújo, J.A., *A generalized ANN-multiaxial fatigue nonlocal approach to compute fretting fatigue life for aeronautical Al alloys*, Tribology International, 180 (2023) 108250.
11. Pinto, A.L., *Fretting fatigue under variable amplitude loading*, PhD Thesis, UK Leuven, University of Brasília, September 2022.

Metallic Materials – Mechanical Processes and Surface Treatments

12. Carvalho, C.P.; de Lima, Pascon, J.P., Lima, M.S., Baptista, C.A.R.P., *Investigation of laser treatment as a method for fatigue crack growth retardation in Aluminum Alloy 2198-T851* - Proceedings of the 31st ICAF Symposium - Delft, The Netherlands, June 26-29, 2023.
13. Baptista, C.A.R.P., Antunes, A.M., de Paula, S.M., Peinado, G.C.C., *Effects of the secondary aging heat treatment T614 on fracture toughness and fatigue crack growth resistance of AA7050 alloy* - Proceedings of the 31st ICAF Symposium - Delft, The Netherlands, June 26-29, 2023.

Metallic Materials – Structures

14. Belem, F.R., *Post-buckling fatigue crack propagation on curved stiffened panels*, MsC Dissertation, Aeronautics Institute of Technology, 2022.
15. Stonaker, K., Bakuckas Jr., J.G., Zhang, T., Kulak, M., Maciejewski, K., Sippel, W., Fanton, F., Chaves, C.E., Jonas, P., *Characterization of MSD in emerging metallic structures in fuselage lap joints*- Proceedings of the 31st ICAF Symposium - Delft, The Netherlands, June 26-29, 2023.
16. Félix, P.H.W., Arbelo, M.A., *Crack Growth Analysis of Fiber Metal Laminates Stiffened Panels*, ICAF 2023 - Delft, The Netherlands, June 26-29, 2023.
17. Marques, D.E.T., Ribeiro, M.L., Tita, V., *Comparative study of adhesive fatigue in aeronautical bonded joints: A numerical approach in the frequency domain*, Proc IMechE Part L: J Materials: Design and Applications 2022, Vol. 236(7) 1400–1407.

Metallic Materials - Structural Health Monitoring

18. Marques, D.E.T., Vandepitte, D., Tita, V., *Damage detection and fatigue life estimation under random loads: A new structural health monitoring methodology in the frequency domain*, Fatigue Fract Eng Mater Struct. 2021;44:1622–1636.
19. Marques, D.E.T., Vandepitte, D., Tita, V., *Sensitivity and uncertainty analysis for structural health monitoring with crack propagation under random loads: A numerical framework in the frequency domain*, Fatigue Fract Eng Mater Struct. 2023;46:137–152.
20. Dirlik T, Benasciutti D., *Dirlik and Tovo-Benasciutti spectral methods in vibration fatigue: a review with a historical perspective*. Metals. 2021;11(9):1333.

Composite Materials and Structures

21. Gonçalves, V.O., *Avaliação da resistência estática e em fadiga em compósitos de fibra de carbono/epóxi com diferentes níveis de porosidade sob esforço de compressão*, PhD Thesis (in portuguese), Aeronautics Institute of Technology, 2022.
22. Gonçalves, V.O., Osses, M., Pardini, L.C., *New jig adapted for compression fatigue tests on composite materials*, Journal of Composite Materials 2023, Vol. 57(2) 337–344.
23. Silva, T.C., Moraes, D.V.O., Morgado, G.F.M., Gonçalves, V.O., Costa, D.H.S., Marques, T.P.Z., Passador, F.R., Rezende, M.C., *Mechanical characterization and fractographic study of the carbon/PEI composite under static and fatigue loading*, Mechanics of Advanced Materials and Structures, 2022 <https://doi.org/10.1080/15376494.2022.2134952>.
24. Ferreira, G.F.O., Almeida Jr., J.H.S., Ribeiro, M.L., Ferreira, A.J.M., Tita, V., *A finite element unified formulation for composite laminates in bending considering progressive damage*, Thin-Walled Structures 172 (2022) 108864.
25. Monticeli, F.M., *Fadiga em compósitos híbridos processados via RTM: influência da interface híbrida na delaminação nos Modos I e II*, PhD Thesis (in portuguese), State University of São Paulo, 2021. Manuscript available in: <https://repositorio.unesp.br/handle/11449/214667>.
26. Cândido, G.V., Sales, R.C.M., Arbelo, M.A., Donadon, M.V., *Failure analysis in secondary bonded T-stiffened composite panels subject to cyclic and quasi-static compression loading*, International Journal of Adhesion & Adhesives 118 (2022) 103199.
27. Fuga, F.R., Donadon, M.V., *A progressive damage model for composite laminates based on non-linear continuum mechanics—Static and fatigue loadings*, Theoretical and Applied Fracture Mechanics 122 (2022) 103639.
28. Souza, R.R., Nascimento Jr., S.L., Silveira, N.N., Arbelo, M.A., Donadon, M.V., *Translaminar fracture toughness and fatigue crack growth characterization of carbon-epoxy plain weave laminates*, Polym. Compos. 40 (10) (2019) 3791–3804, <http://dx.doi.org/10.1002/pc.25247>.
29. Marinho, N.R., Arbelo, M.A., Cândido, G.M., Sales, R.C.M., Donadon, M.V., *Effects of mean load on interlaminar fracture behavior of carbon-epoxy prepreg fabric laminates under Mode I fatigue loading*, Composite Structures 276 (2021) 114451.
30. Madureira, F., Silva, L.F.M., Tita, V. (2022) , *Compliance methods for bonded joints: Part I - Investigation of the standardized methods to obtain the strain energy release rate for Mode I*, The Journal of Adhesion, DOI: 10.1080/00218464.2022.2144731.

31. Madureira, F., Silva, L.F.M., Tita, V. (2022), *Compliance methods for bonded joints: Part II - Investigation of the equivalent crack methodology to obtain the strain energy release rate for Mode I*, The Journal of Adhesion, DOI: 10.1080/00218464.2022.2144732.

Composite Materials - Structural Health Monitoring

32. Mello, F.M.S., Pereira, J.L.J., Gomes, G.F., *Multi-objective sensor placement optimization in helicopter main rotor blade considering the number of sensors and mode shape interpolation*- Proceedings of the 31st ICAF Symposium - Delft, The Netherlands, June 26-29, 2023.
33. Viotti, I.D., Gomes, G.F., Gomes, G. F., *Delamination identification in sandwich composite structures using machine learning techniques*, Computers and Structures 280 (2023) 106990.

Probabilistic Modelling and Risk Analysis

34. Lemes, C.A.P., Arbelo, M.A., Barbosa, A.F., Chaves, C.E., *A probabilistic methodology for analysis of secondary cracks in riveted structures*, 2023 AIAA Aviation Forum. San Diego, CA & Online, June 2023.
35. Van's Service Bulletin affects all E-AB Models. Norwalk: Kitplanes Magazine. 2016. Available at: <https://www.kitplanes.com/vans-service-bulletin-affects-all-e-ab-models>. Accessed on: 26 Jul. 2022.
36. Goranson, U., *Damage tolerance – facts and fiction*, keynote presentation, DTAS Conference, Delft, The Netherlands, 2007.

Fatigue Loads

37. Mattos, J.D., Arbelo, M.A., Machado, F., *Towards deriving loads spectra representing operational life: equivalent flight profile versus single flight profiles*, - Proceedings of the 31st ICAF Symposium - Delft, The Netherlands, June 26-29, 2023.
38. Reis, N.S., Arbelo, M.A., Chaves, C.E., *Plasticity effect on fatigue life of aeronautical structures considering a variable amplitude loading*, MECSOL 2022, Campinas, Brazil, October 2022.
39. Schijve, J., *Fatigue of Structures and Materials*, 2nd Edition, Springer, 2009.

Airworthiness

40. Rissardo, W., Chaves, C.E., *On the development of statistical knock-down factors for WFD Assessment*, ICAF 2023 - Proceedings of the 31st ICAF Symposium - Delft, The Netherlands, June 26-29, 2023.

41. Safarian, P. (2013), *Widespread Fatigue Damage Evaluation Method*, Proceedings of the 27th ICAF Symposium - Jerusalem, Israel, June 03-07, 2013.
42. Oliveira, M.C.C.Z., Cardoso, M.M., Arbelo, M.A., *Aircraft structural reliability/risk estimate with limited data using possibility theory*, MECSOL 2022, Proceedings of the 8th International Symposium on Solid Mechanics, Campinas-SP, Brazil, October 17-19, 2022.
43. Tuegel, E. J., Bell, R. P., Berens, A. A. P., Brussat, T., Cardinal, J. W., Gallagher, J. P. and Rudd, J., 2018, *"Aircraft Structural Reliability and Risk Analysis Handbook. Volume 1: Basic Analysis Methods."* Wright-Patterson Air Force Base, OH: Air Force Research Laboratory, v.1. (AFRL-RQ-WP-TR-2018-0180).
44. EASA (European Aviation Safety Agency) – CS-26 requirement and AMC 20-20, <https://www.easa.europa.eu/en/downloads/121014/en>
<https://www.easa.europa.eu/en/downloads/121020/en>